X-ray Study of Low-mass Young Stellar Objects in the ρ Ophiuchi Star-forming Region with *Chandra*

Kensuke Imanishi

Department of Physics, Graduate School of Science,
Kyoto University, Sakyo-ku, Kyoto 606-8502, Japan

Submitted to the Department of Physics, Kyoto University
in partial fulfillment of the requirements
for the degree of Doctor of Science

January 6, 2003

Abstract

We present the results of a systematic X-ray study of low-mass young stellar objects, using two deep exposure *Chandra* observations of the main region of the ρ Ophiuchi star-forming cloud. From the central 1 pc $\times$ 2 pc region, we detect 195 X-ray sources with the detection limit of the X-ray luminosity of $\sim 10^{28}$ ergs s^{-1}. About 60 % of them (110/195) are identified with optical and/or infrared counterparts, including significant numbers of class I, II, III sources, and some young brown dwarfs. Most of the X-ray spectra are well fitted by a single temperature thin thermal plasma model with the elemental abundance of 0.3 solar, although some sources show unusual features; overabundances (GY21, S2, and WL22), abundance variation among elements (DoAr21, ROXs21, and ROXs31), multi-temperature spectra (ROXs21 and ROXs31), 6.4 keV line emission (YLW16A), and a possible non-thermal spectrum with the absorption edge of Ca or Ar (S1). The absorption column density ($N_{\rm H}$) is spread around the average value through the cloud ($\sim 10^{22.5}$ cm^{-2}) and is proportional to the visual extinction (A_V). The time-averaged plasma temperature ($< kT >$) is in the range of 0.2–10 keV. The time-averaged X-ray luminosity ($< L_X >$) is well correlated with the bolometric luminosity ($L_{\rm bol}$), stellar mass, and radio (cm) luminosity. We detect 71 X-ray flares. Most of them have the typical profile of those of solar and stellar flares (fast rise and slow decay), while some bright flares show unusually long rise timescales. We find that (1) class I–II sources tend to have higher $< kT >$, which sometimes exceeds 5 keV, (2) the distribution of $< L_X >$ during flares is nearly the same for all the classes from $\sim 10^{29.5}$ to $\sim 10^{31.5}$ ergs s^{-1}, although there is a marginal hint of higher $< L_X >$ distribution for class I than class II–III, and (3) positive and negative log-linear correlations are found between the rise (τ_r) and decay (τ_d) timescales, and $< kT >$ and τ_r. In order to explain these relations, we use the framework of magnetic reconnection model with heat conduction and chromospheric evaporation (Shibata & Yokoyama 1999, 2002) to formulate the observational parameters (τ_r, τ_d, and $< kT >$) as a function of the pre-flare (coronal) electronic density (n_c), the half-length of the reconnected magnetic loop (L), and magnetic field strength (B). The observed correlations are well reproduced if loop lengths are nearly the same for all classes, regardless of the existence of an accretion disk. The estimated loop length is almost comparable to the typical stellar radius of these objects (10^{10}–10^{11} cm), which indicates that the observed flares are triggered by solar-type loops rather than larger ones ($\sim 10^{12}$ cm) connecting the star with its inner accretion disk. The higher $< kT >$ observed for class I sources may be explained by a slightly higher magnetic field strength ($\approx$500 G) than for class II–III sources (200–300 G).

Contents

List of Figures

List of Tables

Chapter 1

Introduction

Star formation process is one of the most important issues in astronomy. Young stellar objects (YSOs) are born in dense molecular cloud cores and evolve through the Hayashi and Henyey tracks in the Hertzsprung-Russell (H-R) diagram to the main-sequence stage. However, observational information about YSOs is still limited because the dense circumstellar envelope absorbs and scatters infrared–optical photons emitted from YSOs.

Recent observations have discovered X-rays from many low-mass YSOs (Feigelson & Montmerle, 1999, for a review). Their characteristics of high temperature spectra ($\sim$1 keV) and strong time variability with occasional rapid flares are basically the same as the solar X-rays, hence their origin would be solar-type activity attributable to magnetic dynamo processes. These pioneering discoveries demonstrate the unique capability of X-ray observations to probe YSOs themselves through the circumstellar envelope, using their high penetrating power.

Thus, the next step should be a systematic X-ray study of YSOs and to approach physical conditions of these initial stages of stars, which gives extremely important information to the star formation theory. The ρ Ophiuchi cloud (ρ Oph) is the best site for this purpose, because it is among the closest star-forming regions (distance = 145 pc[1]), well studied in the radio–infrared bands, and contains a wide variety of samples in different physical conditions (age and mass). The previous X-ray satellites such as *Einstein*, *ROSAT*, and *ASCA* detected X-rays from some low-mass YSOs in ρ Oph (Montmerle et al., 1983; Koyama et al., 1994; Casanova et al., 1995; Kamata et al., 1997; Grosso et al., 2000). However, those samples are too limited because of low sensitivity at the hard X-ray band (>2 keV) and/or poor spatial resolution. The *Chandra* X-ray Observatory has the wide energy band sensitivity (0.5–9.0 keV) coupled with the unprecedented spatial resolution ($\sim 0''.5$), hence is the best observatory for X-ray studies of YSOs.

[1]The distance corresponding to a parallax angle of $1''$. 1 pc = 3.1×10^{18} cm.

In this thesis, we report results of two deep exposure *Chandra* observations of ρ Oph. We first give brief reviews of low-mass YSOs and ρ Oph in chapters 2 and 3. Details of the *Chandra* satellite and its instruments are shown in chapter 4. Chapter 5 describes the method of data analysis and gives source catalogues. Comments on some interesting sources are shown in chapter 6. Then we discuss overall X-ray properties of YSOs in chapter 7. We further put particular emphasis on their flare activity and predict the evolution of X-ray activity on YSOs as shown in chapter 8. Finally, chapter 9 gives a brief summary.

Chapter 2

Review of Low-mass Young Stellar Objects

2.1 Evolution of Low-mass Stars

The evolution of low-mass stars (mass = 0.1–1.5 $M_\odot$[1]) is well traced by the locus on the Hertzsprung-Russell (H-R) diagram (Figure 2.1: Hayashi, 1966). Through a dynamical collapse, interstellar medium starts condensing. The density soon becomes so large that the shock wave emerging at its center propagates towards the outer region, which is followed by a dynamical equilibrium state with the timescale of $\sim 10^4$ yr. This phase is called "protostars", the first stage of stars. Protostars are born at the top-right side in the H-R diagram (higher bolometric luminosity and lower surface temperature), although we can not see the central sources because of large extinction at dense circumstellar envelope. The main mechanism of energy transportation in the stellar interior is convection (fully convective structure). They evolve along the track of reducing the luminosity with nearly constant temperature (Hayashi track). While moving down on this track, the envelope gradually disappears and the central sources become optically visible ($\sim 10^6$ yr), which is called "T Tauri stars (TTSs)". After 10^7 yr later, the radiative energy transportation becomes dominant and the temperature gradually increases with a constant luminosity (Henyey track: Henyey, Lelevier, & Levée, 1955). During the hydrogen burning ($\sim 10^8$ yr), the stars stay at a certain point in the H-R diagram, which is called "main-sequence stars (MSs)". Protostars and TTSs are called "pre-main-sequence stars (PMSs)", or "young stellar objects (YSOs)".

[1]The stellar mass normalized by the solar value. 1 $M_\odot$ = 2.0×10^{33} g.

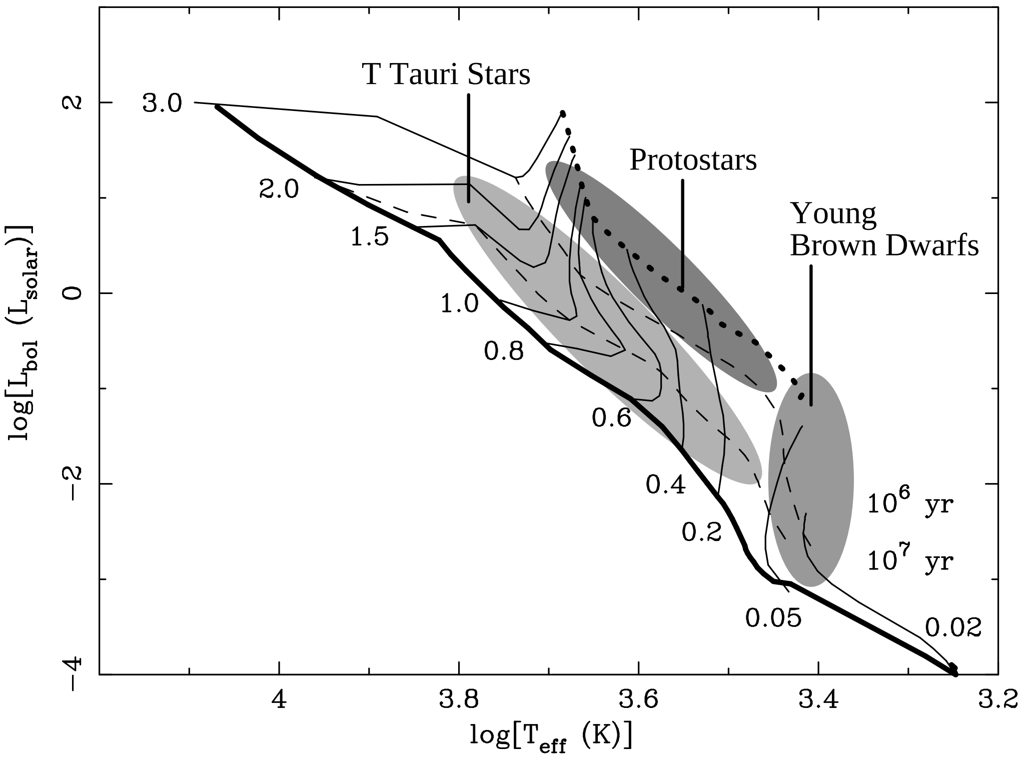

Fig. 2.1.— The H-R diagram (D'Antona & Mazzitelli, 1997). The horizontal and vertical axes are the surface (effective) temperature and bolometric luminosity normalized by the solar value (1 $L_\odot$ = 3.8×10^{33} ergs s^{-1}). Thin solid and dashed lines represent the evolutional tracks (Hayashi and Henyey tracks) with the mass of 0.02–3.0 $M_\odot$ and isochrones with the ages of 10^6 and 10^7 yrs, while thick solid and dashed lines are the main-sequence track and the birth line, respectively. Ellipses show the approximate positions of protostars, T Tauri stars, and young brown dwarfs.

Low-mass YSOs are classified into four types based on their spectral energy distributions (SEDs) from the near-infrared (NIR) to sub-millimeter (sub-mm) wavelengths (Figure 2.2; Lada 1991). Class 0 sources (André, Ward-Thompson, & Barsony, 1993; Barsony, 1994) are at the early phase of protostars ($t \sim 10^4$ yr). Although the central source is hidden by the dense material, we can observe emission from cold ($\sim$30 K) circumstellar envelope at the far-infrared (FIR) to millimeter (mm) bands. In the class 0 phase, much angular momentum is transferred into the central source through dynamical mass accretion. Part of them escape outward via bipolar outflows, which is confirmed by some observational evidence such as molecular (CO, H_2, etc.) and atomic (Herbig-Haro object) line emissions with a scale of $\lesssim 10^4$ AU[2] and centimeter (cm) continuum emissions

[2] The average distance from the earth to the sun (astronomical unit). 1 AU = 1.5×10^{13} cm.

which may be produced by a shock of the jet from a putative protostar on the interstellar medium (e.g., Rodriguez et al., 1989, and references theirin). About 10^5 yr later, most of the materials have accreted onto the central source and the emission from the accretion disk reprocessing incident starlight starts to be observed from the NIR to mid-infrared (MIR) bands, which is called class I sources (late phase of protostars). They still show outflow activity. Class II sources are at the early phase of TTSs (classical T Tauri stars = CTTSs). Although the emission from the central source becomes dominant, they show excess emissions from K (2.2 μm) to MIR bands and strong optical Hα lines, indicating the presence of an accretion disk. Soon the disk disappears and the SEDs become a single temperature blackbody. We call them class III sources, or weak-lined T Tauri stars (WTTSs).

If sources have a mass below $\approx$0.08 $M_{\odot}$, dynamical contraction stops before the hydrogen burning starts, hence they never arrive at the MS stage, which is called "brown dwarfs (BDs)" (Basri, 2000). They emit faint optical–IR photons using gravitational energy and consequently are relatively bright at a younger phase (Figure 2.1). Hereafter, we call those BDs still in the mass contraction phase "young BDs" (i.e., on the Hayashi and Henyey tracks, Figure 2.1).

The evolution of high- and intermediate-mass stars ($>$1.5 $M_{\odot}$) would be the same as low-mass ones; they also evolve along the Hayashi and Henyey tracks. However, there are very few samples of high/intermediate-mass YSOs (e.g., Waters & Waelkens, 1998; Howard, Pipher, & Forrest, 1994), because they quickly start hydrogen burning then reach the MSs during the mass contraction phase. Detailed understanding of these classes therefore has not been obtained. In this thesis, we basically do not discuss them. For the results of X-ray observations of high/intermediate-mass YSOs, see Hamaguchi et al. (2000); Hamaguchi (2001); Kohno et al. (2002); Takagi et al. (2002); Nakajima et al. (2003).

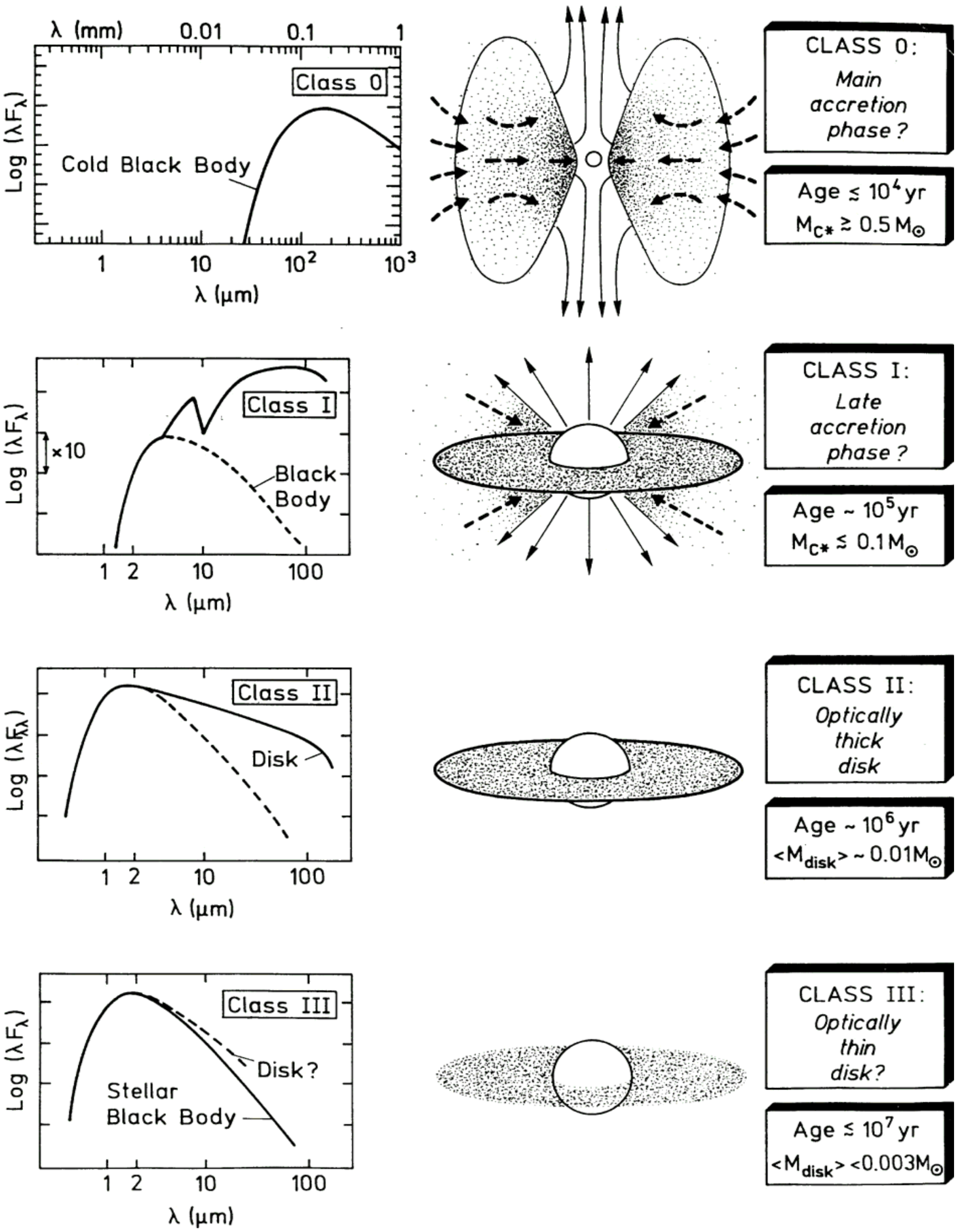

Fig. 2.2.— Evolutionary sequence of the spectral energy distributions for low-mass YSOs (André, 1994; Bachiller, 1996).

2.2 Molecular Clouds

Most of nearby YSOs are clustered at several regions in our Galaxy (mainly on the Galactic plane) with a size of 1–200 pc. These regions are generally invisible in the optical light but show strong radio continuum (mm) and atomic line (CO, HCO^+, etc.) emissions, hence are called “dark clouds” or “molecular clouds” (Figure 2.3: Dame, Hartmann, & Thaddeus, 2001). Molecular clouds contain a large amount of cold gas and dust with a mass of 10^3–10^6 $M_\odot$. In the smaller scale, there are several “molecular cloud cores” with a size and density of 10^3–10^4 AU and 10^4–10^7 cm^{-3}. YSOs are born in those molecular cloud cores. The molecular clouds are therefore often called “star-forming regions”. Many low-mass star-forming regions exist near the solar system (50–200 pc), such as ρ Ophiuchi, Taurus, Chamaeleon, and Lupus. On the other hand, high- and intermediate-mass star-forming regions (Orion, Monoceros R2, etc.) are generally distant (0.5–1 kpc; Figure 2.4).

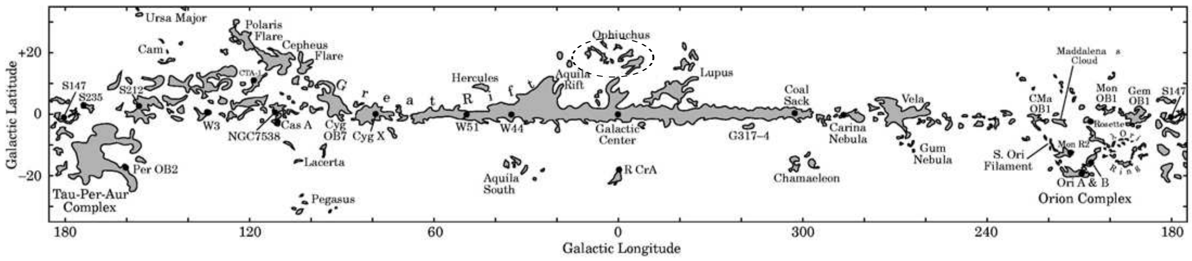

Fig. 2.3.— Molecular cloud map in our Galaxy obtained with velocity-integrated CO intensity (Dame et al., 2001). A dashed ellipse represents the position of the ρ Ophiuchi cloud.

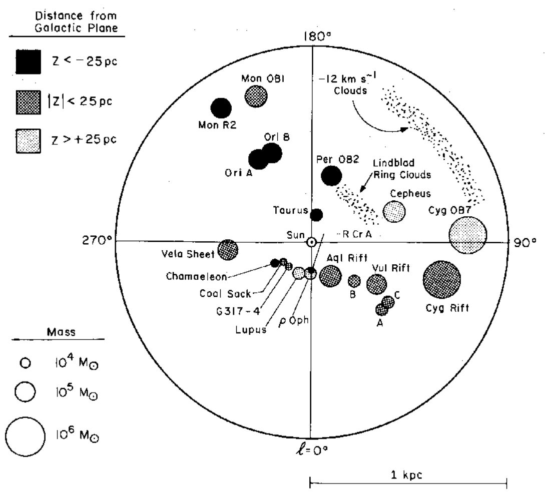

Fig. 2.4.— The distribution of the Galactic molecular clouds (Dame et al., 1987). The circle radius and shading indicate the cloud mass and angular distance from the Galactic plane, respectively.

2.3 X-ray Observations of Low-mass Stars

2.3.1 X-rays from low-mass main-sequence stars

Low-mass MSs emit significant X-rays. The most famous sample of this class is, of course, our sun. There are two origins of the solar X-rays as follows.

Flare

A "solar flare" means a phenomenon in which a large amount of energy (10^{29}–10^{32} ergs) suddenly arises in a surface magnetic loop with timescales from several minutes to hours. First, particles are accelerated at the loop top, then move down along the loop and penetrate into a cold chromosphere. During this phase, the non-thermal particles emit radio (synchrotron) and hard X-ray – γ-ray (bremsstrahlung and nuclear line emission) photons. Cold gas at the chromosphere is abruptly heated to high temperature, then expands and flows up into the loop, which is called "chromospheric evaporation". High temperature (0.1–1 keV) and density ($\sim 10^{10}$ cm^{-3}) plasma fills the loop, then emits thermal X-rays. The plasma gradually cools down due to radiative and conductive energy losses, hence X-ray emission disappears about several hours later (Figure 2.5).

It is obvious that the flare activity has a tight correlation with magnetic field. However, the mechanism to release such large magnetic energy with a short timescale had been a long-standing issue. In 1990's, the Japanese solar X-ray satellite *Yohkoh* brought us key observational evidence. Figure 2.6 (left) shows a *Yohkoh* SXT (soft X-ray telescope) image of the solar flare occurred on February 21, 1992 (Tsuneta et al., 1992). This shows a beautiful cusp-like shape, which is in good agreement with the magnetic reconnection models (Sweet, 1958; Parker, 1957; Petschek, 1964, see also Figure 2.6 right); when a pair of anti-parallel lines of magnetic field crosses each other at the loop top, a reconfiguration of the magnetic field occurs and a large amount of magnetic energy is suddenly released. Now it is widely accepted that magnetic reconnections trigger the solar flares.

Another important issue is the origin of surface magnetic field. The main mechanism for the sun is the standard α-ω dynamo (Parker, 1955, 1970, see also Figure 2.7); poloidal magnetic field makes toroidal field with the effect of differential rotation in a surface convection zone (ω term), and vice versa with the effect of turbulent motion (α term). Theories predict that the boundary between the surface convection zone and the radiative core acts as the anchor point of magnetic field, hence the α-ω dynamo mechanism may not work for sources with fully convective structure such as protostars and brown dwarfs, although a small-scale turbulent dynamo (α^2 dynamo) would be conceivable (Durney et al., 1993).

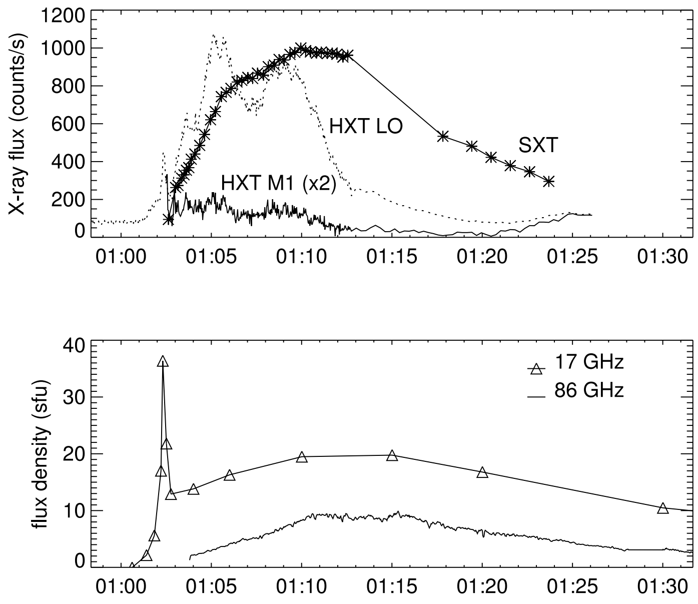

Fig. 2.5.— Multiwavelength light curves of the solar flare occurred on August 17, 1994 (Silva et al., 1996). The top panel shows those in the soft (SXT: 0.25–4.0 keV) and hard (HXT LO: 14–23 keV, M1: 23–33 keV) X-ray bands obtained with *Yohkoh*, while the lower panel shows those in the radio 17 (NRO) and 86 (BIMA) GHz bands.

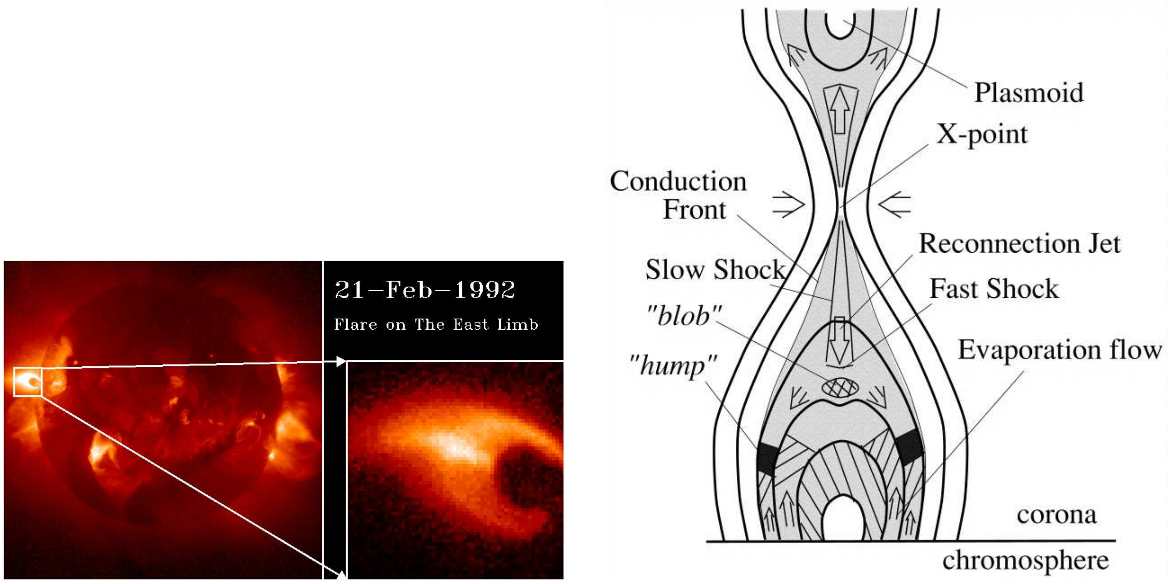

Fig. 2.6.— (left) A *Yohkoh* SXT image of the solar flare occurred on February 21, 1992 (Tsuneta et al., 1992) and (right) schematic view of the magnetic reconnection model (Yokoyama & Shibata, 2001).

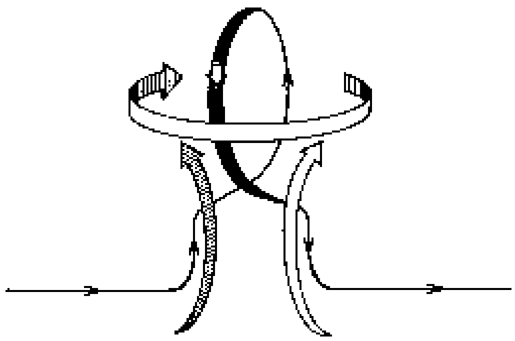

Fig. 2.7.— Schematic view of the α-ω dynamo mechanism (Parker, 1970). Solid line and ribbon arrows represent a magnetic line of force and fluid motion, respectively.

Corona

The sun is covered by hot corona, which also emits X-rays. However, its X-ray properties are quite different from the solar flare X-rays; steady emission from relatively low temperature ($\sim$0.1 keV) and density ($\sim 10^9$ cm^{-3}) plasma. Although the heating mechanism of the corona is still controversial, it is widely accepted that the magnetic field also plays a key role.

2.3.2 X-rays from low-mass young stellar objects

X-rays from T Tauri stars

In 1980's, the *Einstein* and *ROSAT* satellites discovered X-ray emission from many TTSs (Feigelson & DeCampli, 1981; Feigelson & Kriss, 1981; Montmerle et al., 1983; Feigelson & Montmerle, 1999) using the imaging capability at the soft X-ray band (<2 keV). Their X-rays are highly variable with timescales of days or longer and occasionally show flare activities like the sun. X-ray spectra are thermal in origin and are well fitted by a single- or multi-temperature plasma model with temperatures of 0.1–3 keV (Preibisch, 1997). These characteristics are quite similar to the solar X-rays (§2.3.1), hence the origin of X-rays from TTSs would be the same as that of the sun, i.e., magnetic activity at the stellar surface. The X-ray luminosity (L_X) of TTSs is, however, much larger than that of the sun; 10^{29}–10^{31} ergs s^{-1} and 10^{30}–10^{32} ergs s^{-1} for the quiescent and flare phases, respectively (cf., $\sim 5\times10^{26}$ ergs s^{-1} for the solar corona and 10^{27}–10^{31} ergs s^{-1} for the solar flares: Vaiana & Rosner, 1978). Also, L_X of TTSs is well correlated with their bolometric luminosity, stellar mass (Preibisch & Zinnecker, 2002), and possibly with their rotation period (Stelzer et al., 2000), although the underlying physics is still controversial.

X-rays from class I protostars

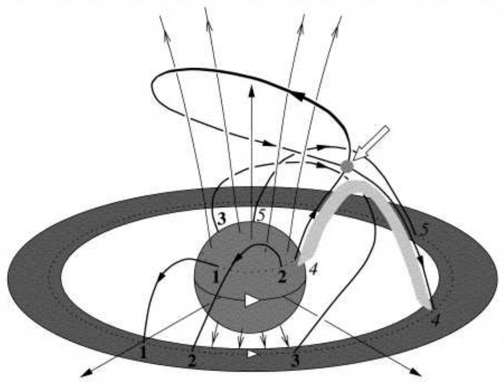

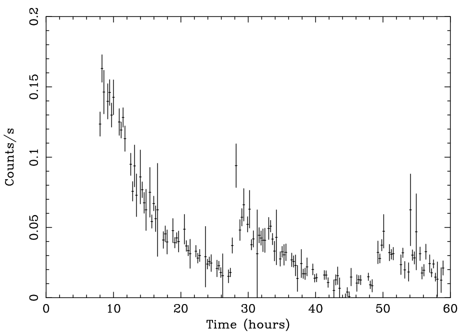

Fig. 2.8.— (left) Schematic view of the star-disk arcade model (Montmerle et al., 2000). Numerals (1–5), solid lines, and thick gray line indicate time sequence, magnetic field, and flare loop after a reconnection. An arrow shows a reconnection point. (right) Quasi-periodic flares from a class I YLW15A in the ρ Ophiuchi cloud obtained with *ASCA* (Tsuboi et al., 2000).

Protostars are deeply embedded in molecular cloud cores and shrouded by dense circumstellar gas and dust, hence we can not observe them even with the soft X-ray band due to large extinction. The Japanese X-ray satellites *Temma* and *Ginga*, however, discovered hard X-ray emission (>2 keV) in the direction of star-forming regions (Koyama, 1987; Koyama et al., 1992). Although they have no imaging capability, X-ray characteristics of flare-like light curves and highly absorbed spectra ($N_{\rm H} \sim 10^{22}$ cm^{-2}) indicate that X-rays are coming from discrete sources inside (or behind) the dense cloud cores.

The forth Japanese X-ray satellite *ASCA* (Advanced Satellite for Cosmology and Astrophysics: Tanaka, Inoue, & Holt, 1994) is the first X-ray mission to have the X-ray telescopes (XRTs: Serlemitsos et al., 1995) with the imaging capability for the hard X-ray photons (2–10 keV), which are less absorbed as the extinction cross-section decreases as $E_{\rm X}^{-2.5}$ ($E_{\rm X}$: X-ray energy). Koyama et al. (1994) first revealed that the hard X-rays from the ρ Ophiuchi dark cloud regions would come from class I sources (WL6 and WL15 = Elias29) with *ASCA*/GIS. Using *ASCA*/SIS, which has better spatial resolution than GIS, Kamata et al. (1997) confirmed the X-ray emission from these class I sources. Independently, Casanova et al. (1995) obtained the hints of X-ray detection from class I in the same star-forming area with *ROSAT*/PSPC. Then the successive observations with *ASCA* further revealed that many class I protostars are X-ray emitters (Koyama et al., 1996; Ozawa et al., 1999; Tsuboi et al., 2000) thanks to its higher sensitivity at the hard X-ray band. *ROSAT* observations also detected X-rays from class I (Grosso et al., 1997; Neuhäuser & Preibisch, 1997; Grosso, 2001). They share the same characteristics of thermal emission with the plasma temperature of 0.5–5 keV and strong variability with occasional rapid flares, which are consistent with the scenario of enhanced solar-type activity, attributable to magnetic dynamo processes.

Class I protostars have fully convective structure, so the standard (α-ω) dynamo mechanism may not work (§2.3.1). As an alternative scenario, Hayashi, Shibata, & Matsumoto (1996) and Montmerle et al. (2000) have proposed a scenario of star-disk connection by one magnetic loop, where the central forming-star rotates faster than the inner edge of its accretion disk (Figure 2.8 left). This well explains characteristic quasi-periodic three flares from a class I YLW15A (Figure 2.8 right: Tsuboi et al., 2000). If this is a real case, the rotation period of YLW15A is surprisingly high of $\sim$ a day (e.g., $\sim$28 day for the sun and 3–10 day for TTSs).

X-rays from class 0 protostars

Recently, the *Chandra* and *XMM-Newton* satellites discovered X-rays from some class 0 systems (or candidates), MMS 2 and 3 in the Orion Molecular Cloud 3 (OMC 3: Tsuboi et al., 2001), IRS5 in L1551 (Favata et al., 2002) and HH2 in the Orion Nebula (Pravdo et al., 2001). Their X-ray properties, however, are different from those of class I–IIIs; (1) there is no significant X-ray variability, and (2) X-ray shapes of IRS5 and HH2 seem to be diffuse and are not located at the central source but near the Herbig-Haro objects, which are shock induced optical emissions (Figure 2.9). As for MMS 2, Tsujimoto et al. (2002a) and Tsujimoto (2003) made follow-up observations with the Subaru and VLA telescopes and found that the X-ray emission is associated with an H_2 outflow of about 500 AU-long emanating from the VLA source. Their X-rays therefore may not be attributable to central sources with the solar-like magnetic activity but are probably associated with the violent outflows of more than 200–1000 km s^{-1} (Pravdo et al., 2001; Favata et al., 2002; Tsujimoto, 2003), although the limited samples and statistics hamper further analyses and discussions.

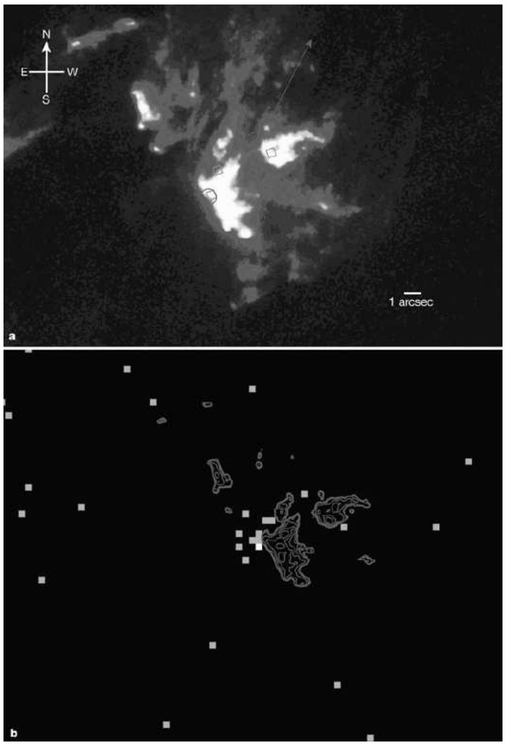

Fig. 2.9.— (top) HST and (bottom) *Chandra* images of HH2 (Pravdo et al., 2001). The contour in the bottom panel is the same as the image in the top panel.

2.3.3 X-rays from brown dwarfs

ROSAT detected X-rays from several young BDs and their candidates in star-forming regions; Chamaeleon, ρ Ophiuchi, and Taurus (Neuhäuser & Comrerón, 1998; Neuhäuser et al., 1999). Also, an old BD LP944$-$20 showed a weak X-ray flare discovered with *Chandra* (Rutledge et al., 2000). Their X-rays are similar to those of low-mass stars and are likely to be magnetic origin. However, the standard (α-ω) dynamo to produce the magnetic activity may not present, because BDs are fully convective like class 0–I protostars.

Chapter 3

Review of the ρ Ophiuchi Cloud

3.1 The ρ Ophiuchi Molecular Cloud

The ρ Ophiuchi molecular cloud (hereafter, ρ Oph) is one of the nearest and most well-known star-forming regions in our Galaxy, which is located about 15° above the Galactic center (Figure 2.3).

The distance to ρ Oph is somewhat uncertain. Chini (1981) made optical–infrared photometric observations and estimated the distance to be 165±20 pc from the mean distance modulus of three bright and heavily reddened stars. Alternatively, Knude & Høg (1998) calculated optical reddening (E_{B-V}) of MS stars and giants using the *Hipparcos* and *Tycho* catalogues, then found an abrupt increase of E_{B-V} for stars with the distance larger than 120 pc. Recently, however, de Zeeuw et al. (1999) proposed the distance of 145±2 pc from the *Hipparcos* positions, proper motions, and parallaxes. In this thesis, we adopt the distance of 145 pc.

The total size of the ρ Oph complex is $\sim$10° × 20° ($\cong$ 25 pc × 50 pc). The ongoing star formation is less active in the north-east region but is concentrated in the south-west region with the size of $\sim$1 pc × 2 pc called "ρ Oph main body". The radio observations of the ρ Oph main body region have been frequently made since 1980's. The $C^{18}O$ J=1–0 (Wilking & Lada, 1983; Tachihara, Mizuno, & Fukui, 2000) and ^{13}CO J=1–0 (Loren, 1989) mappings revealed the distribution of low density molecular gas and were used to estimate the total mass and average density of the main body to be 500–1000 $M_\odot$ and 10^4–10^5 cm^{-3}, respectively. Loren, Wootten, & Wilking (1990) observed higher density gas with DCO^+ emission lines and divided the main body into seven smaller scale cores called ρ Oph A, B1, B2, C, D, E, and F. The scale, mass, and density of these cores are $\sim$0.1 pc, 10–100 $M_\odot$, and 10^5–10^6 cm^{-3}, respectively. The millimeter-submillimeter radio continuum emission (850 μm: Johnstone et al. 2000; 1.3 mm: Motte et al. 1998; see also Figures

3.1, 3.2, and Table 3.1) revealed further smaller scale structure and detected about 60 clumps with the scale and mass of ∼5000 AU (≅0.02 pc) and 0.1–6 $M_\odot$. Within these clumps, new YSOs are generated.

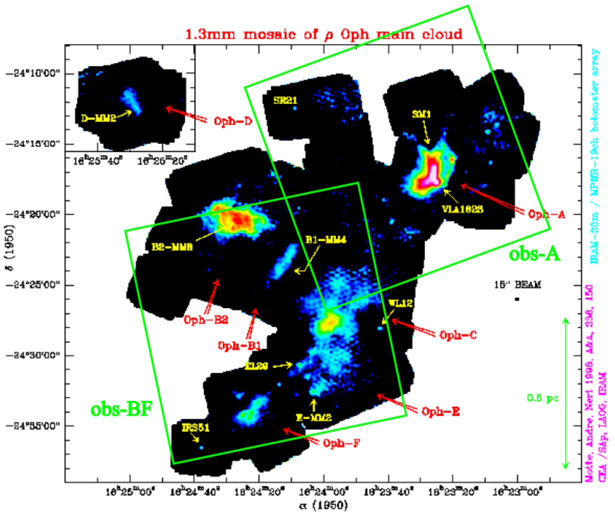

Fig. 3.1.— 1.3 mm radio continuum map of the ρ Oph main body region (Motte et al., 1998). Squares are the fields of view of *Chandra* observations (chapter 5).

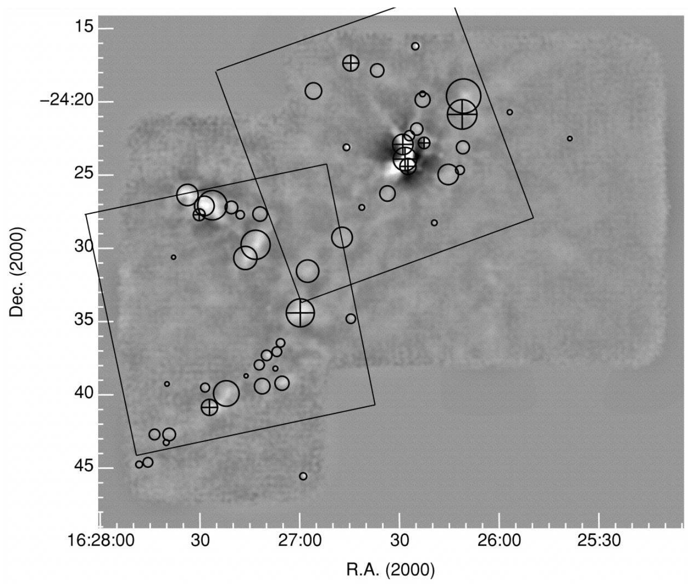

Fig. 3.2.— 850 μm map of the ρ Oph main body region (Johnstone et al., 2000). Circles show the detected clumps. Squares are the fields of view of *Chandra* observations (chapter 5).

3.2 Young Stellar Objects in ρ Oph

The search for YSOs in ρ Oph has been made with several instruments (Table 3.1), using the NIR (Grasdalen, Strom, & Strom, 1973; Vrba et al., 1975; Elias, 1978; Wilking & Lada, 1983; Barsony et al., 1989; Greene & Young, 1992; Strom, Kepner, & Strom, 1995; Barsony et al., 1997) and MIR/FIR (Young, Lada, & Wilking, 1986; Wilking, Lada, & Young, 1989; Bontemps et al., 2001) photometry. Several hundreds of YSOs have been found. Bontemps et al. (2001) made MIR observations with the *ISO* satellite and divided IR sources into 16 class I, 123 class II, and 77 class III sources, which is based on the spectral index from the NIR to MIR bands. Such a sensitive survey at the MIR band has been done for limited star-forming regions, which makes the unambiguous classification of YSOs possible. Luhman & Rieke (1999) obtained K-band spectra of about 100 NIR-bright cloud members and estimated the age and mass ranges of the ρ Oph YSOs to be roughly 0.1–1 Myr and 0.02–3 $M_\odot$.

In addition, there are two class 0 protostars in ρ Oph; VLA1623 and IRAS 16293$-$2422 (André & Montmerle, 1994). They show strong sub-mm emission and CO bipolar outflow (Mundy, Wootten, & Wilking, 1990; André, Ward-Thompson, & Barsony, 1993), which is firm evidence for their class 0 nature. Unfortunately, however, IRAS 16293$-$2422 is located outside of the *Chandra* observed field, hence we do not mention it hereafter.

3.3 Previous X-ray Observations

The first X-ray observation of ρ Oph was made with the *Einstein* satellite (Table 3.1: Montmerle et al., 1983). In the soft X-ray (<2 keV) band image, many TTSs showed X-ray flares. Montmerle et al. (1983) expressed such phenomena as "*the X-ray Christmas Tree*". The X-ray spectra were well fitted by a thin-thermal plasma model with a moderate temperature of $kT \sim$1 keV and absorption of $N_{\rm H} \lesssim 10^{22}$ cm^{-2}. The *ROSAT* satellite further detected soft X-rays from about 50 TTSs and some class I sources (Casanova et al., 1995; Grosso et al., 2000; Grosso, 2001). However, X-ray emission from class I was still controversial due to the large positional uncertainty and limited statistics.

As for the hard X-ray (>2 keV) band, the Japanese *Tenma* and *Ginga* satellites detected significant emission toward the ρ Oph cloud (Koyama, 1987; Koyama et al., 1992). Based on these pioneering results, the *ASCA* satellite observed ρ Oph and made the first hard X-ray image. Some class I sources were identified with hard X-ray emitters (Koyama et al., 1994; Kamata et al., 1997; Tsuboi et al., 2000, Figure 3.3). In particular, a class I source YLW15A showed three quasi-periodic flares with the interval of $\sim$1 day (Tsuboi et al., 2000), which may be evidence for the star-disk arcade scenario and fast rotation of protostars (Montmerle et al., 2000, see also §2.3.2).

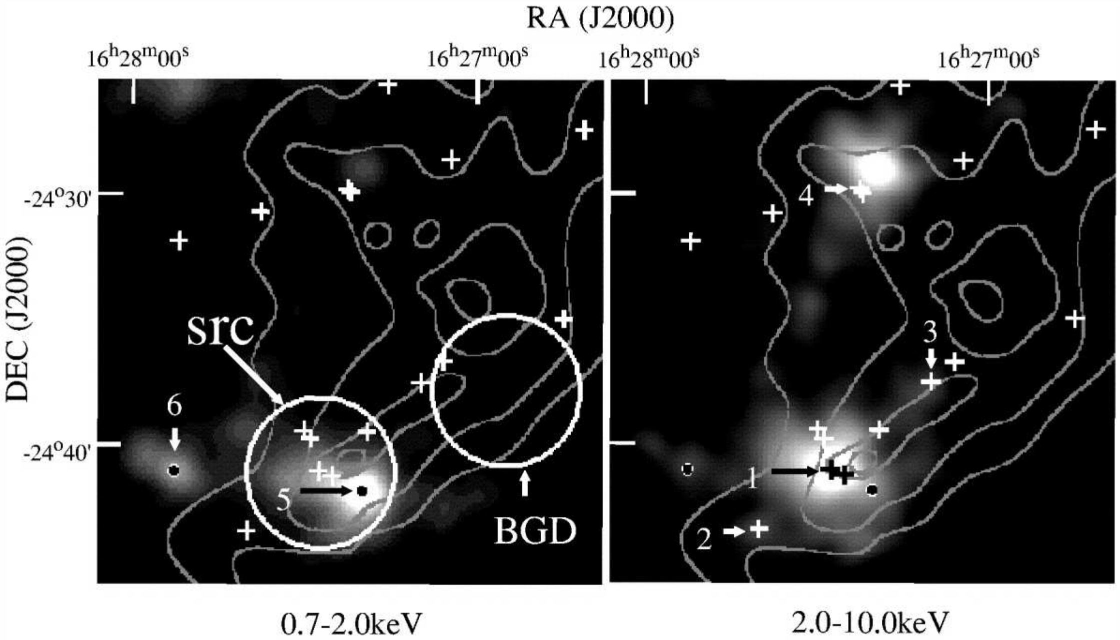

Fig. 3.3.— *ASCA*/SIS images of the central region of ρ Oph in the 0.7–2 (left) and 2–10 keV (right) bands (Tsuboi et al., 2000). The contours are $C^{18}O$ (1–0) density (Wilking & Lada, 1983). Crosses show the position of class I sources. Arrows indicate X-ray detected class I sources (1: YLW15A, 2: IRS51, 3: Elias29), WTTSs (5: ROXs21, 6: ROXs31), and another class I source detected in the previous *ASCA* observation (4: WL6). Circles are source and background regions used for the spectral analysis in Tsuboi et al. (2000).

3.4 γ-ray Emission

The *COS-B* satellite found a γ-ray source 2CG353+16 near the ρ Oph cloud (Swanenburg et al., 1981). The position (J2000) is ($16^h30^m05^s$, $-24°50'06''$) with the error radius of 1.5° and flux (>100 MeV) of 1.1×10^{-6} photons cm^{-2} s^{-1}. One plausible idea about its emission mechanism is that γ-rays are made by the interaction between high-energy cosmic ray nucleons and the interstellar matter in the cloud via pion decay ($\pi^0 \rightarrow 2\gamma$). Xu et al. (1992) proposed that those high-energy cosmic rays were generated by the supernova remnant exploded in the 14th century B.C in this cloud, which was reported in an ancient Chinese record. *EGRET* further found a γ-ray source 3EG J1627−2419, although Hartman et al. (1999) suggested that it may be a possible artifact.

Table 3.1: Multiwavelength source catalogues in the ρ Oph cloud

Instruments	Abbreviation	Area (arcmin^2)	Bandpass	Resolution (arcsec)	Sensitivity	Number of Sources	Ref.
			— Radio —				
VLA	ROS	14000	1.4 GHz	5	1 mJy	58	1
VLA	SFAM	14000	1.4 GHz	5	1 mJy	213	2
VLA	ROC	2500	1.4/5 GHz	5	1 mJy (@1.4 GHz)	59	1
VLA	LFAM	340	5 GHz	0.5	0.09 mJy	35	3
IRAM	···	480	1.3 mm	15	30 mJy	58[*]	4
SCUBA	SMM	700	850 μm	3	0.1 Jy	55	5
			— MIR —				
IRAS	YLW	620	12–100 μm	45	1 Jy (@12 μm)	18	6
IRAS	WLY	1800	12–100 μm	45	0.15 Jy (@12 μm)	64	7
ISO	···	2500	6.7/14.3 μm	3	10 mJy (@6.7 μm)	425	8
			— NIR —				
KPNO	GSS, S	230	K	35	9 mag	41	9
KPNO	VSSG	720	$JHKL$	36	12.0 mag (@K)	31	10
CIT	Elias	65000	$JHKLMNQ$	120	7.5 mag (@K)	50	11
[†]	WL	100	JHK	12	12.1 mag (@K)	20	12
KPNO	BBRCG	140	K	0.78	14.2 mag	61	13
IRTF	IRS	2000	$JHKLMNQ$	7.5	14 mag (@K)	58	7
Steward Obs.	GY	650	JHK	1.8	13 mag (@K)	481	14
Steward Obs.	CRBR	200	HK	1.3	16 mag (@K)	91	15
KPNO	SKS	1200	JHK	1.3	14.2 mag (@K)	119	16
KPNO	BKLT	3600	JHK	1.2	14.5 mag (@K)	4495	17
2MASS	···	···	$JHKs$	0.1	15 mag (@Ks)	~600[‡]	18
			— Optical —				
[§]	···	···	$UBVRI$	···	···	38	19
CTIO	···	140000	Hα	a few	··· [‖]	86	20
La Silla	ROXs	··· [#]	··· [#]	··· [#]	··· [#]	47	21
			— X-ray —				
Einstein	ROXs	14000	0.5–2 keV	45	$10^{29.5}$ ergs s^{-1}	47	22
ROSAT/PSPC	ROXR1	1200	0.1–2.4 keV	15	10^{29} ergs s^{-1}	55	23
ROSAT/HRI	ROXR	800	0.1–2.4 keV	2	10^{29} ergs s^{-1}	63	24
ASCA	ROXA	2000	0.5–10 keV	30	10^{30} ergs s^{-1}	19	25
Chandra	···	600	0.5–9 keV	0.5	10^{28} ergs s^{-1}	195	26

(footnotes for Table 3.1)

*The number of starless cores.

†University of Arizona 1.54 m telescope.

‡The number of sources within $\sim$700 arcmin^2 region of the ρ Oph main body.

§The 123 cm telescope in Cala Alto/Spain and the 50 cm telescope on the Gamsberg in South West Africa. No observational information was given in the paper.

‖Relative Hα intensity was only given.

#Pointing spectroscopic (3700–7500 Å) and photometric ($UBVRI$) observations on *Einstein* X-ray sources (Montmerle et al., 1983).

References – (1) André et al. (1987), (2) Stine et al. (1988), (3) Leous et al. (1991), (4) Motte et al. (1998), (5) Johnstone et al. (2000), (6) Young et al. (1986), (7) Wilking et al. (1989), (8) Bontemps et al. (2001), (9) Grasdalen et al. (1973), (10) Vrba et al. (1975), (11) Elias (1978), (12) Wilking & Lada (1983), (13) Barsony et al. (1989), (14) Greene & Young (1992), (15) Comerón et al. (1993), (16) Strom et al. (1995), (17) Barsony et al. (1997), (18) http://ipac.caltech.edu/2mass/, (19) Chini (1981), (20) Wilking et al. (1987), (21) Bouvier & Appenzeller (1992), (22) Montmerle et al. (1983), (23) Casanova et al. (1995), (24) Grosso et al. (2000), (25) Kamata et al. (1997), (26) This thesis and Imanishi et al. (2003).

Chapter 4

Instrumentation

In this chapter, we show the basic properties of the *Chandra* satellite and its instruments. More details are found in the *Chandra* Observatory Guide[1].

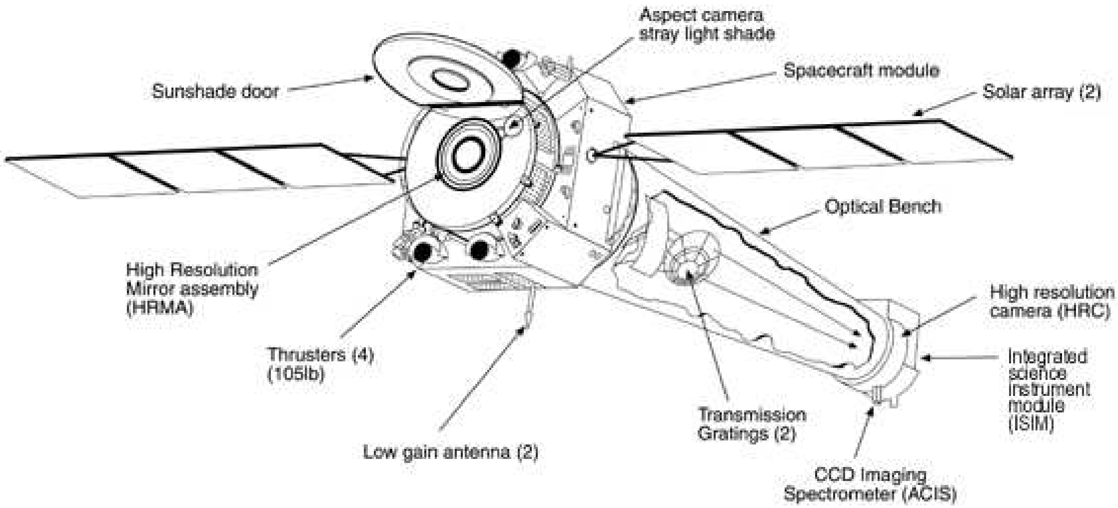

Fig. 4.1.— Schematic view of the *Chandra* satellite (©NASA/CXC/SAO).

4.1 Overview of the *Chandra* X-ray Observatory

The *Chandra* X-ray Observatory (CXO: Weisskopf et al., 2002, Figure 4.1) was launched by NASA's Space Shuttle Columbia on July 23, 1999. The total weight and length are ~5,000 kg and ~10 m. The orbit is elliptical with the perigee and apogee altitudes of ~16,800 km and ~132,000 km,

[1]http://asc.harvard.edu/udocs/docs/docs.html .

respectively. The orbital period is ∼63.5 hours, about 75 % of which are used for observation times.

Chandra is equipped with one large X-ray telescope (HRMA = High Resolution Mirror Assembly; §4.2) and the focal-plane Science Instruments (SIs), consisting of two CCD (Charge Coupled Device, ACIS = Advanced CCD Imaging Spectrometer; §4.3) and microchannel plate (HRC = High Resolution Camera; §4.4) arrays. Also two transmission grating systems (HETG = High Energy Transmission Grating and LETG = Low Energy Transmission Grating; §4.4), which are located between HRMA and SIs, offer observations with high energy resolution. The satellite pointing is controlled by the Pointing Control and Aspect Determination (PCAD) system. Table 4.1 shows basic characteristics of each instrument. The most superior point is the highest spatial resolution (∼0.″5) among the X-ray satellites operated by today.

Dithering

Since HRMA gives the excellent spatial resolution (∼0.″5) comparable to the pixel size of SIs, it sometimes happens that most X-ray photons fall into a certain bad pixel or the gap between the SI chips. In order to avoid them, the spacecraft is dithered during observations in a Lissajous shape. The peak-to-peak amplitude of the dithering is 16″ (ACIS) and 40″ (HRC) and the nominal period is 1000.0/707.1 s (ACIS) and 1087.0/768.6 s (HRC) in the Y/Z axes, respectively. We can correct the dither pattern in ground processing with the PCAD data.

Table 4.1: Basic characteristics of the *Chandra* scientific instruments

Instruments	ACIS-I	ACIS-S	HRC	HETG	LETG
Field of view	∼17′×17′	∼8′×50′	∼30′×30′ (I)	···	···
			∼6′×99′ (S)		
Bandpass	0.5–10.0 keV	0.1–10.0 keV *	0.08–10.0 keV	0.4–10 keV	0.08–2 keV
On-axis Effective area ...	600 cm^2	800 cm^{2*}	200 cm^2	60 cm^2	10 cm^2
	@1.5 keV	@1.5 keV	@1 keV	@1 keV	@1 keV
On-axis spatial resolution	0.″5	0.″5	0.″4	···	···
Energy resolution	130 eV†	200 eV*	1 keV	1 eV	0.1 eV
	@6.0 keV	@6.0 keV	@1 keV	@1 keV	@0.1 keV
Timing resolution	3.2 s‡	3.2 s‡	16 μs	16 μs	16μs

*Values for the backside illuminated (BI) CCD chips.

†Values near the readout node. The energy resolution becomes worse at the further position from the node (see Figure 4.7 right).

‡Values for the Timed Exposure mode with full frames.

4.2 HRMA – High Resolution Mirror Assembly

In spite of their high penetrating power, most X-rays can be reflected if the incident angle is smaller than a critical value of $\lesssim 1°$. HRMA consists of four pairs of Wolter Type-I mirrors, a combination of parabolic and hypabolic shells, which realize small incident angles (Figure 4.2). The mirrors are made of Zerodur glass polished and coated with iridium. The diameters of the mirrors are from 0.65 to 1.23 m and the focal length is 10.066 m. In order to keep high accuracy of the mirror surface, the glass is very thick with the total mass of ∼1,500 kg.

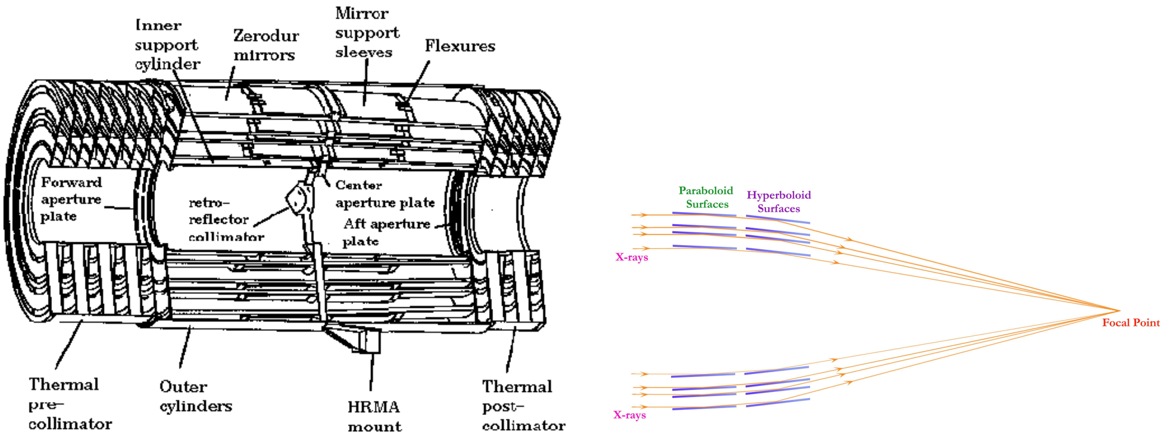

Fig. 4.2.— (left) Schematic view of The HRMA mirrors. (right) Wolter type-I optics (©NASA/CXC/SAO).

Effective area

Figure 4.3 shows the HRMA effective area, which is ∼800 cm^2 at the photon energy of 1 keV and ∼100 cm^2 at 8 keV. It gradually decreases as the source off-axis angle becomes larger. These values are almost comparable to those of *ASCA* and slightly smaller than those of *XMM*-Newton.

Point spread function and encircled energy fraction

Figure 4.4 shows the shape of the point spread function (PSF) of HRMA and the fraction of encircled energy at the on-axis position. The point source image is nearly circular and very sharp. The half power diameter (HPD) is $\sim 0''.5$ (at 1.49 keV) and about 90 % of the photons are concentrated in a $2''$ diameter. The PSF gets elongated in an elliptical shape as the off-axis angle becomes larger (Figure 4.5), which is due to the aberrations of Wolter type I optics and the different shapes in focal surfaces among the four mirrors. The HPD thus becomes large as a function of the off-axis angle (Figure 4.5 right).

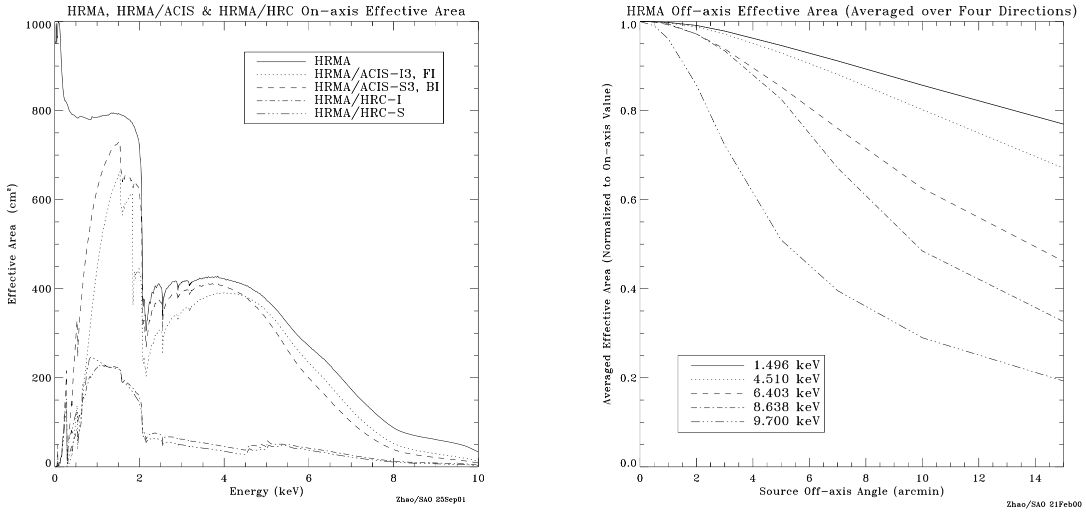

Fig. 4.3.— The effective area of HRMA plotted against (left) X-ray energy and (right) a source off-axis angle. The sudden drop-off seen around 2 keV (left) is due to the M-edge of iridium used for the mirror coating. The values multiplied by the quantum efficiency of ACIS and HRC are also shown in the left panel.

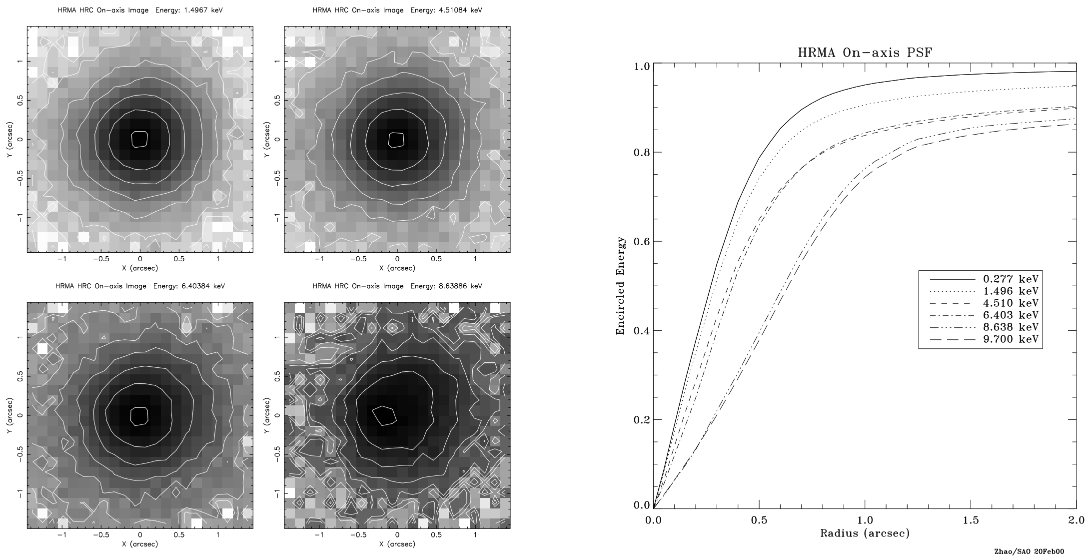

Fig. 4.4.— (left) On-axis PSF of HRMA with the photon energies of (top-left) 1.49, (top-right) 4.51, (bottom-left) 6.40, and (bottom-right) 8.63 keV. (right) The fraction of encircled energy of HRMA as a function of the angular radius at the on-axis position.

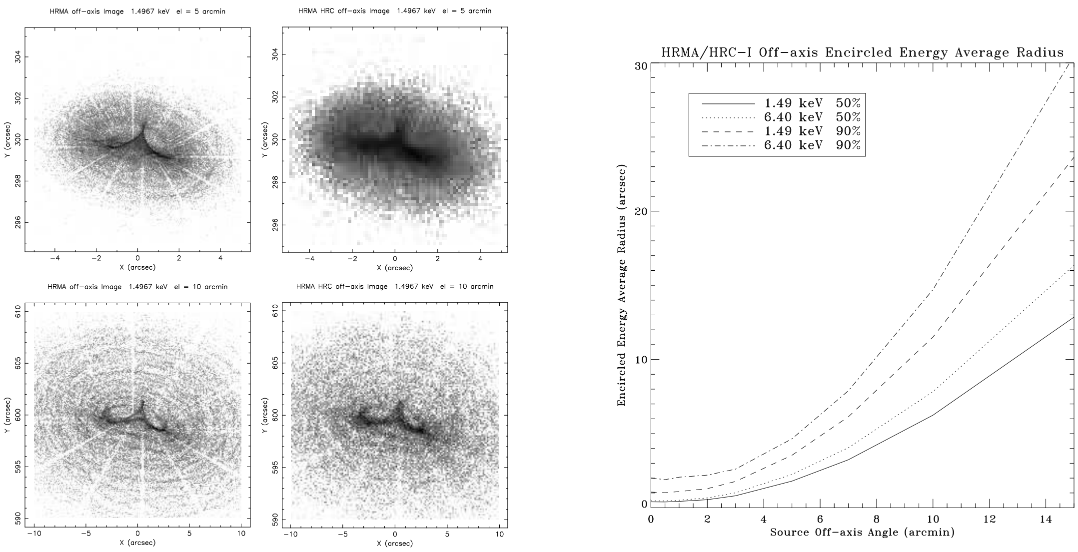

Fig. 4.5.— (left) Off-axis PSF with the photon energy of 1.49 keV. The difference between the top and bottom panels is the off-axis of $5'$ and $10'$, while that between the left and right panels are those of HRMA only and of HRMA/HRC-I, respectively. (right) The fraction of encircled energy of HRMA as a function of source off-axis angle.

4.3 ACIS – Advanced CCD Imaging Spectrometer

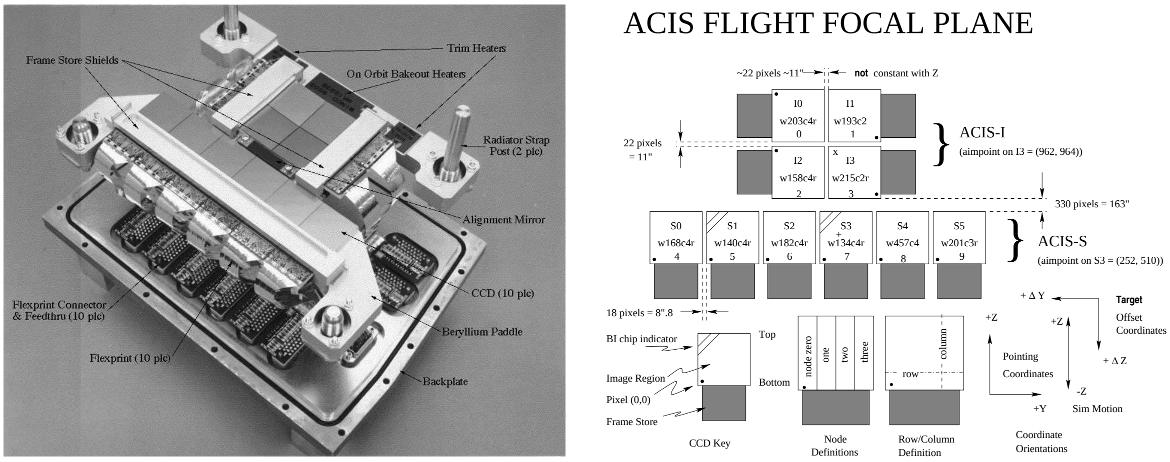

Fig. 4.6.— (left) photographic and (right) schematic view of the ACIS array. The legend of the terminology (right panel) is given in the lower left. The x and cross positions represent the nominal aimpoints of the ACIS-I and ACIS-S arrays.

The ACIS array (Figure 4.6) consists of ten CCDs (Charge Coupled Devices) with 1024 × 1024 pixels each. ACIS-I (chip I0–I3) is laid out in 2 × 2 and is used for imaging observations, while ACIS-S (chip S0–S6) is in 1 × 6, which is optimized for both imaging and grating-spectroscopic observations. The pixel size is 24 μm × 24 μm, corresponding to the angular size of $0''.5 \times 0''.5$. Two CCDs in the ACIS-S array (chip S1 and S3) are back-illuminated (BI) and the others are front-illuminated (FI). For each observation, we can use any six CCDs simultaneously.

Energy resolution

Figure 4.7 (left) shows the energy resolution (ΔE) of ACIS estimated by ground calibrations. The FI chips have a good resolution near the theoretical limit ($\sim$120 eV @ 5.9 keV), while that of the BI chips is slightly poor. After the launch, however, the ACIS-I chips were significantly damaged by low energy protons encountered during radiation belt passages. These protons made many charge traps at buried channels, which cause the increase of charge transfer inefficiency (CTI). Consequently, ΔE becomes worse as a function of source positions from the readout nodes; $\Delta E \sim$ 130 eV (@ 5.9 keV) near the readout nodes, while $\Delta E \sim$ 330 eV (@ 5.9 keV) at the edge of the chip. Since the gate structure of the BI chips (S1 and S3) is at the opposite side to HRMA, ΔE of the BI chips remains at their pre-launch value and has little dependence on the source position. Now ACIS is not operated and not left at the focal position during the radiation belt passages, hence no further degradation of CTI is expected. Furthermore, in order to reduce the effect of CTI, the CCD temperature is lowered from −90 °C to −120 °C.

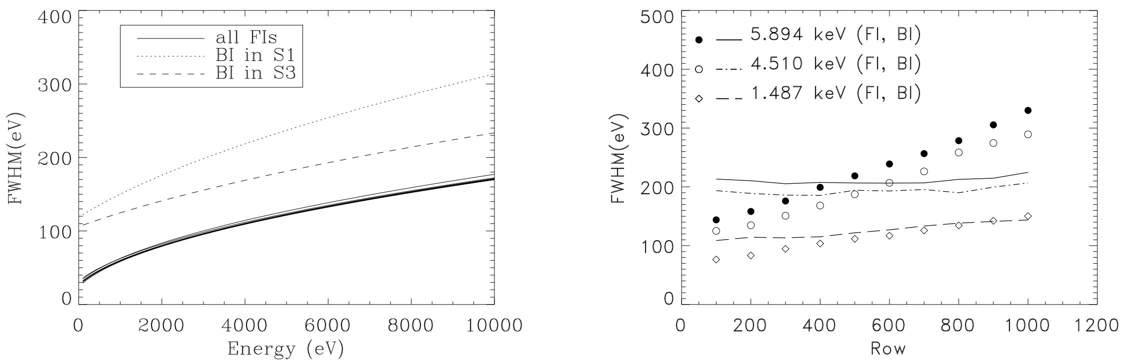

Fig. 4.7.— (left) The pre-launch energy resolution of ACIS. (right) The energy resolution of chip S3 and I3 as a function of row number, after the proton damage on orbit. The data were taken at the CCD temperature of −120 °C.

Quantum efficiency and effective area

Figure 4.8 shows the quantum efficiency of ACIS (left) and the combined effective area of HRMA and ACIS (right). A large fraction of low energy X-rays is absorbed at the optical blocking filter (OBF) and the gate structure for FI chips, hence the efficiency becomes worse at the lower energy. Since the gate of BI chips is at the opposite side to HRMA, the efficiency of BI chips at the low energy band is about two times better than that of FI chips. Due to the effect of CTI, the quantum efficiency at the further side from the readout node is about 5–15 % worse than that near the node. The energy ranges with the effective area of larger than 10 cm^2 are ~0.5–10.0 keV and ~0.1–10.0 keV for FI and BI chips, respectively.

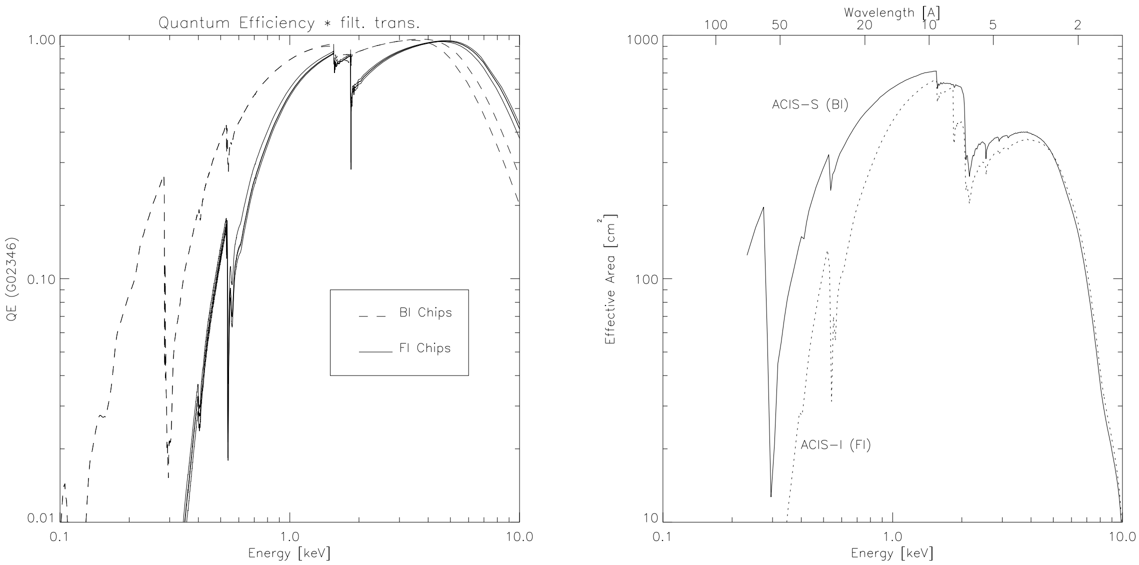

Fig. 4.8.— (left) The quantum efficiency of ACIS with the transmission of OBF. (right) The combined effective area of HRMA and ACIS. The sudden drop-off seen around 1.8 keV is due to the K-edge of silicon.

Event grade

X-ray events are selected with the criterion that the bias-subtracted pixel value exceeds the event threshold (38 ADU ≅ 140 eV and 20 ADU ≅ 70 eV for FI and BI chips) and is the highest among the neighboring 9×9 pixels. In order to distinguish real events from background ones and to estimate the total number of electrons including those leak into the neighboring pixels, the grade method is used. Its algorithm is basically the same as the *ASCA*/SIS grade method (Burke et al., 1991), but ACIS gives the specified numbers for each pixel around the event pixel (Figure 4.9) and determines the grade by summing up those pixel numbers that have a pixel value larger than the split threshold (13 ADU; if the neighboring pixel has larger pixel value than the split threshold, it is regarded as the leaking pixel). Table 4.2 gives the relationship of the *ASCA*/SIS and ACIS grading schemes. Usually, we regard the grades corresponding to the *ASCA*/SIS grades 0, 2, 3, 4, and 6 as real events.

32	64	128
8	0	16
1	2	4

Fig. 4.9.— Schematic for determining the ACIS grade. For example, an event that caused all pixels to exceed their threshold is grade 255. A single pixel event is grade 0.

Table 4.2: Relation between the *ASCA*/SIS and ACIS grades

ASCA/SIS grade	ACIS grade
0	0
1	1, 4, 5, 32, 33, 36, 37, 128, 129, 132, 133, 160, 161, 164, 165
2	2, 34, 64, 65, 68, 69, 130, 162
3/4	8, 12, 16, 17, 48, 49, 136, 140
5	3, 6, 9, 13, 20, 21, 35, 38, 40, 44, 52, 53, 96, 97, 100, 101, 131, 134, 137, 141, 144, 145, 163, 166, 168, 172, 176, 177, 192, 193, 196, 197
6	10, 11, 18, 22, 50, 54, 72, 76, 80, 81, 104, 108, 138, 139, 208, 209
7	All other grades

Operating mode

Two operating modes are available for ACIS. In this thesis, we only use the data of Timed Exposure mode with full frames and the frame time of 3.2 s.

- **Timed Exposure (TE) mode**
  The 1024 × 1024 active region of the CCD is exposed for a selected time interval (frame time), then the collected charge quickly (∼41 ms) transfers to the framestore region. For the entire CCD (full frames), the frame time is 3.2 s, which is the nominal timing resolution of ACIS. In order to obtain better timing resolution or to avoid the pileup effect (see below), we can select subarray mode; the active region is limited to 1/2, 1/4, or 1/8 subarray, which shortens the frame time to 0.4 s at the minimum.

- **Continuous Clocking (CC) mode**
  CC mode achieves high timing resolution (3 ms) but has only one dimension of spatial resolution. Data are continuously clocked through the CCD and framestore to minimize the readout time, with one-dimensional (1 × 1024 pixels) images.

Telemetry format

Three telemetry formats are available as follows. Table 4.3 lists the operating modes, associated formats, and approximate event rates at the telemetry saturation. The faint and very faint formats were used for obs-BF and obs-A, respectively (§5.1).

- **Graded**
  This provides event positions in detector coordinates, event amplitudes, arrival times, and event grades.

- **Faint**
  This provides the same information as the Graded format other than the event grades. Alternatively, this supplies all information about 3 × 3 pixels around the event pixel. The bias map (zero level of each pixel) is telemetered separately.

- **Very Faint**
  This is basically the same as the Faint format, but provides all information about 5 × 5 pixels around the event pixel. This format is used for the TE mode only and offers the advantage for minimizing the background after ground processing, but is limited for low-count sources (Table 4.3).

Event pileup

For bright sources, two or more X-ray photons are often registered in a single ACIS pixel within one readout cycle, which is called pileup. It causes an artificial spectral hardening and underestimate of the X-ray counts. In fact, the brightest two sources in the ρ Ophiuchi cloud (A-2 and BF-64, see chapter 5) suffered the pileup effect. It can be reduced by selecting a proper observing mode (e.g., shorten the exposure time).

Table 4.3: Telemetry saturation limits of ACIS

Mode	Format	Bits/event	Events/s*
CC	Graded	58	375.0
CC	Faint	128	170.2
TE	Graded	58	375.0
TE	Faint	128	170.2
TE	Very Faint	320	68.8

*The number of events per 1 s at the telemetry saturation.

4.4 HRC, HETG, and LETG

We do not use these three instruments in this thesis, hence only show their basic characteristics.

HRC – High Resolution Camera

HRC is a microchannel plate instrument consisting of two detectors like ACIS; HRC-I for imaging and HRC-S for imaging and grating spectroscopy. HRC has larger field of view ($30' \times 30'$) and better time resolution (16 μs) than ACIS, although the energy resolution (ΔE/E $\sim$1 @ 1 keV) is largely limited.

HETG – High Energy Transmission Grating

HETG is designed for grating spectroscopy. The transmission grating inserted between HRMA and the focal plane detector (ACIS-S and HRC-S) disperses incident X-ray photons. Although the two dimensional image is not available, spatial information along the detector can be converted to the photon energy because the dispersion distance from the aimpoint is a function of energy (wavelength) of X-ray photons, which attains high energy resolution ($\Delta E/E \sim$ 1000 @ 1 keV). HETG consists of two gratings; MEG (= Medium Energy Grating; energy range = 0.4–5.0 keV) and HEG (= High Energy Grating; 0.8–10.0 keV).

LETG – Low Energy Transmission Grating

The mechanism of LETG is basically the same as HETG, but is designed to cover the lower energy range (0.08–2 keV). Usually, LETG is used with HRC-S as the focal plane detector.

Chapter 5

Chandra Observations of the ρ Ophiuchi Cloud

5.1 Observations and Data Reduction

Table 5.1: Log of the *Chandra* ACIS-I observations of the ρ Oph main body

Obs.ID	Sequence ID	Observation Date (UT)		Pointing Direction (J2000)*		Exposure†
		Start	End	R.A.	Decl.	(ks)
BF ...	200060	2000 Apr 13 18:33	Apr 14 23:14	$16^{h}27^{m}18\overset{s}{.}1$	$-24°34'21\overset{''}{.}9$	100.6
A	200062	2000 May 15 23:35	May 17 03:18	$16^{h}26^{m}35\overset{s}{.}3$	$-24°23'12\overset{''}{.}9$	96.4

*The position of the detector aimpoint (the telescope optical axis).

†The live time corrected from deadtime.

Chandra made two long-exposure observations on ρ Oph with the ACIS-I array (Table 5.1). The fields of view for the ACIS observations are shown in Figure 3.1, which cover the almost entire 1 pc $\times$ 2 pc region of the ρ Oph main body. The first observation (here and after, obs-BF) is aimed at the south-east $17\overset{'}{.}4 \times 17\overset{'}{.}4$ area including the millimeter cores B, C, E, and F, while the second observation (obs-A) covered the north-west area centered on core A (Loren et al., 1990; Motte et al., 1998). Although some of the ACIS-S chips were simultaneously in operation, we do not use these data except for some bright sources (chapter 6), because large off-axis angles cause degeneration of sensitivity and position determination. From the *Chandra* X-ray Center (CXC), we retrieve the level 2 data, in which the data degradation caused by the increase of CTI in orbit was corrected. The X-ray events were selected with the *ASCA* grades 0, 2, 3, 4, and 6 (Table 4.2).

The afterglow events were also removed. After the processing, each observation yields a ≈100 ks live time (Table 5.1).

5.2 Image and Source Extraction

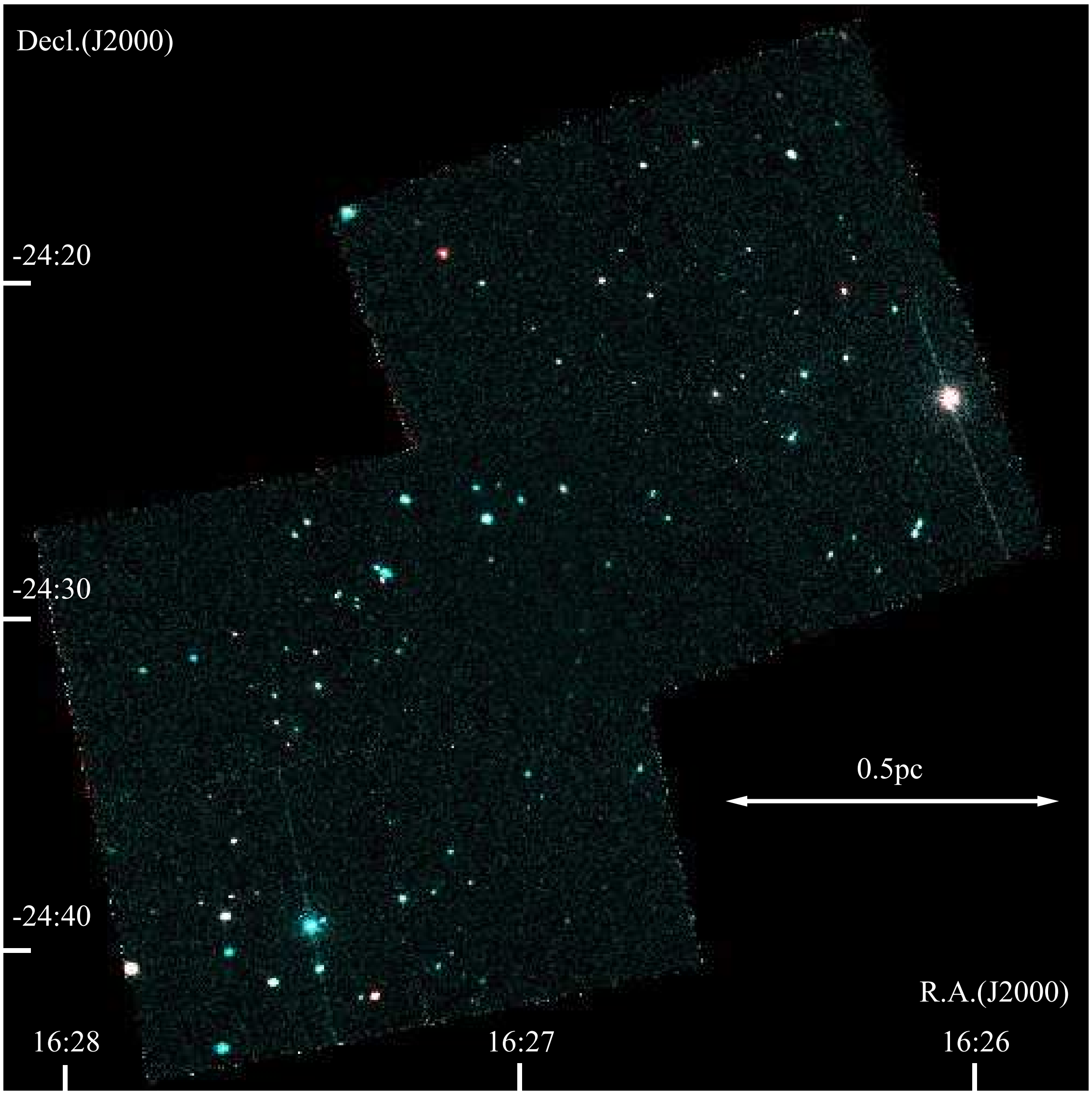

Fig. 5.1.— False-color ACIS image of the ρ Oph cloud. Red and blue colors represent photons in the soft (0.5–2.0 keV) and hard (2.0–9.0 keV) bands, respectively.

Figure 5.1 shows the ACIS-I false-color image of the ρ Oph cloud. Red and blue colors represent photons in the soft (0.5–2.0 keV) and hard (2.0–9.0 keV) X-ray bands, respectively. First, we conduct the source detection analysis for 2048 pixel × 2048 pixel images with the pixel size of $0''.5$ using the `wavdetect` command (Freeman et al., 2002) in the CIAO 2.2.1 package. We set the wavelet scales ranging from 1 to 16 pixels in multiples of $\sqrt{2}$ and the significance criterion at 10^{-6}, which means that the expected false identification of the event pixel is one out of 10^6 pixel image. The `wavdetect` analysis is separately applied for the total (0.5–9.0 keV), soft (0.5–2.0 keV), and hard (2.0–9.0 keV) X-ray bands.

We then detect 195 X-ray sources, nine of which are found in both observations. Thirteen and nine sources are exclusively found only in the soft and hard bands, respectively (hereafter, the "soft-band sources" and "hard-band sources"). Table 5.2 (column [1]–[4]) shows the name, background-subtracted ACIS-I counts, and coordinate for each source (after the offset correction, see §5.3). The soft-band and hard-band sources are indicated by the prefix "S" and "H", respectively. The X-ray photons are extracted from a circle of $1''.2$–$23''.3$ radius depending on the point spread function (PSF) radius for 1.49 keV photons, which is a function of the angular distance from the optical axis of the telescope (psfsize20010416.fits[1] in the CIAO 2.2.1 package). Typically, in the source radius, ≈95 % X-ray photons are included. In order to obtain a high signal-to-noise ratio for some faint sources, we use a circle of a half radius of the PSF. For A-48, we use a larger circle ($5''$) than the PSF because of its diffuse-like feature (§6.6.2). Background counts are extracted from circles respectively of 38 arcmin^2 and 57 arcmin^2 source-free regions in the ACIS-I fields of obs-A and obs-BF.

In order to check possible false sources with the `wavdetect` procedure (Feigelson et al., 2002), we estimate the confidence level (CL) of the X-ray counts using the Poisson statistics (see §6.4). Then 14 sources have the CL smaller than 99.9 %. Although A-48 and A-H2 have significantly high CL, these may also be possible false sources because of its larger source size than the PSF radius (A-48) and of the severe contamination from A-2 (A-H2). We hence note that 16 sources are marginal detections, and label them with (m) in column [2] of Table 5.2.

5.3 Identification and Offset Correction

We search for NIR counterparts of the X-ray sources and estimate the absolute positional offsets of the *Chandra* observations. For reference of NIR sources, we use the Point Source Catalog in the 2MASS Second Incremental Data Release (Cutri et al., 2000) not in Barsony et al. (1997) used in Imanishi et al. (2001a), because the former has better position accuracy ($\sigma \sim 0''.1$) than the latter

[1]This file was constructed by using the SAOsac raytrace code (Jerius et al., 1995).
See also http://asc.harvard.edu/chart/.

(Barsony et al. 1997, $\sigma \sim 1.''2$) with comparable sensitivity ($K \lesssim 14.5$ mag).

We find the NIR counterparts for about 60 % of the X-ray sources within a $5''$ radius circle. Using these *Chandra*-2MASS pairs, we determine and shift the absolute positions of the *Chandra* sources so that the mean values of the *Chandra*-2MASS offset in the direction of right ascension and declination become zero. The systematic positional offset of the *Chandra* frame is (ΔR.A., ΔDecl.) = ($+0.''004$, $+0.''948$) for obs-A and ($-0.''045$, $+0.''802$) for obs-BF, respectively (Figure 5.2). After the offset correction, we repeat the same procedure for the 2MASS counterpart search. Figure 5.3 shows the resultant offset between *Chandra* and 2MASS sources plotted against their off-axis angle. For the sources within the off-axis angle of $5'$, all *Chandra*-2MASS pairs have smaller positional offset than $1''$. However, it becomes larger as a function of the off-axis angle due to the degeneration of position determination. Here, we pick up the *Chandra*-2MASS pairs located below the dashed line in Figure 5.3, which represents the half-power radius for 1.49 keV X-ray photons (Figure 4.5). For remaining sources, we further search for counterparts using other NIR catalogues, then identify an X-ray source BF-90 with GY322 (Greene & Young, 1992). We also regard the counterparts of A-34 to be the nearest NIR source in spite of larger separations than that of the standard criterion (Figure 5.3, see also §6.3.4). Finally, we conclude that 110 out of 195 X-ray sources have NIR counterparts. The offset between the X-ray and NIR sources is shown at column [2] in Table 5.3. We also search for radio (cm) and X-ray counterparts in published catalogues (columns [3]–[7] in Table 5.3).

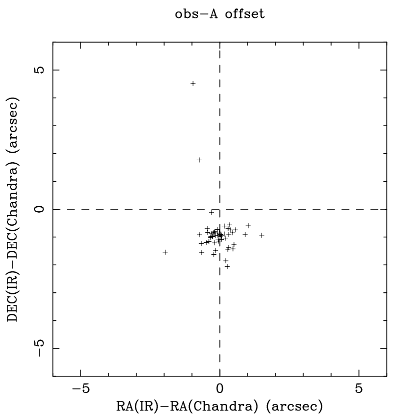

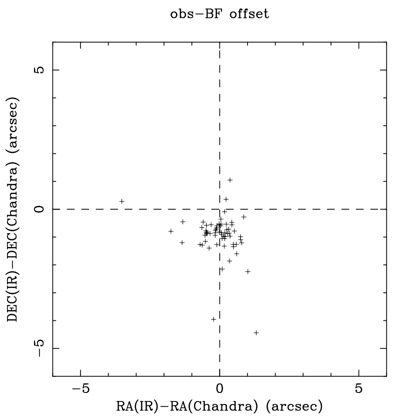

Fig. 5.2.— Offset between the *Chandra* and 2MASS sources for (left) obs-A and (right) obs-BF, before the offset correction (see text).

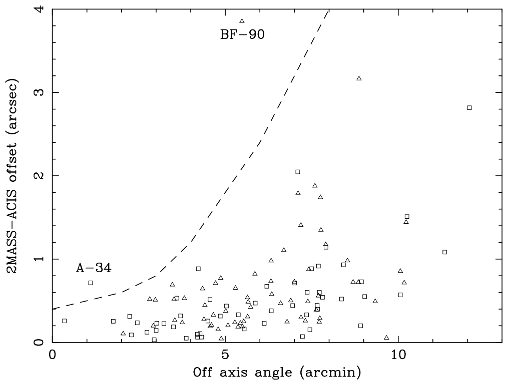

Fig. 5.3.— Offset between the *Chandra* and 2MASS sources (after the offset correction) plotted against their off-axis angle. Squares and triangles represent the X-ray sources in obs-A and obs-BF, respectively. The dashed line is the half-power radius of the PSF for 1.49 keV X-ray photons (Figure 4.5).

5.4 Source Classification

Column [9] in Table 5.3 shows the IR classification based on the spectral indices from the NIR to MIR band (ISOCAM survey at 6.7 and 14.3 μm; Bontemps et al. 2001). Imanishi et al. (2001a) used the terminology class I_c (class I candidate) for sources previously classified as class I (or flat spectrum source). In this thesis, however, we regard all class I_cs as class II, following Bontemps et al. (2001). Furthermore, we define some additional classes as follows.

1. Class III candidates (III_c) are selected among unclassified NIR sources, which are located within the CS contours (Table 5 in Bontemps et al., 2001).

2. Brown dwarfs (BD) and candidates (BD_c) mean sources with the upper limit of the mass below the hydrogen-burning limit of 0.08 $M_\odot$ and with the lower limit of the mass below 0.08 $M_\odot$, respectively (Wilking, Greene, & Meyer, 1999; Cushing, Tokunaga, & Kobayashi, 2000).

3. Foreground stars (F) are selected with the optical color-color diagram and photometric parallaxes (Festin, 1998).

4. Remaining NIR sources are represented by "?", which we call "unclassified NIR sources".

5. Sources with no NIR counterpart are called "unidentified sources", which are labeled by no data point (...). Most of the unidentified sources are thought to be background extragalactic sources (§6.6), although some fractions would be faint cloud members (§6.5).

We then list 8 class Is, 58 class IIs, 17 class IIIs, 9 class III_cs, 2 BDs, 3 BD_cs, 1 F, 12 unclassified NIR sources, and 85 unidentified sources. Hereafter, we use the terminology "class III+III_c" by combining the class III and class III_c for brevity.

5.5 Timing Analysis

We make two X-ray light curves in 0.5–9.0 keV for all *Chandra* sources (background is not subtracted) with the respective time bin of 2000 and 4000 s. The source regions are basically the same as those used in the estimation of the source counts (§5.2). Unfortunately, the brightest two sources (A-2 and BF-64) suffer the photon pileup effect (§4.3), hence we use annulus of $2''.5$–$12''.5$ and $2''.5$–$7''.5$ radii for A-2 and BF-64, respectively. The light curves show many flare-like events. We define a "flare time bin" by the following criterion:

$$\frac{N - N_0}{\Delta N} \geq 2, \tag{5.1}$$

where N, ΔN, and N_0 are the X-ray counts, the statistical 1 σ error, and average counts in a 20000 s interval including the relevant time bin, respectively. If the above criterion is satisfied for both of the two light curves (2000 s and 4000 s time bin), we define the event to be a "flare". Then we pick up 71 flares (Table 5.4). The light curves of the flaring sources are shown in Appendix A. Most flares have the typical profile of those of low-mass main-sequences and YSOs; fast-rise and slow-decay, while some sources show unusual flares having slow rise timescale; e.g., BF-64 = YLW16A (Figure A.1). We fit the rise and decay phases of the flare by a simple (exponential + constant) model using the QDP command in the LHEASOFT 5.0[2], and derive respective e-folding times and quiescent level (τ_r, τ_d, and Q; Table 5.4) with their 90 % errors, where the flare peak time (t_p) is fixed to be the maximum time bin except for the second flare of BF-64. Evidently, this simple model can not reproduce the unusually giant flare from BF-64 even if we relax t_p to be free. However, we do not intend to make a model of the flare light curve and only have interested in the typical timescales, hence do not discuss this discrepancy in further detail.

5.6 Spectral Analysis

X-ray spectra are made for all *Chandra* sources. For the flaring sources, we make the spectra separately in the quiescent and flare phases. The flare phase is the time from $(t_p - \tau_r)$ to $(t_p + \tau_d)$. The quiescent phase is that outside of the flare phase. Background regions are the same as used in §5.2. We then fit them by a thin-thermal plasma model (MEKAL: Mewe et al. 1985; Kaastra 1992; Liedahl et al. 1995) with the photoelectric absorption (WABS: Morrison & McCammon 1983). The metal abundance (Anders & Grevesse, 1989) is well determined only for bright sources. Figure 5.4 shows the histogram of the best-fit abundance for sources with the total X-ray photons larger than 1000 counts. We exclude A-2, BF-64, BF-46, and BF-96 in this figure, because of the pileup effect for the first two sources and their complex spectral shapes for the last two sources (§6.2). The

[2]see http://heasarc.gsfc.nasa.gov/docs/software/lheasoft/.

abundance is spread around 0.3 solar, which is consistent with the previous *ASCA* results (Koyama et al., 1994; Kamata et al., 1997). We therefore fix the abundance to be 0.3 solar unless otherwise noted, because photon statistics are generally limited. The free parameters are the time-averaged plasma temperature ($< kT >$), emission measure ($< EM >$), and absorption column ($N_{\rm H}$). If the temperature is not constrained, which is often the case for very faint sources, we fix the temperature at two representative values of 1 keV (typical of the quiescent state of TTSs; see Figure 7.4) and 5 keV (typical of the flare state of protostars), then estimate respective absorptions and luminosities. For the nine sources detected in both observations, we derive the parameters of each spectrum assuming the same absorption. This simple model is generally acceptable. BF-46 (ROXs21) and BF-96 (ROXs31), however, need multi-temperature spectra with unusual abundances (§6.2). A-23, A-24 and BF-10, on the other hand, require overabundances (§6.3.2, §6.3.3, and §6.3.7). In Table 5.2 (columns [5]–[9]), we summarize the best-fit parameters; $< kT >$, $< EM >$, $N_{\rm H}$, flux, and time-averaged luminosity ($< L_X >$) in 0.5–9.0 keV.

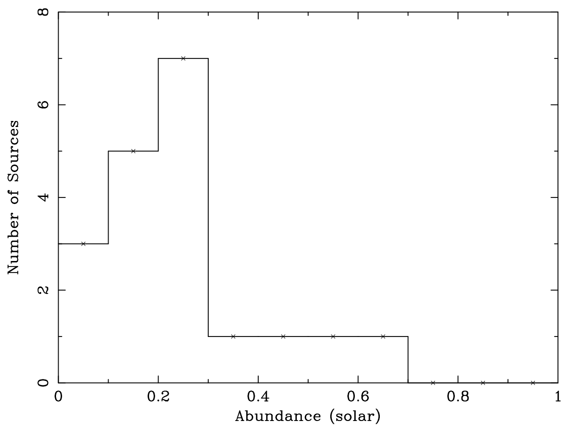

Fig. 5.4.— Histogram of the best-fit abundance for bright sources with total X-ray photons larger than 1000 counts.

5.7 The Catalogue of X-ray Sources in ρ Oph

Here, we present catalogues of 195 *Chandra* X-ray sources in ρ Oph and detected X-ray flares. These are an upgraded version of those in Imanishi et al. (2001a) and also will be presented in Imanishi et al. (2003). Table 5.2 shows the positions and basic X-ray parameters, while Table 5.3 shows identifications of each X-ray source with the previous IR, radio, and X-ray observations. The detected X-ray flares and their fitting parameters are listed in Table 5.4.

5.7.1 *Chandra* X-ray sources in ρ Oph

Table 5.2:: *Chandra* X-ray sources in the ρ Oph region

No.	Counts[*]	R.A.[†] (J2000)	Decl.[†] (J2000)	$< kT >$[‡] (keV)	log($< EM >$)[‡] (cm^{-3})	N_H[‡] (10^{22} cm^{-2})	Flux[§]	L_X[§]	Red-χ^2[‖]	Comment
A-1[#]	13.0(m)	25 55.22	25 37.3	1.0(fixed)	53.6(51.9–56.3)	45.5(>6.7)	0.5	38.4	0.40(2)	
				5.0(fixed)	51.6(50.7–53.2)	15.0(1.6–129.3)	0.6	0.6	0.31(2)	
A-2[**]	79359.2[††]	26 03.02	23 36.1	2.9(2.8–3.0)	54.8(54.8–54.9)	1.1(1.0–1.1)	1257.2	602.5	1.51(436)	Flare1
				2.8(2.7–2.9)	54.8(54.8–54.8)	...	1016.0	493.6	...	Flare2
A-3	829.9	26 07.05	27 24.4	2.1(1.8–2.7)	53.1(53.0–53.3)	3.7(3.2–4.2)	13.7	13.6	0.81(76)	Quiescent
				2.5(1.8–4.3)	53.3(53.1–53.5)	...	26.1	22.4	...	Flare
A-4	23.7	26 07.36	25 31.4	19.4(>0.2)	51.4(51.0–59.7)	4.6(1.9–44.5)	0.8	0.4	0.34(7)	
A-5	994.2	26 07.62	27 41.6	2.1(1.8–2.4)	53.1(53.0–53.2)	2.8(2.5–3.1)	13.4	11.7	0.72(114)	Quiescent
				3.5(2.5–4.9)	53.2(53.1–53.4)	...	34.5	20.8	...	Flare1
				2.6(1.9–4.0)	53.2(53.0–53.3)	...	22.0	16.0	...	Flare2
A-6	193.1	26 10.34	20 54.6	2.3(1.4–4.3)	53.0(52.6–53.4)	5.8(4.2–8.5)	8.2	9.5	0.74(17)	
A-7	83.1	26 12.42	28 49.0	3.3(1.4–10.3)	52.1(51.8–52.8)	5.5(3.5–10.2)	2.0	1.6	0.57(24)	
A-8	16.2	26 13.30	28 23.0	2.0(>0.2)	51.4(50.6–56.1)	3.0(0.8–10.2)	0.3	0.3	0.95(2)	
A-9[#]	12.9	26 14.34	22 28.1	1.0(fixed)	53.0(51.4–54.1)	26.6(3.4–92.8)	0.2	8.9	0.57(2)	
				5.0(fixed)	51.4(50.4–51.9)	10.8(0.8–46.5)	0.4	0.3	0.39(2)	
A-10[‡‡]	10.9	26 15.06	25 48.1	...	...	...	...	...	...	
A-11	59.8	26 15.71	27 49.3	3.7(>0.7)	52.0(51.6–54.2)	6.6(3.3–25.6)	1.5	1.3	0.56(14)	
A-12	180.3	26 15.81	19 22.2	1.2(1.1–1.6)	52.6(52.3–52.9)	2.6(2.0–3.0)	1.8	3.1	0.73(15)	Quiescent
				4.3(>0.9)	52.8(52.4–53.3)	...	15.1	8.1	...	Flare
A-13	16.2	26 16.32	18 43.0	5.2(>0.5)	51.4(50.9–55.4)	5.8(1.6–43.6)	0.5	0.3	0.01(1)	
A-14	2068.5	26 16.87	22 23.0	1.7(1.5–1.9)	53.3(53.2–53.3)	1.9(1.8–2.1)	18.6	16.3	1.14(165)	Quiescent
				2.6(2.2–3.1)	53.5(53.4–53.6)	...	54.0	33.4	...	Flare
A-15	3741.7	26 17.06	20 21.6	1.3(1.2–1.3)	53.1(53.1–53.1)	0.5(0.5–0.6)	19.0	10.7	1.29(181)	Quiescent
				1.4(1.3–1.5)	53.1(53.1–53.2)	...	22.5	12.1	...	Flare1
				1.5(1.3–1.7)	53.4(53.3–53.4)	...	41.4	20.7	...	Flare2
				1.5(1.4–1.6)	53.2(53.2–53.3)	...	28.4	14.3	...	Flare3
A-16	126.2	26 17.13	12 38.9	0.9(0.6–1.2)	52.4(52.2–52.8)	1.8(1.4–2.2)	1.1	2.5	1.26(16)	
A-17	38.3	26 17.47	18 08.8	1.8(0.6–21.8)	52.4(51.4–55.0)	11.1(3.0–37.3)	0.9	2.3	0.71(6)	
A-18	54.2	26 18.01	15 17.6	2.7(>0.6)	51.9(51.3–53.8)	5.0(1.6–14.4)	1.0	1.0	1.06(13)	
A-19	405.8	26 18.88	28 19.9	2.2(1.7–2.9)	52.6(52.4–52.7)	1.9(1.6–2.2)	5.3	3.6	1.07(37)	
A-20	3435.0	26 22.41	22 52.8	2.0(1.8–2.2)	53.7(53.7–53.8)	3.6(3.5–3.9)	49.2	51.5	0.95(178)	Quiescent
				2.4(2.1–2.8)	53.7(53.7–53.8)	...	65.2	56.2	...	Flare1
				2.2(1.7–3.0)	53.8(53.6–53.9)	...	60.3	57.4	...	Flare2
				2.4(2.0–2.8)	53.8(53.7–53.9)	...	72.7	63.9	...	Flare3
A-21[#]	11.2	26 23.22	26 36.8	1.0(fixed)	53.6(52.2–54.6)	52.1(9.7–130.8)	0.4	37.9	0.48(2)	
				5.0(fixed)	51.7(50.8–52.3)	23.3(2.7–71.4)	0.5	0.7	0.33(2)	
A-22	986.4	26 23.37	20 59.8	2.6(2.1–3.2)	52.6(52.6–52.7)	1.0(0.9–1.1)	9.4	4.7	1.13(51)	Quiescent
				2.8(2.1–4.1)	52.9(52.8–53.0)	...	19.4	9.3	...	Flare
A-23[§§]	478.9	26 23.61	24 39.6	4.1(2.5–8.6)	52.8(52.5–53.1)	11.6(9.4–14.7)	11.5	10.8	1.71(50)	Quiescent

Table 5.2 (Continued)

No.	Counts*	R.A.† (J2000)	Decl.† (J2000)	$< kT >$‡ (keV)	$\log(< EM >)$‡ (cm^{-3})	N_{H}‡ (10^{22} cm^{-2})	Flux§	L_X§	Red-χ^2‖	Comment
				12.1(>5.4)	53.3(51.4–53.6)	...	87.8	52.4	...	Flare1
				4.2(>1.8)	53.2(51.4–53.7)	...	18.7	19.8	...	Flare2
A-24§§	2604.9	26 24.07	24 48.1	2.2(2.0–2.6)	53.4(53.3–53.5)	4.2(3.9–4.5)	29.2	29.2	1.25(114)	Quiescent
				5.7(4.5–7.7)	53.9(53.8–54.0)	...	253.4	139.3	...	Flare
A-25	2036.4	26 24.08	16 13.1	3.3(2.8–3.9)	53.1(53.0–53.1)	1.4(1.3–1.5)	27.1	13.5	0.99(116)	Quiescent
				12.7(>4.6)	53.1(53.0–53.2)	...	60.6	22.6	...	Flare1
				3.3(2.6–4.4)	53.1(53.1–53.2)	...	32.7	16.3	...	Flare2
				7.9(5.1–19.2)	53.2(53.2–53.3)	...	67.1	26.5	...	Flare3
A-26	380.8	26 25.26	23 23.8	2.2(1.6–3.4)	52.8(52.5–53.1)	6.0(5.0–7.4)	4.9	6.0	0.66(64)	Quiescent
				2.7(1.7–5.3)	53.5(53.2–53.8)	...	32.7	33.3	...	Flare1
				3.4(>1.6)	53.0(52.7–53.4)	...	15.1	12.7	...	Flare2
				1.9(1.3–3.0)	53.0(52.8–53.3)	...	6.8	10.3	...	Flare3
A-27	22.3	26 25.31	24 44.9	1.1(0.3–6.8)	51.7(50.8–55.0)	2.5(0.5–11.1)	0.2	0.5	1.03(2)	
A-28	88.4	26 25.72	14 27.1	1.4(1.0–4.0)	51.1(50.9–51.3)	0.4(0.1–0.7)	0.2	0.1	1.29(32)	Quiescent
				1.7(1.2–4.1)	51.8(51.6–51.9)	...	1.4	0.6	...	Flare
A-29‖‖	25.0	26 27.47	24 17.8			– see Table 6.6 –				
A-30‡‡	10.2	26 27.83	26 41.8	...	...	...	...	...	...	
A-31‖‖	12.2	26 27.89	23 59.2			– see Table 6.6 –				
A-32	28.5	26 28.43	15 40.9	2.4(>0.7)	51.4(50.8–52.4)	1.5(0.2–4.2)	0.4	0.2	0.70(14)	
A-33	336.3	26 29.69	19 05.3	1.8(1.5–2.3)	52.7(52.6–52.9)	3.2(2.7–3.9)	4.8	5.1	0.78(29)	
A-34	396.5	26 30.55	22 56.8	2.1(1.6–2.7)	52.7(52.5–52.9)	3.6(3.0–4.4)	4.9	4.8	0.75(69)	Quiescent
				3.3(2.1–6.9)	53.0(52.8–53.2)	...	16.4	11.4	...	Flare
A-35#	26.8	26 30.62	20 23.4	1.0(fixed)	52.8(52.4–53.4)	14.4(8.9–32.5)	0.4	6.1	1.50(3)	
				5.0(fixed)	51.5(51.2–51.8)	6.9(3.8–16.1)	0.6	0.5	0.77(3)	
A-36	14.8	26 31.04	31 04.0	1.5(>0.2)	51.5(50.5–55.5)	3.1(0.5–13.2)	0.2	0.3	0.19(3)	
A-37#	15.2	26 31.32	18 33.0	1.0(fixed)	52.2(49.8–53.1)	8.0(>35.2)	0.2	1.3	1.12(2)	
				5.0(fixed)	51.0(49.8–51.3)	3.1(>13.3)	0.2	0.1	0.95(2)	
A-38	36.6	26 31.39	25 30.3	4.2(>1.4)	51.2(50.8–51.7)	1.1(0.4–2.7)	0.5	0.2	0.95(4)	
A-39#	21.6	26 31.55	23 18.1	1.0(fixed)	52.7(52.2–53.0)	12.3(7.6–21.6)	0.3	4.2	1.74(2)	
				5.0(fixed)	51.4(51.0–51.7)	5.8(2.9–13.1)	0.5	0.4	1.39(2)	
A-40#	13.8	26 33.26	19 51.2	1.0(fixed)	52.6(51.9–53.5)	12.7(5.8–46.7)	0.2	3.3	1.01(1)	
				5.0(fixed)	51.2(50.8–51.6)	5.3(2.0–18.7)	0.4	0.2	0.03(1)	
A-41##	2249.6	26 34.20	23 28.2			– see Table 6.4 –				
A-42#	39.6	26 34.51	22 29.0	1.0(fixed)	53.6(53.1–53.9)	29.6(18.4–43.3)	0.7	32.1	1.60(6)	
				5.0(fixed)	51.6(51.4–51.8)	4.7(3.0–10.3)	0.8	0.5	0.88(6)	
A-43#	14.9	26 36.77	19 33.4	1.0(fixed)	52.8(48.2–53.5)	16.4(8.3–41.2)	0.3	5.7	0.13(1)	
				5.0(fixed)	51.4(51.0–52.0)	8.0(3.2–25.4)	0.5	0.4	0.02(1)	
A-44	105.7	26 36.81	15 51.4	2.3(1.3–3.8)	52.3(51.9–52.9)	5.4(3.4–8.7)	2.0	2.2	0.98(19)	
A-45#	8.4	26 36.85	19 00.6	1.0(fixed)	51.5(50.6–52.4)	3.3(0.9–14.2)	0.1	0.3	0.52(1)	
				5.0(fixed)	50.7(50.0–51.0)	1.3(0.1–5.2)	0.2	0.1	0.07(1)	
A-46	63.6	26 37.16	15 59.8	0.8(0.6–1.2)	51.8(51.3–52.2)	1.0(0.8–1.4)	0.4	0.6	0.22(11)	
A-47‡‡	12.2	26 37.90	19 42.9	...	...	...	...	...	...	
A-48#	14.2(m)	26 38.90	23 28.1	1.0(fixed)	52.2(49.7–55.1)	10.5(<218.8)	0.1	1.6	1.82(2)	
				5.0(fixed)	50.4(49.8–52.1)	0.8(<73.9)	0.1	0.1	1.12(2)	

Table 5.2 (Continued)

No.	Counts*	R.A.† (J2000)	Decl.† (J2000)	$< kT >$‡ (keV)	log($< EM >$)‡ (cm^{-3})	N_H‡ (10^{22} cm^{-2})	Flux§	L_X§	Red-χ^2‖	Comment
A-49	186.0	26 40.50	27 14.4	2.3(1.4–3.6)	52.4(52.0–52.9)	5.5(3.8–8.2)	2.1	2.3	0.53(32)	Quiescent
				4.2(2.4–15.2)	52.9(52.7–53.3)	...	15.8	11.3	...	Flare
A-50	19.0	26 41.81	16 05.2	4.0(>0.5)	51.3(50.6–54.4)	3.9(0.7–14.3)	0.4	0.3	0.66(3)	
A-51	51.2	26 42.44	26 25.4	1.2(0.6–2.3)	52.6(51.9–53.6)	6.3(4.0–10.1)	0.8	3.1	0.43(8)	
A-52	123.9	26 42.57	26 31.7	2.6(1.5–5.9)	52.4(52.0–52.8)	5.7(4.0–8.2)	2.4	2.4	1.00(21)	
A-53	1211.3	26 42.89	20 29.9	2.1(1.8–2.4)	53.0(53.0–53.1)	1.9(1.6–2.0)	14.9	10.7	1.13(70)	Quiescent
				2.6(1.9–4.2)	53.1(53.0–53.3)	...	24.7	15.1	...	Flare
A-54‡‡	11.2	26 42.93	22 59.2	...	...	...	...	...	...	
A-55	20.8	26 43.38	24 34.7	9.6(>0.2)	51.4(51.0–58.1)	7.6(2.9–32.8)	0.7	0.4	1.68(1)	
A-56	608.5	26 43.80	16 32.8	1.9(1.5–2.4)	52.7(52.6–52.9)	1.6(1.3–2.0)	6.6	4.7	1.47(52)	
A-57‡‡	11.6	26 43.91	27 17.1	...	...	...	...	...	...	
A-58‡‡	5.9	26 44.77	22 57.0	...	...	...	...	...	...	
A-59	73.9	26 45.07	23 07.8	6.7(>1.3)	51.7(51.5–52.4)	3.1(1.7–7.1)	1.6	0.8	0.86(11)	
A-60	81.7	26 46.79	19 07.9	1.9(1.1–3.4)	51.8(51.4–52.2)	1.6(1.2–2.7)	0.8	0.6	1.05(15)	
A-61	55.9	26 48.46	28 38.3	1.2(1.0–1.8)	52.6(52.4–52.9)	7.5(5.6–9.4)	0.8	3.3	0.84(24)	= BF-2
A-62#	19.5	26 49.18	21 43.4	5.0(fixed)	51.1(50.7–51.3)	2.4(1.1–5.7)	0.3	0.2	1.38(3)	
A-63	1372.5	26 49.27	20 02.8	1.7(1.5–1.9)	53.1(53.0–53.2)	2.1(1.9–2.3)	11.7	10.9	0.94(115)	Quiescent
				2.2(1.9–2.4)	53.2(53.1–53.3)	...	22.0	16.1	...	Flare
A-64	7.7(m)	26 51.94	30 39.9	2.8(>0.0)	51.1(<55.7)	5.9(4.0–10.9)	0.1	0.1	0.53(12)	= BF-4
A-65***	27.6	26 52.51	31 33.9	1.8(>0.5)	52.7(52.4–54.1)	30.6(15.1–68.5)	0.8	4.8	1.06(18)	= BF-5
A-66	33.6	26 53.38	32 36.2	0.9(0.2–3.0)	53.0(51.7–58.0)	9.9(4.4–34.2)	0.5	8.3	0.87(13)	
A-67#	15.5	26 54.12	23 25.6	5.0(fixed)	51.0(50.4–51.5)	3.1(0.8–25.6)	0.2	0.1	1.36(2)	
A-68	25.1	26 54.12	28 40.2	3.4(>0.2)	51.8(51.0–60.4)	12.7(4.1–47.5)	0.6	0.8	0.95(9)	
A-69	461.7	26 54.48	26 20.5	1.8(1.5–2.2)	52.7(52.6–52.8)	2.5(2.2–2.8)	4.7	4.4	0.75(139)	= BF-7, Quiescent
				2.1(1.9–2.4)	52.9(52.7–53.0)	...	8.4	6.9	...	= BF-7, Flare
A-70	17.1	26 54.49	15 55.0	1.1(>0.1)	52.0(50.2–57.5)	5.6(0.0–65.7)	0.2	0.9	0.81(5)	
A-71	304.3	26 55.02	22 29.9	1.7(1.3–2.3)	52.7(52.5–53.0)	3.3(2.7–4.1)	4.1	4.9	1.13(25)	
A-72	48.8	26 58.42	21 29.9	2.0(0.8–10.5)	51.8(51.2–53.0)	3.4(1.5–7.9)	0.7	0.7	0.83(10)	
A-73	17.3	26 58.79	18 34.1	2.3(>0.4)	51.4(50.8–52.7)	2.1(0.7–4.3)	0.4	0.3	0.14(2)	
A-74‡‡	5.6(m)	26 58.87	22 15.6	...	...	...	...	...	0.85(2)	
A-75†††	200.8	27 00.07	26 40.3			– see Table 6.8 –				= BF-11
A-76	90.9	27 00.57	16 25.3	1.8(0.7–4.5)	51.4(51.0–51.9)	0.7(0.5–1.3)	0.4	0.2	0.92(17)	Quiescent
				2.4(0.6–15.5)	51.9(51.6–52.8)	...	1.8	0.8	...	Flare
A-77	55.7	27 03.04	26 14.0	2.1(>0.3)	52.4(51.5–53.6)	20.1(7.6–38.0)	0.7	2.2	1.17(19)	= BF-15, Quiescent
				2.0(>0.6)	53.8(52.9–54.9)	...	19.1	63.7	...	= BF-15, Flare
A-78	40.2	27 04.11	28 29.0	12.1(>1.5)	51.3(51.1–52.1)	3.0(1.9–6.2)	0.8	0.3	1.22(26)	= BF-16, Quiescent
				6.3(>1.1)	52.4(52.0–53.3)	...	7.3	3.6	...	= BF-16, Flare
A-79	4959.9	27 04.63	27 15.4	2.7(2.4–3.1)	53.5(53.4–53.5)	3.9(3.7–4.1)	39.1	32.0	0.95(239)	= BF-17, Quiescent

Table 5.2 (Continued)

No.	Counts*	R.A.† (J2000)	Decl.† (J2000)	< kT >‡ (keV)	log(< EM >)‡ (cm^{-3})	N_H‡ (10^{22} cm^{-2})	Flux§	L_X§	Red-χ^2‖	Comment
				5.1(4.2–6.6)	54.1(54.0–54.1)	...	283.2	164.1	...	= BF-17, Flare1
				3.0(2.7–3.4)	54.1(54.1–54.2)	...	194.8	147.4	...	= BF-17, Flare2
A-80	231.3	27 05.23	20 07.1	2.5(1.7–4.0)	52.2(52.0–52.4)	1.6(1.2–2.2)	2.8	1.7	0.77(47)	
A-81	291.1	27 06.02	26 18.6	2.1(1.7–4.1)	52.5(52.2–52.7)	3.7(2.7–4.9)	2.9	2.9	0.95(70)	= BF-19, Quiescent
				4.6(2.3–19.2)	53.1(52.8–53.4)	...	26.7	15.7	...	= BF-19, Flare
A-82	1192.4	27 10.34	19 12.6	0.7(0.6–0.8)	53.4(53.3–53.4)	1.4(1.3–1.4)	7.1	22.1	1.17(85)	
A-83	55.5	27 13.72	18 16.3	1.0(0.5–1.8)	52.2(51.7–53.2)	2.6(1.7–3.9)	0.6	1.5	0.70(16)	
A-84	549.4	27 22.98	18 00.0	1.5(1.2–1.9)	53.2(53.1–53.4)	3.3(2.9–3.9)	10.9	15.2	0.77(50)	
A-S1‡‡	5.5	26 16.94	23 31.0	...	...	...	...	...	...	
A-S2#	8.5	26 21.55	26 01.0	1.0(fixed)	51.8(50.7–52.2)	3.7(0.7–6.6)	0.2	0.6	1.07(2)	
				5.0(fixed)	50.7(50.2–51.1)	0.6(<2.6)	0.2	0.1	0.78(2)	
A-S3‡‡	4.4	26 23.51	29 58.4	...	...	...	...	...	...	
A-S4‡‡	2.8	26 47.24	25 04.0	...	...	...	...	...	...	
A-S5‡‡	2.7(m)	26 58.20	24 26.7	...	...	...	...	...	...	
A-H1‡‡	16.4	26 05.71	27 54.8	2.9(>0.7)	51.5(50.9–53.2)	3.7(1.4–15.8)	0.5	0.4	0.54(6)	
A-H2	31.2(m)	26 06.52	23 53.0	...	...	...	...	...	...	Contamination from A-2
A-H3‡‡	2.7(m)	26 08.18	21 11.4	...	...	...	...	...	...	
A-H4‡‡	6.9(m)	26 37.17	17 36.4	...	...	...	...	...	...	
A-H5‡‡	8.3	26 48.72	23 27.4	...	...	...	...	...	...	
BF-1	132.3	26 44.19	34 48.2	3.2(1.6–9.4)	52.5(52.1–53.0)	8.3(5.7–12.6)	3.2	3.4	0.97(25)	
BF-2	45.9	26 48.46	28 38.3	1.3(0.6–1.9)	52.6(51.9–54.1)	... ###	0.9	3.1	...###	= A-61
BF-3	26.0	26 48.91	38 23.7	1.8(0.3–11.2)	51.3(50.8–53.4)	1.4(0.9–4.0)	0.3	0.2	0.44(5)	
BF-4	23.4	26 51.96	30 40.2	1.5(0.3–16.0)	52.0(51.1–54.2)	...###	0.4	0.9	...###	= A-64
BF-5***	26.7	26 52.56	31 29.7	1.8(>0.5)	52.6(51.5–54.4)	... ###	0.6	3.8	...###	= A-65
BF-6#	21.7	26 53.96	39 24.7	1.0(fixed)	53.3(52.9–53.7)	24.5(16.3–45.6)	0.5	17.3	1.25(6)	
				5.0(fixed)	51.8(51.5–52.1)	14.0(7.9–31.2)	0.9	0.9	1.19(6)	
BF-7	526.4	26 54.46	26 20.5	1.6(1.3–1.9)	52.9(52.8–53.1)	... ###	6.8	7.6	...###	= A-69
BF-8	34.3	26 57.34	35 38.7	1.8(0.6–39.5)	52.0(51.2–54.2)	6.9(3.1–14.3)	0.5	0.9	0.73(4)	Quiescent
				2.8(>0.4)	52.9(52.1–55.9)	...	8.1	8.7	...	Flare
BF-9	32.8	26 59.07	35 57.2	0.9(0.2–2.6)	51.8(51.1–54.1)	1.8(0.7–3.8)	0.2	0.5	0.51(5)	
BF-10§§	128.1	26 59.16	34 58.3	2.1(1.3–3.1)	52.8(52.3–53.4)	12.0(7.8–19.6)	2.8	5.1	1.16(20)	
BF-11†††	229.3	26 59.98	26 40.3			– see Table 6.8 –				= A-75
BF-12	14.1	27 02.32	37 26.7	1.3(>0.2)	51.4(50.2–55.5)	2.6(0.1–19.3)	0.1	0.2	0.13(1)	
BF-13‡‡	9.5	27 02.46	28 39.9	...	...	...	...	...	...	
BF-14‡‡	5.3(m)	27 02.83	31 51.5	...	...	...	...	...	...	
BF-15	12.6(m)	27 03.04	26 11.5	0.9(0.4–9.8)	53.1(51.2–55.6)	... ###	0.3	12.2	...###	= A-77
BF-16	81.6	27 04.10	28 28.9	2.4(1.2–6.2)	52.0(51.7–52.7)	... ###	1.3	1.0	...###	= A-78

Table 5.2 (Continued)

No.	Counts*	R.A.† (J2000)	Decl.† (J2000)	$< kT >$‡ (keV)	$\log(< EM >)$‡ (cm^{-3})	N_H‡ (10^{22} cm^{-2})	Flux§	L_X§	Red-χ^2‖	Comment
BF-17	106.5	27 04.59	27 14.3	1.3(1.1–1.9)	52.3(52.0–52.6)	... ###	0.9	1.7	...###	= A-79, Quiescent
				2.0(1.1–8.1)	53.3(52.9–53.6)	...	16.6	17.8	... ###	= A-79, Flare
BF-18#	30.6	27 05.44	41 14.4	1.0(fixed)	54.0(52.5–54.6)	56.7(9.0–102.3)	0.8	91.6	1.35(6)	
				5.0(fixed)	51.6(51.3–52.2)	8.6(3.4–36.4)	0.8	0.6	0.81(6)	
BF-19	38.8	27 05.95	26 17.7	1.2(0.6–3.3)	52.1(51.6–52.8)	... ###	0.6	1.2	...###	= A-81
BF-20	58.6	27 06.60	41 50.0	0.9(0.5–1.3)	52.0(51.6–53.0)	1.8(1.1–2.5)	0.4	0.9	0.88(12)	
BF-21	106.5	27 06.78	38 15.2	1.2(0.8–2.0)	52.8(52.2–53.5)	5.8(4.0–8.6)	1.6	5.1	0.69(18)	
BF-22#	16.6	27 07.66	41 04.1	1.0(fixed)	53.6(52.9–54.1)	40.1(21.4–70.9)	0.5	32.2	0.16(3)	
				5.0(fixed)	51.7(51.1–52.1)	17.0(4.5–37.0)	0.6	0.7	0.30(3)	
BF-23#	13.6	27 08.40	39 40.3	1.0(fixed)	53.4(52.1–53.9)	38.4(9.9–70.1)	0.3	21.2	0.90(4)	
				5.0(fixed)	51.4(50.6–51.9)	10.9(1.9–38.7)	0.4	0.3	1.06(4)	
BF-24	74.0	27 09.12	34 08.2	2.0(1.3–4.8)	51.8(51.4–52.3)	2.2(1.5–3.0)	0.8	0.7	0.94(11)	
BF-25	42.9	27 09.32	40 22.1	0.8(0.4–1.3)	52.9(52.1–54.2)	6.3(4.0–9.6)	0.6	8.2	1.55(10)	
BF-26	1141.2	27 09.44	37 19.0	3.8(2.9–5.2)	53.2(53.1–53.3)	8.2(7.4–8.8)	22.4	20.4	1.14(126)	Quiescent
				5.8(3.8–9.5)	53.5(53.4–53.7)	...	71.8	52.5	...	Flare
BF-27	122.8	27 11.17	40 46.9	3.1(1.5–22.7)	52.3(51.9–52.9)	6.6(4.4–9.8)	2.4	2.2	0.73(26)	Quiescent
#				5.0(fixed)	52.9(52.5–53.1)	...	14.7	10.4	...	Flare
BF-28	217.8	27 11.73	38 32.4	3.8(2.0–11.2)	52.4(52.1–52.8)	6.5(4.8–9.1)	3.7	3.0	0.64(37)	Quiescent
				2.3(1.2–4.5)	53.6(53.2–54.2)	...	32.7	40.9	...	Flare
BF-29#	12.6	27 12.60	40 52.5	1.0(fixed)	53.0(52.4–53.5)	24.1(13.1–43.5)	0.3	9.8	0.96(2)	
				5.0(fixed)	51.3(50.7–51.7)	9.7(3.2–28.3)	0.3	0.3	1.90(2)	
BF-30‡‡	4.5(m)	27 15.25	34 10.2	...	...	...	...	...	...	
BF-31	1400.5	27 15.46	26 39.5	2.5(2.1–3.0)	53.0(52.9–53.1)	3.9(3.6–4.3)	12.0	10.4	1.08(125)	Quiescent
				2.8(2.3–3.0)	54.0(53.9–54.1)	...	137.2	110.8	...	Flare
BF-32‡‡	4.5	27 15.46	41 21.4	...	...	...	...	...	...	
BF-33	29.3	27 15.51	30 54.0	9.5(>0.5)	51.5(51.2–53.9)	3.8(1.9–15.3)	1.0	0.5	0.35(3)	
BF-34#	33.3	27 15.55	33 01.8	1.0(fixed)	53.2(52.7–53.7)	19.4(11.0–32.6)	0.6	15.3	1.13(4)	
				5.0(fixed)	51.8(51.5–52.0)	7.8(4.6–15.2)	1.1	0.8	0.64(4)	
BF-35	1086.9	27 15.92	38 43.6	3.3(2.6–4.2)	53.1(53.0–53.2)	3.0(2.6–3.1)	24.9	16.0	0.86(94)	Quiescent
				5.9(4.1–8.0)	53.6(53.5–53.7)	...	124.2	62.6	...	Flare
BF-36‖‖	105.4	27 16.41	31 14.7			– see Table 6.6 –				
BF-37‡‡	9.1	27 16.98	36 21.2	...	...	...	...	...	...	
BF-38#	19.0	27 17.47	36 27.1	5.0(fixed)	52.2(51.3–52.8)	41.8(5.4–95.2)	1.1	2.4	1.66(2)	
BF-39	155.4	27 17.56	28 56.3	6.3(>2.6)	52.2(52.0–52.6)	6.2(4.0–9.3)	4.0	2.6	0.75(27)	
BF-40	1299.2	27 18.17	28 52.5	1.9(1.6–2.3)	53.6(53.5–53.8)	8.0(7.3–9.0)	23.7	41.5	1.00(89)	Quiescent
				3.4(2.5–5.6)	53.8(53.7–54.0)	...	87.2	84.2	...	Flare
BF-41‡‡	8.6	27 18.34	39 14.3	...	...	...	...	...	...	
BF-42	514.0	27 18.48	29 05.7	1.2(1.0–1.4)	53.1(52.9–53.3)	3.2(2.8–3.7)	5.2	11.1	0.97(52)	Quiescent

Table 5.2 (Continued)

No.	Counts*	R.A.† (J2000)	Decl.† (J2000)	$< kT >$‡ (keV)	$\log(< EM >)$‡ (cm^{-3})	N_{H}‡ (10^{22} cm^{-2})	Flux§	L_X§	Red-χ^2‖	Comment
				1.7(1.3–2.4)	53.1(53.0–53.3)	...	10.8	12.4	...	Flare
BF-43‡‡	4.5	27 18.99	33 44.3	...	...	...	...	...	...	
BF-44	677.1	27 19.21	28 43.8	1.6(1.4–1.8)	53.4(53.2–53.5)	5.2(4.6–5.8)	11.2	19.8	0.83(58)	
BF-45#	55.0	27 19.34	31 30.7	1.0(fixed)	53.8(53.4–54.3)	36.0(23.2–65.1)	1.0	57.0	1.72(9)	
				5.0(fixed)	52.1(51.8–52.3)	15.7(10.2–25.3)	1.5	1.6	1.21(9)	
BF-46‡‡‡	8664.4	27 19.53	41 40.7			– see Table 6.3 –				
BF-47‡‡	6.4	27 19.91	35 31.8	...	...	...	...	...	...	
BF-48#	13.8	27 20.01	30 13.6	1.0(fixed)	54.1(53.1–54.7)	74.0(31.1–129.1)	0.5	101.7	0.25(2)	
				5.0(fixed)	51.9(51.3–52.4)	30.2(10.6–74.0)	0.6	1.1	0.27(2)	
BF-49	144.7	27 21.44	41 43.1	1.1(0.8–1.5)	52.8(52.4–53.3)	4.7(3.5–6.5)	1.6	5.9	0.90(34)	
BF-50	121.0	27 21.82	29 53.4	3.9(1.9–11.1)	52.3(52.0–52.9)	8.8(6.0–13.4)	3.1	2.8	0.65(21)	
BF-51	56.7	27 21.98	29 39.7	1.2(0.5–7.7)	52.1(51.1–53.5)	3.6(1.5–7.4)	0.5	1.0	0.65(8)	Quiescent
				5.1(>1.0)	52.6(52.2–53.6)	...	10.4	5.9	...	Flare1
				2.6(>0.3)	52.6(52.0–53.8)	...	5.6	4.6	...	Flare2
BF-52#	11.8(m)	27 22.42	39 53.0	1.0(fixed)	49.9(<51.6)	0.0(<7.0)	0.03	0.008	0.95(4)	
				5.0(fixed)	50.0(<54.6)	0.0(<820.4)	0.06	0.02	1.02(4)	
BF-53‡‡	4.5	27 22.64	34 14.9	...	...	...	...	...	...	
BF-54‡‡	11.2	27 23.64	31 57.3	...	...	...	...	...	...	
BF-55#	54.2	27 24.23	29 29.5	2.4(>1.0)	52.1(51.6–52.9)	3.2(1.3–6.1)	1.6	1.3	0.59(8)	Quiescent
				5.0(fixed)	52.9(52.3–53.3)	...	20.9	11.4	...	Flare
BF-56#	20.7	27 24.38	41 49.4	1.0(fixed)	51.8(51.2–52.1)	3.0(1.8–4.8)	0.2	0.5	1.43(5)	
BF-57	55.4	27 24.63	29 35.1	2.2(>0.9)	52.3(51.7–53.2)	3.0(0.7–6.0)	2.5	2.1	0.88(8)	
BF-58‡‡	4.3	27 25.02	34 35.4	...	...	...	...	...	...	
BF-59	647.3	27 26.51	39 23.1	2.7(2.1–3.5)	52.7(52.6–52.9)	3.4(3.0–3.7)	7.1	5.5	0.85(79)	Quiescent
				6.4(3.9–14.7)	53.2(53.1–53.4)	...	50.8	26.2	...	Flare
BF-60§§§	12.7	27 26.62	25 53.7	0.1(0.04–0.9)	53.4(50.3–56.4)	0.9(0.5–1.8)	0.2	2.2	0.73(3)	
BF-61	3055.0	27 26.95	40 50.9	2.3(2.0–2.6)	53.5(53.4–53.6)	4.8(4.5–5.1)	30.3	31.9	0.94(132)	Quiescent
				4.2(3.6–5.1)	54.1(54.0–54.2)	...	248.5	167.0	...	Flare
BF-62	1103.9	27 27.09	32 17.6	2.1(1.8–2.6)	53.0(52.9–53.2)	4.5(4.0–5.1)	10.2	11.4	1.01(105)	Quiescent
				3.5(2.3–5.0)	53.0(52.8–53.2)	...	16.8	12.3	...	Flare1
				2.8(2.3–3.6)	53.7(53.5–53.8)	...	60.9	52.4	...	Flare2
BF-63	480.4	27 27.41	31 16.4	1.9(1.5–2.3)	52.4(52.3–52.5)	1.2(1.0–1.5)	3.7	2.4	0.79(72)	Quiescent
				3.4(2.0–7.6)	52.7(52.6–52.9)	...	13.2	6.2	...	Flare
BF-64	21904.0††	27 28.04	39 33.5	3.1(2.8–3.6)	53.5(53.4–53.6)	5.1(4.9–5.3)	45.8	37.8	1.18(424)	Quiescent
				7.2(5.5–10.4)	53.8(53.7–53.9)	...	173.9	98.7	...	Flare1
				9.9(8.5–11.8)	54.8(54.8–54.8)	...	1912.2	1008.0	...	Flare2
BF-65	26.2	27 28.46	29 42.2	2.6(>0.6)	51.9(51.1–54.1)	8.8(3.5–33.3)	0.6	0.8	0.41(5)	
BF-66	309.3	27 28.49	27 20.7	1.6(1.4–1.9)	52.7(52.5–52.8)	2.7(2.4–3.0)	3.5	4.1	0.84(59)	Quiescent
				1.4(0.6–6.5)	52.9(52.3–54.5)	...	5.2	7.4	...	Flare
BF-67	18.5	27 28.82	38 06.3	3.0(>0.1)	51.4(50.7–54.8)	4.8(1.1–60.9)	0.4	0.3	0.65(2)	

Table 5.2 (Continued)

No.	Counts*	R.A.† (J2000)	Decl.† (J2000)	$< kT >$‡ (keV)	$\log(< EM >)$‡ (cm^{-3})	N_H‡ (10^{22} cm^{-2})	Flux§	L_X§	Red-χ^2‖	Comment
BF-68#	25.1	27 29.42	39 16.0	5.0(fixed)	51.6(51.2–52.1)	10.5(4.2–38.0)	0.6	0.5	1.47(3)	
BF-69	95.1	27 29.99	33 36.7	3.2(1.6–10.1)	52.2(51.8–52.7)	6.1(4.0–9.6)	2.1	1.8	0.71(14)	
BF-70#	12.9	27 30.13	38 03.7	1.0(fixed)	52.7(51.3–53.8)	18.4(3.0–78.4)	0.2	4.2	0.73(2)	
				5.0(fixed)	51.0(50.5–51.6)	3.9(1.1–27.1)	0.3	0.2	0.19(2)	
BF-71	233.7	27 30.15	27 43.6	1.6(0.9–2.6)	52.6(52.2–53.2)	3.5(2.3–5.3)	2.6	3.6	1.47(46)	
BF-72	194.8	27 31.09	34 03.4	1.6(1.3–2.3)	52.0(51.8–52.4)	1.3(0.9–1.5)	1.2	1.0	1.11(31)	Quiescent
				1.2(>0.4)	52.6(52.3–53.9)	...	3.7	3.8	...	Flare
BF-73	74.7	27 31.33	31 10.1	3.1(>1.2)	52.1(51.6–53.0)	7.9(4.3–15.1)	1.5	1.6	1.14(13)	
BF-74#	9.8	27 32.12	29 43.3	1.0(fixed)	51.9(51.3–52.3)	5.1(2.6–9.6)	0.1	0.7	1.30(1)	
BF-75	357.5	27 32.72	33 24.3	1.9(1.4–2.8)	52.7(52.5–53.0)	3.8(3.2–4.8)	4.8	5.3	1.13(60)	
BF-76	189.2	27 32.89	32 35.0	1.7(1.2–2.5)	52.4(52.2–52.7)	3.1(2.4–4.1)	2.1	2.4	1.11(31)	
BF-77#	14.3	27 33.04	31 48.3	1.0(fixed)	52.8(51.8–54.8)	22.7(7.0–173.4)	0.2	2.0	1.95(1)	
				5.0(fixed)	51.4(50.7–52.3)	11.4(1.8–81.4)	0.4	0.2	0.81(1)	
BF-78	2853.7	27 33.15	41 15.4	2.1(1.9–2.3)	53.4(53.3–53.4)	1.9(1.8–2.0)	32.2	23.1	1.60(117)	Quiescent
				4.0(3.2–5.0)	53.6(53.5–53.7)	...	105.0	52.8	...	Flare
BF-79	96.4	27 35.29	38 33.7	0.7(0.6–0.8)	51.6(51.3–51.9)	0.6(0.3–0.8)	0.4	0.4	1.06(19)	
BF-80#	27.9	27 36.01	32 18.0	5.0(fixed)	51.5(50.8–51.8)	6.3(0.8–15.2)	0.6	0.4	1.21(5)	
BF-81#	11.1	27 36.08	34 30.6	1.0(fixed)	53.5(52.4–54.8)	40.8(13.1–113.5)	0.4	26.4	0.53(1)	
				5.0(fixed)	51.7(51.0–52.8)	18.5(5.2–78.6)	0.6	0.7	0.19(1)	
BF-82	26.4	27 37.26	42 37.4	1.6(0.6–5.1)	51.9(51.2–53.1)	3.7(1.9–8.1)	0.5	0.7	0.77(9)	
BF-83#	18.8	27 37.83	36 04.7	1.0(fixed)	52.7(51.9–53.2)	15.6(5.9–34.5)	0.3	4.8	0.71(3)	
				5.0(fixed)	51.2(50.7–51.6)	4.5(1.2–17.6)	0.4	0.2	0.50(3)	
BF-84	175.7	27 38.16	30 42.6	1.1(0.9–1.5)	52.3(52.1–52.4)	1.9(1.6–2.2)	1.1	1.7	0.92(31)	Quiescent
				1.2(0.8–1.8)	52.7(52.4–53.1)	...	3.0	4.2	...	Flare
BF-85	1162.0	27 38.35	36 58.4	1.7(1.5–1.9)	53.1(53.0–53.2)	1.9(1.7–2.1)	12.3	10.7	1.25(48)	
BF-86	264.6	27 38.67	38 39.2	1.6(0.9–2.0)	52.1(51.9–52.5)	0.8(0.6–1.5)	1.7	1.0	1.19(46)	
BF-87	764.1	27 38.98	40 20.5	3.2(2.3–4.4)	52.9(52.7–53.1)	8.8(7.5–10.6)	8.2	8.7	1.04(71)	Quiescent
				4.5(3.8–5.9)	54.0(53.8–54.2)	...	148.7	126.1	...	Flare
BF-88	6909.3	27 39.47	39 15.5	2.2(2.0–2.5)	53.6(53.5–53.6)	1.8(1.7–1.9)	54.7	36.5	1.18(290)	Quiescent
				3.2(2.9–3.7)	53.7(53.7–53.8)	...	119.8	64.8	...	Flare1
				2.9(2.6–3.1)	53.8(53.7–53.8)	...	111.1	64.1	...	Flare2
				2.2(1.9–2.7)	53.7(53.6–53.7)	...	66.9	44.7	...	Flare3
BF-89 #	908.5	27 39.88	43 15.3	1.8(1.6–2.1)	53.3(53.2–53.5)	5.4(4.9–6.1)	12.6	18.5	0.84(115)	Quiescent
				5.0(fixed)	53.6(53.6–53.7)	...	93.2	61.2	...	Flare1
				2.3(1.6–3.0)	53.5(53.3–53.7)	...	27.3	30.5	...	Flare2
				2.5(1.5–5.9)	53.8(53.5–54.1)	...	64.5	65.1	...	Flare3
BF-90	52.2	27 41.53	35 37.6	1.4(0.7–3.7)	51.9(51.4–52.8)	2.6(1.9–4.3)	0.5	0.7	1.18(9)	
BF-91	125.9	27 42.79	38 51.0	0.9(0.7–1.1)	52.6(52.0–53.0)	2.9(1.7–3.9)	0.9	3.3	1.41(21)	
BF-92‖‖‖‖	229.0	27 43.63	31 26.5	>5.8	52.3(52.3–52.4)	6.0(4.9–7.5)	6.5	3.6	1.03(22)	Quiescent
				>1.5	52.8(52.5–52.9)	...	17.9	10.0	...	Flare
BF-93#	15.9	27 45.51	38 08.9	5.0(fixed)	51.9(50.1–56.8)	29.1(<721.3)	0.6	0.8	0.66(10)	

Table 5.2 (Continued)

No.	Counts*	R.A.† (J2000)	Decl.† (J2000)	$< kT >$‡ (keV)	$\log(< EM >)$‡ (cm^{-3})	N_H‡ (10^{22} cm^{-2})	Flux§	L_X§	Red-χ^2‖	Comment
BF-94	29.8	27 49.16	39 06.9	2.7(>0.2)	51.9(51.2–60.5)	10.7(4.2–26.9)	0.6	0.9	1.57(7)	
BF-95	162.6	27 50.42	31 49.5	1.4(0.8–2.2)	53.1(52.5–54.4)	11.1(6.9–23.2)	2.8	11.4	1.23(39)	
BF-96‡ ‡ ‡	4289.3	27 52.01	40 50.0			– see Table 6.3 –				
BF-97#	36.4	27 54.71	37 14.8	1.0(fixed)	52.9(52.6–53.2)	12.8(8.8–19.9)	0.5	7.6	1.08(10)	
				5.0(fixed)	51.6(51.3–51.8)	6.6(4.1–12.1)	0.8	0.6	1.29(10)	
BF-98	24.8	27 55.34	28 39.3	0.9(0.2–2.2)	51.5(50.8–53.3)	1.2(0.3–2.5)	0.2	0.3	0.70(5)	
BF-S1‡‡	8.9	26 49.06	37 31.7	...	...	...	...	...	...	
BF-S2‡‡	8.4	26 51.24	32 42.4	...	...	...	...	...	...	
BF-S3‡‡	6.4	26 51.53	28 54.8	...	...	...	...	...	...	
BF-S4#	7.4	27 04.57	24 57.6	1.0(fixed)	50.0(<50.6)	0.0(<0.8)	0.04	0.01	1.86(1)	
BF-S5‡‡	6.4(m)	27 07.72	27 33.0	...	...	...	...	...	...	
BF-S6‡‡	4.4	27 17.57	29 22.8	...	...	...	...	...	...	
BF-S7‡‡	4.4	27 24.87	41 04.4	...	...	...	...	...	...	
BF-S8‡‡	2.9	27 32.88	34 47.4	...	...	...	...	...	...	
BF-H1#	9.8(m)	26 43.55	33 00.5	5.0(fixed)	52.4(51.3–53.2)	55.1(14.8–164.6)	1.1	3.4	1.15(4)	
BF-H2‡‡	9.3(m)	26 49.38	36 18.7	...	...	...	...	...	...	
BF-H3#	11.1	27 32.06	38 33.1	1.0(fixed)	52.3(51.0–53.2)	10.8(2.2–49.1)	0.1	1.6	1.08(1)	
				5.0(fixed)	50.9(50.8–57.5)	3.5(<857.9)	0.2	0.1	1.00(1)	
BF-H4#	6.6(m)	27 50.01	36 49.1	1.0(fixed)	51.5(49.6–54.5)	3.5(<139.8)	0.1	0.3	1.56(1)	
				5.0(fixed)	50.6(49.7–52.1)	1.4(<69.9)	0.1	0.1	1.08(1)	

(footnotes for Table 5.2)

*Background-subtracted X-ray counts in 0.5–2.0 keV, 2.0–9.0 keV, and 0.5–9.0 keV for soft-band, hard-band, and the other sources, respectively. (m) denotes sources with marginal detections (the confidence level < 99.9 %, see §5.2). Although the confidence levels of A-48 and A-H2 are significant enough, we regard them as marginal sources because of the larger source size (A-48) and severe contamination from A-2 (A-H2).

†Right ascension and declination for all sources are 16h and -24°.

‡Parentheses indicate the 90 % confidence limits.

§Observed flux (10^{-14} ergs s^{-1} cm^{-2}) and absorption-corrected X-ray luminosity (10^{29} ergs s^{-1}; "$< L_X >$" in the text) in 0.5–9.0 keV.

‖Reduced-χ^2 for the spectral fittings. Parentheses indicate the degrees of freedom.

#We determine spectral parameters with fixed temperatures of 1 keV and 5 keV (see text). For sources which only show the parameters for $kT = 1$ or 5 keV, no good fitting is obtained for the other temperature.

**We assume the same abundances as the "F2" phase in Table 6.3. The quiescent spectrum is not obtained because the decay phases of the two flares occupy all of the light curve.

††The pileup effect is not corrected.

‡‡No spectral fit is done due to the limited statistics.

§§Abundances are free parameters (§6.3.2, §6.3.3, and §6.3.7).

‖‖We make the flare spectra with a bit larger timescale in order to obtain as good statistics as possible. Errors of $< EM >$ for A-29 in the quiescent are not determined because of the limited statistics.

##The spectra show the possible absorption edge of neutral Ca or warm Ar. The non-thermal model also well reproduces the spectra (§6.3.5, see also Hamaguchi et al. 2002).

***We assume the same temperature because of the limited statistics.

†††These show non-thermal spectra (§6.6.3).

‡‡‡These show two temperature model with an unusual abundance pattern (§6.2).

§§§Foreground star. The distance is 60 pc (Festin, 1998).

‖‖‖The best-fit value of $< kT >$ is not determined (larger than 10 keV), hence we assume 10 keV temperature for the estimation of the other parameters.

###$N_{\rm H}$ and reduced-χ^2 are estimated by the simultaneous fittings with the identical sources in obs-A.

5.7.2 Identifications of the X-ray sources

Table 5.3:: Identifications of the X-ray sources

No.	Offset* ($''$)	Radio†	— X-ray —‡ PSPC	HRI	ASCA	IKT	Other names§	Class‖
A-1	...	...	...	...	...	...	...	...
A-2	0.33	R8, S7	13	A11	3	...	DoAr21, ROXs8, YLW26, GSS23, Elias14, SKS1-5, ISO10	III
A-3	0.40	...	...	...	...	...	ISO13	II
A-4	7.54(R)	R9?	...	...	...	...	...	...
A-5	0.60	...	15?	A13	...	...	ISO14	III
A-6	0.23	...	16	...	...	...	GSS26, CRBR5, SKS1-6, ISO17	II
A-7	...	...	...	...	...	...	...	...
A-8	...	...	...	...	...	...	...	...
A-9	...	...	...	...	...	...	...	...
A-10	...	...	...	...	...	...	...	...
A-11	...	...	...	...	...	...	...	...
A-12	0.47	...	...	...	...	...	CRBR9, SKS1-7, ISO18	III $_c$
A-13	...	...	...	...	...	...	...	...
A-14	0.11	Lp1	18	A14	...	...	ROXs11, GSS29, Elias18, CRBR10, SKS1-8, ISO19	II
A-15	0.44	...	17	A15	...	...	DoAr24, ROXs10A, GSS28, Elias19, CRBR11, SKS1-9, ISO20	II
A-16	1.08	...	...	...	...	...	2MASSI J1626172−241238	?
A-17	...	...	...	...	...	...	...	...
A-18	...	...	...	...	...	...	...	...
A-19	0.38	...	19	...	...	...	YLW31, VSSG1, Elias20, ISO24	II
A-20	0.03	L2	...	A17	...	...	GY12, VSSG12, ISO34	III
A-21	...	...	...	...	...	...	...	...
A-22	0.19	...	24(22?)	A18	4	...	ROXs10B, GY20, GSS31, Elias22, CRBR29, SKS1-15, ISO36	II
A-23	0.23	L3	...	...	...	...	GY21, CRBR30, SKS1-16, ISO37	II
A-24	0.14	...	25	A19	C3	...	S2, GY23, GSS32, Elias23, CRBR32, SKS1-17, ISO39	II
A-25	0.15	...	26	A20	...	...	YLW32, Elias24, ISO40	II
A-26	0.09	...	...	...	...	...	GY31, CRBR34, SKS3-15	? ‖‖
A-27	0.12	...	...	...	...	...	GY29, CRBR35, SKS1-18, ISO41	II
A-28	0.55	...	...	...	...	...	2MASSI J1626257−241427	?
A-29	...	...	...	...	...	...	...	...
A-30	0.05	...	C15	...	...	...	GY37, VSSG29, CRBR37, ISO42	BD $_c$(III$_c$)
A-31	2.66(R)	L6?	...	...	...	...	...	...
A-32	0.92	...	...	...	...	...	ISO44	III $_c$
A-33	0.06	L8	27	...	...	...	SKS1-19, ISO45	III
A-34	0.72	L9	...	...	...	...	GY51, VSSG27, CRBR38, SKS1-20, ISO46	II
A-35	...	...	...	...	...	...	...	...
A-36	1.14	...	...	...	...	...	YLW35, GY54, IRS14, ISO47	III $_c$
A-37	1.42(R)	L10	...	...	...	...	...	...
A-38	0.24	...	...	...	...	...	GY59, CRBR39, SKS1-21	BD $_c$
A-39	...	...	...	...	...	...	...	...
A-40	...	...	...	...	...	...	...	...

Table 5.3 (Continued)

No.	Offset* ($''$)	Radio†	—- X-ray —-‡ *PSPC*	*HRI*	*ASCA*	IKT	Other names§	Class‖
A-41	0.26	R15, S13, L11	28	A21	5	...	S1, ROXs14, YLW36, GY70, GSS35, Elias25, CRBR41, SKS1-22, ISO48	III
A-42	...	...	...	...	...	...	...	...
A-43	...	...	...	...	...	...	...	...
A-44	0.60	...	...	A22	...	...	ISO51	II
A-45	0.89	...	...	...	...	...	ISO50	III $_c$
A-46	0.07	...	...	...	...	...	2MASSI J1626371−241559	?
A-47	...	...	...	...	...	...	...	...
A-48	...	...	...	...	...	...	...	...
A-49	0.06	...	...	...	...	...	GY91, CRBR42, ISO54	I
A-50	...	...	...	...	...	...	...	...
A-51	0.53	R16, L15	...	...	...	...	GY101, CRBR43, ISO60	III
A-52	0.32	...	...	...	...	...	GY103, CRBR44, ISO61	III
A-53	0.23	...	29	A23	C4	...	GY110, VSSG2, GSS37, Elias26, ISO62	II
A-54	0.25	L16?	C19	...	...	...	GY109, ISO63	II
A-55	...	...	...	...	...	...	...	...
A-56	0.44	R17, S15	30	...	...	...	YLW39, VSSG11, IRS19, ISO64	III
A-57	...	...	...	...	...	...	...	...
A-58	...	...	...	...	...	...	...	...
A-59	0.31	Lp3	...	...	...	...	GY116, VSSG28, GSS39, Elias27, ISO67	II
A-60	0.32	...	...	...	...	...	2MASSI J1626467−241908	?
A-61	0.67	...	...	...	...	2	GY128, WL2, BBRCG6, ISO70	II
A-62	...	...	...	...	...	...	...	...
A-63	0.26	L18	32	A25	...	...	ROXs17, GY135, VSSG3, ISO73	III
A-64	0.52	...	C21?	...	...	4	GY144, BBRCG13, CRBR47, ISO75	II
A-65	...	...	...	...	...	5	...	...
A-66	1.51	...	...	...	...	...	GY146, BBRCG14, CRBR48, ISO76	II
A-67	...	...	...	...	...	...	...	...
A-68	...	...	...	...	...	...	...	...
A-69	0.33	...	33	...	...	7	GY153, VSSG5, ISO78	II
A-70	...	...	...	...	...	...	...	...
A-71	0.51	...	C22?	...	...	...	GY156, VSSG6, GSS40, ISO80	III
A-72	0.16	...	C23?	...	...	...	YLW1C, GY171, IRS26, ISO86	II
A-73	2.05	...	...	...	...	...	ISO87	II
A-74	...	...	...	...	...	...	...	...
A-75	1.95(R)	R19, S20, L21	...	...	...	11	...	...
A-76	0.20	...	...	...	...	...	2MASSI J1627005−241625	?
A-77	0.71	...	...	...	...	12	GY188, ISO93	II
A-78	0.93	...	...	...	...	13	YLW6, GY192, WL1, VSSG31, BBRCG20, CRBR55, IRS29, ISO95	II
A-79	0.54	...	C24?	...	...	14	GY195, ISO98	II
A-80	0.88	...	...	...	...	...	GY199, VSSG21	?
A-81	0.45	...	C25	...	...	16	YLW10A, GY203, IRS30, ISO101	III
A-82	0.73	...	38	A26	...	...	SR21, YLW8, VSSG23, Elias30, ISO110	II
A-83	0.57	...	...	...	...	...	VSSG24, ISO116	II
A-84	2.82	R21	42	...	...	...	ROXs23, VSSG22, ISO135	III
A-S1	...	...	...	...	...	...	...	...

Table 5.3 (Continued)

No.	Offset* ($''$)	Radio†	— X-ray —‡ PSPC	HRI	ASCA	IKT	Other names§	Class‖
A-S2	0.10	...	...	...	...	...	(GY5, CRBR21, SKS1-13, ISO30) ‡‡	BD_c(II)
A-S3	...	...	...	...	...	...	...	...
A-S4	...	...	...	...	...	...	...	...
A-S5	...	...	...	...	...	...	...	...
A-H1	...	...	...	...	...	...	...	...
A-H2	...	...	...	...	...	...	...	...
A-H3	...	...	...	...	...	...	...	...
A-H4	...	...	...	...	...	...	...	...
A-H5	...	...	...	...	...	...	...	...
BF-1	0.25	...	...	...	...	1	YLW2, GY111, WL12, VSSG30, BBRCG4, ISO65	I
BF-2	0.72	(= A-61)						
BF-3	1.74	...	...	...	...	3	GY129, WL18, BBRCG8, ISO72	II
BF-4	0.73	(= A-64)						
BF-5	...	(= A-65)						
BF-6	...	...	...	...	...	6	...	...
BF-7	0.05	(= A-69)						
BF-8	0.04	...	34	...	...	8	YLW4B, GY164, WL21, BBRCG17, CRBR50, SKS3-23, IRS23, ISO84	II
BF-9	0.21	...	...	...	...	9	YLW4A, GY172, WL14, BBRCG18, CRBR52, SKS3-25, ISO89	II
BF-10	0.64	L23	...	...	...	10	YLW4C, GY174, WL22, CRBR53, IRS27, ISO90	II
BF-11	0.97(R)	(= A-75)						
BF-12	0.71	...	...	...	...	...	YLW5, GY182, WL16, BBRCG19, CRBR54, SKS1-25, ISO92	II
BF-13	...	...	...	...	...	...	...	...
BF-14	...	...	...	...	...	...	...	...
BF-15	3.16	(= A-77)						
BF-16	1.11	(= A-78)						
BF-17	1.35	(= A-79)						
BF-18	...	...	...	...	...	15	...	...
BF-19	0.98	(= A-81)						
BF-20	1.17	...	...	...	...	17	GY204, SKS1-26, ISO102	II
BF-21	0.33	...	...	...	C5	18	GY205, WL17, BBRCG22, CRBR58, SKS3-27, ISO103	II
BF-22	1.79	...	...	...	...	19	2MASSI J1627075−244104	?
BF-23	...	...	...	...	...	20	...	...
BF-24	0.10	...	37	...	7	21	GY211, WL10, BBRCG24, CRBR59, SKS1-27, ISO105	II
BF-25	0.73	...	...	...	...	22	GY213, SKS3-28, ISO107	II
BF-26	0.27	L27	...	...	8	23	YLW7, GY214, WL15, Elias29, BBRCG23, CRBR60, SKS1-28, ISO108	I
BF-27	0.47	...	...	...	...	24	GY224, SKS3-30, ISO112	II
BF-28	0.45	...	...	...	...	25	YLW11A, GY227, WL19, BBRCG28, CRBR65, SKS3-31, ISO114	II
BF-29	...	...	...	...	...	...	...	...
BF-30	...	...	...	...	...	...	...	...

Table 5.3 (Continued)

No.	Offset* (″)	Radio†	— X-ray —‡ PSPC	HRI	ASCA	IKT	Other names§	Class‖
BF-31	0.29	...	...	...	...	26	YLW10B, GY239, SKS3-36, IRS34, ISO120	II
BF-32	...	...	...	...	...	...	...	...
BF-33	0.52	...	...	F15	...	27	GY238, BBRCG32, CRBR70, SKS3-35, IRS35, ISO119	II
BF-34	...	...	...	...	...	28	...	...
BF-35	0.28	L30	39	F16	...	29	YLW11B, GY240, WL20, BBRCG31, CRBR68, SKS1-31, ISO121	II
BF-36	...	...	...	...	...	30	...	...
BF-37	5.71(R)	L32?	...	...	...	31	...	...
BF-38	...	...	...	...	...	32	...	...
BF-39	0.23	...	...	...	...	33	YLW12A, GY244, VSSG26, BBRCG36, CRBR71, SKS1-32, IRS37, ISO124	II
BF-40	0.19	R20, S22	40	...	...	34	ROXs22, YLW12B, GY246, WL5, VSSG26, BBRCG37, CRBR73, SKS1-33, IRS38, ISO125	III
BF-41	0.77	...	...	...	...	35	GY245, BBRCG39, CRBR72, SKS3-37, ISO127	II
BF-42	0.24	...	...	...	C6	36	YLW12C, GY247, WL4, VSSG26, BBRCG40, CRBR75, SKS1-34, IRS39, ISO128	II
BF-43	...	...	...	...	...	37	...	...
BF-44	0.31	...	...	...	...	38	YLW12D, GY249, WL3, VSSG26, BBRCG41, CRBR77, SKS3-38, IRS41, ISO129	II
BF-45	...	...	...	...	...	39	...	...
BF-46	0.26	Lp6	41	F17	9A	40	SR12, ROXs21, YLW13A, GY250, CRBR76, SKS1-35, IRS40, ISO130	III
BF-47	...	...	...	...	...	41	...	...
BF-48	...	...	...	...	...	42	...	...
BF-49	0.49	...	...	...	...	43	YLW13B, GY252, CRBR79, SKS1-36, IRS42, ISO132	II
BF-50	0.19	...	...	...	10	44	YLW14, GY254, WL6, BBRCG38, CRBR80, SKS3-40, ISO134	I
BF-51	0.16	...	...	...	...	45	GY256, BBRCG43, CRBR81, SKS3-41	II
BF-52	...	...	...	...	...	...	...	...
BF-53	...	...	...	...	...	46	...	...
BF-54	...	...	...	...	...	47	...	...
BF-55	0.20	...	...	...	...	48	GY257, CRBR83, SKS3-43	?
BF-56	1.88	...	...	...	...	49	GY258, CRBR84, SKS3-42, ISO136	III $_c$
BF-57	0.38	...	...	...	...	50	GY259, CRBR86, SKS3-45	?
BF-58	...	...	...	...	...	51	...	...
BF-59	0.19	...	45?	...	...	53	YLW16C, GY262, BBRCG45, CRBR88, SKS3-47, ISO140	II
BF-60	0.73	...	...	...	...	52	GY264, SKS1-37	F
BF-61	0.25	R24, L33	43	F21	T††	54	YLW15A, GY265, CRBR89, SKS3-49, IRS43, ISO141	I
BF-62	0.20	...	...	...	...	55	GY266, SKS3-50	?

Table 5.3 (Continued)

No.	Offset[*] (″)	Radio[†]	— X-ray —[‡] *PSPC*	*HRI*	*ASCA*	IKT	Other names[§]	Class[‖]
BF-63	0.24	...	44	F22	...	56	GY267, WL13, VSSG25, Elias31, BBRCG42, SKS1-38, ISO142	II
BF-64	0.49	L35	45	G[**]	...	57	YLW16A, GY269, BBRCG49, SKS3-51, IRS44, ISO143	I
BF-65	...	...	...	...	...	58	...	...
BF-66	0.88	...	...	...	...	59	YLW17A, GY273, VSSG18, Elias32, SKS1-39, IRS45, ISO144	II
BF-67	...	...	...	...	...	...	...	...
BF-68	0.25	...	45	...	9B	60	YLW16B, GY274, BBRCG52, SKS3-54, IRS46, ISO145	I
BF-69	0.52	...	...	...	...	61	GY278, BBRCG53, ISO146	III $_c$
BF-70	...	...	...	...	...	62	...	...
BF-71	0.30	...	...	...	...	63	YLW17B, GY279, VSSG17, Elias33, SKS1-40, IRS47, ISO147	II
BF-72	0.51	...	47	...	...	64	GY283, BBRCG56, ISO148	III $_c$
BF-73	...	...	...	...	...	65	...	...
BF-74	0.54	...	...	...	...	...	GY287, SKS3-56	?
BF-75	0.69	Lp7	47?	...	...	66	GY289, BBRCG60, ISO152	III
BF-76	0.53	...	48	...	...	67	GY291, BBRCG61, ISO154	II
BF-77	...	...	...	...	...	68	...	...
BF-78	0.56	...	49	F27	...	69	GY292, CRBR90, ISO155	II
BF-79	0.42	...	...	...	...	70	GY295, SKS1-44, ISO156	III $_c$
BF-80	...	...	...	...	...	71	...	...
BF-81	...	...	...	...	...	...	...	...
BF-82	0.49	...	...	...	...	72	GY301, SKS3-59, ISO161	II
BF-83	...	...	...	...	...	73	...	...
BF-84	0.82	...	...	...	...	74	GY306, SKS1-47, IRS50	III
BF-85	0.65	...	50	F29	...	75	YLW47, GY308, SKS1-48, IRS49, ISO163	II
BF-86	0.58	...	...	...	...	76	GY310, SKS1-49, ISO164	BD(II)
BF-87	0.39	...	...	...	...	77	GY312, SKS3-61, ISO165	II
BF-88	0.50	Lp8	51	F30	...	78	ROXs27, GY314, SKS1-50, ISO166	II
BF-89	0.72	...	...	...	T[††]	79	YLW45, GY315, SKS3-63, IRS51, ISO167	I
BF-90	(0.62)[#]	...	...	...	...	80	GY322, ISO169	III $_c$
BF-91	1.41	...	...	...	...	81	GY326, SKS1-52, ISO172	II [‖‖]
BF-92	...	...	...	...	...	82	...	...
BF-93	...	...	...	...	...	...	...	...
BF-94	...	...	...	...	...	83	...	...
BF-95	...	...	...	...	...	84	...	...
BF-96	0.85	R32	54	F33	T[††]	85	ROXs31, GY380, IRS55, ISO184	III
BF-97	...	...	...	...	...	86	...	...
BF-98	1.44	...	...	...	...	87	GY397, ISO185	II
BF-S1	...	...	...	...	...	...	...	...
BF-S2	0.98	...	...	...	...	...	GY141, CRBR46	BD
BF-S3	...	...	...	...	...	...	...	...
BF-S4	...	...	...	...	...	...	...	...
BF-S5	...	...	...	...	...	...	...	...
BF-S6	...	...	...	...	...	...	...	...
BF-S7	...	...	...	...	...	...	...	...

Table 5.3 (Continued)

No.	Offset* ($''$)	Radio†	— X-ray —‡ *PSPC*	*HRI*	*ASCA*	IKT	Other names§	Class‖
BF-S8	...	...	...	...	...	...	...	...
BF-H1	...	...	...	...	...	...	...	...
BF-H2	...	...	...	...	...	...	...	...
BF-H3	...	...	...	...	...	...	A2§§	...
BF-H4	...	...	...	...	...	...	...	...

(footnotes for Table 5.3)

[*]Offset between the *Chandra* and nearest 2MASS sources. For sources having a radio counterpart only, the offset between the *Chandra* and radio sources (André et al., 1987; Leous et al., 1991) are shown, which is indicated by (R).

[†]Radio sources. S, R, and L indicate sources listed in André et al. (1987) (ROC), Stine et al. (1988) (SFAM), and Leous et al. (1991) (LFAM), respectively. Lp denotes possible radio sources in LFAM.

[‡]X-ray sources detected with *ROSAT*/PSPC (Casanova et al., 1995), *ROSAT*/HRI (Grosso et al., 2000), and *ASCA* (Kamata et al., 1997). "IKT" denotes *Chandra* sources already listed in Imanishi et al. (2001a).

[§]Source names used in the literature. Abbreviations for names are SR (Struve & Rudkjobing, 1949), DoAr (Dolidze & Arakelyan, 1959), ROXs (Bouvier & Appenzeller, 1992), S (Grasdalen et al., 1973), YLW (Young et al., 1986), GY (Greene & Young, 1992), WL (Wilking & Lada, 1983), VSSG (Vrba et al., 1975), GSS (Grasdalen et al., 1973), Elias (Elias, 1978), BBRCG (Barsony et al., 1989), CRBR (Comerón et al., 1993), SKS (Strom et al., 1995), IRS (Wilking et al., 1989), and ISO (Bontemps et al., 2001). For sources having NIR counterpart only in the 2MASS catalog, we alternatively show the 2MASS source names.

[‖]Source classifications; I: class I, II: class II, III: class III, III_c: class III candidate (Table 5 in Bontemps et al. 2001), BD: brown dwarf, BD_c: brown dwarf candidate (Imanishi et al., 2001b), F: foreground star (Festin, 1998). Unclassified NIR sources are indicated by "?", and sources with no NIR counterpart are called "unidentified sources", labeled no data point (...) in this column. For BD/BD_cs, we show the available IR classification in Bontemps et al. (2001) in the parentheses.

[#]Offset from a nearest NIR source in Greene & Young (1992).

[**]Grosso (2001).

[††]Tsuboi et al. (2000).

[‡‡]The position of GY5 (Greene & Young, 1992) is slightly shifted ($\sim 2''.3$) from the 2MASS source.

[§§]A candidate of HH object (Gómez et al., 1998, see also §6.6.6).

[‖‖]From NIR spectroscopy, Wilking et al. (1999) derived for these M dwarfs masses higher than the hydrogen burning limit.

5.7.3 Detected X-ray flares

Table 5.4:: Detected X-ray flares

No.	t_p (ks)	τ_r (ks)	τ_d (ks)	Q (cts ks^{-1})	Comment
— Class I —					
A-49	58	0.9*	12.2(9.2–16.0)	0.8(0.5–1.0)$^{\|}$	
BF-26	18	7.3(6.0–9.0)	5.5(4.4–6.7)	7.0(6.4–7.5)	
BF-61	82	2.9(2.6–3.2)	14.0(12.7–15.6)	10.7(10.0–11.3)	
BF-64	22	2.5(2.0–3.2)	14.6(13.2–16.1)	11.4(9.7–13.0)	Flare1
†	87.3(87.1–87.6)§	5.1*	27.7(24.3–31.5)	...	Flare2
BF-89	4	1.2(0.8–1.6)	3.4(2.9–4.1)	6.2(5.6–6.7)	Flare1
	88	4.0(2.4–6.2)	3.8(2.1–7.5)	...	Flare2
	...‡	2.3(1.5–3.4)	...‡	...	Flare3
— Class II —					
A-3	24	6.1(4.3–8.6)	3.7(1.8–9.3)	7.0(6.4–7.5)	
A-14	8	4.6(3.3–6.7)	12.8(10.6–15.7)	14.6(13.6–15.6)	
A-15	2	...‡	11.7(4.6–28.2)	28.1(22.4–30.8)	Flare1
	60	3.4(2.3–5.2)	4.1(3.0–5.8)	...	Flare2
	86	6.5(3.7–12.1)	15.1(8.1–48.0)	...	Flare3
A-22	20	4.2(2.8–6.1)	10.3(6.3–16.5)	7.5(6.7–8.2)	
A-23	56	0.8*	4.0(3.3–4.8)	2.0(1.7–2.3)	Flare1
	74	1.9(0.8–3.4)	3.8(2.1–6.3)	...	Flare2
A-24	72	2.9(2.7–3.1)	12.3(11.3–13.3)	6.4(5.9–7.0)	
A-25	10	0.9*	1.3*	17.0(15.9–18.0)	Flare1
	38	7.5(4.2–12.3)	3.0(0.7–10.1)	...	Flare2
	88	1.1(0.5–1.7)	5.6(3.8–9.1)	...	Flare3
A-34	36	3.0(1.5–5.8)	8.1(5.6–11.8)	2.4(2.0–2.8)	
A-53	82	2.2(1.2–3.6)	5.1(2.8–10.0)	10.6(10.0–11.3)	
A-69	70	26.9(11.0–121.3)	4.7*	3.0*	
A-77	98	3.5(2.2–5.5)	...‡	0.7(0.5–0.8)$^{\|}$	
A-78	94	1.5*	3.1*	1.0(0.8–1.1)	
A-79	42	2.8(2.5–3.0)	9.0(20.8–16.3)	2.4(1.7–3.1)	Flare1
	62	8.1(6.9–9.2)	17.3(35.9–33.4)	...	Flare2
BF-8	66	1.0*	1.3*	0.6(0.3–0.8)$^{\|}$	
BF-17	32	1.4(0.8–2.1)	1.7(0.8–2.9)	1.0(0.8–1.1)	
BF-27	86	1.5(0.6–2.5)	2.1(1.1–3.4)	0.9(0.7–1.1)	
BF-28	18	0.9(0.2–1.3)	2.7(1.9–4.0)	1.1(0.9–1.3)	
BF-31	54	2.5(2.3–2.7)	9.1(8.4–10.0)	1.1(0.8–1.3)	
BF-35	61	6.0(5.2–6.9)	15.8(13.7–18.2)	2.8(2.3–3.2)	
BF-42	76	7.5(3.8–15.1)	4.4(1.7–7.6)	3.8(3.4–4.2)	

Table 5.4 (Continued)

No.	t_p (ks)	τ_r (ks)	τ_d (ks)	Q (Cts ks^{-1})	Comment
BF-51	5	1.0*	1.0*	0.6(0.4–0.8)$^\|$	Flare1
	61	1.5*	1.3*	...	Flare2
BF-59	88	3.2(2.7–3.6)	7.6(6.2–9.5)	2.0(1.7–2.3)	
BF-63	54	...‡	6.9(5.3–8.9)	2.9(2.6–3.2)	
BF-66	98	3.0(1.2–5.8)	0.5*	2.4(2.1–2.7)	
BF-78	4	3.7(2.5–5.6)	7.9(6.8–9.2)	21.8(20.9–22.8)	
BF-87	84	3.4(3.1–3.8)	6.0(5.4–6.7)	1.0(0.8–1.2)	
BF-88	14	21.5(10.7–56.0)	7.0(3.6–15.6)	26.0(14.7–32.7)	Flare1
	46	31.1(17.9–52.5)	22.6(14.7–32.7)	...	Flare2
	84	4.2(1.9–20.2)	3.0(1.3–9.1)	...	Flare3
		— Class III —			
A-2†	...‡	...‡	131*	...‡	Flare1
	70	3.7(2.1-5.8)	55.6(30.8–117.5)	...	Flare2
A-5	54	2.8(1.8–4.1)	6.1(4.0–9.5)	8.0(7.2–8.7)	Flare1
	76	2.3*	7.0(2.6–22.9)	...	Flare2
A-20	22	17.0*	8.3(3.4–31.3)	27.3*	Flare1
	62	1.4*	2.7(2.7–2.7)	...	Flare2
	76	4.2*	9.9(5.6–20.8)	...	Flare3
A-41	90	2.0*	...‡	21.6(20.7–22.4)	
A-63	52	2.6(1.3–4.3)	66.4*	10.3(9.5–11.1)	
A-81	17	1.8(1.4–2.2)	5.3(4.2–6.7)	1.4(1.2–1.7)	
BF-40	88	1.8(1.2–2.7)	4.9(3.8–6.4)	9.7(9.1–10.2)	
BF-46	72	3.6(2.8–4.7)	10.8(8.1–14.2)	76.5(74.6–78.3)	
BF-84	72	5.5(2.7–12.3)	10.2(3.3–24.9)	1.0(0.7–1.2)	
BF-96	32	59.2(41.9–96.7)	13.8(10.8–17.9)	27.2(24.8–29.2)	
		— Class III$_c$ —			
A-12	20	0.9*	0.9*	1.3(1.1–1.5)	
BF-72	...‡	...‡	4.1(2.1–6.8)	1.2(1.0–1.4)	
		— Unclassified NIR sources —			
A-26	2	3.1(1.0–57.9)	4.0(3.1–5.1)	1.4(1.0–1.7)	Flare1
	18	1.3*	4.6(2.3–10.9)	...	Flare2
	76	...‡	20.1*	...	Flare3
A-28	50	8.5(4.3–17.8)	23.8(9.1–55.4)	0.8(0.3–1.1)	
A-76	72	1.9*	24.0(12.2–129.1)	1.0(0.8–1.2)	
BF-55	30	1.5*	0.8*	0.7(0.5–0.9)$^\|$	
BF-62	20	3.7(2.6–5.0)	6.9(4.9–9.9)	1.2(0.5–1.8)	Flare1
	53	5.7(5.0–6.5)	10.5(9.3–12.0)	...	Flare2
		— Unidentified sources —			
A-29	80	1.0*	2.1*	0.5$^{*\|}$	

Table 5.4 (Continued)

No.	t_p (ks)	τ_r (ks)	τ_d (ks)	Q (Cts ks^{-1})	Comment
BF-36	30	4.4(1.7–9.4)	...‡	0.8(0.6–0.9)	
BF-92	20	0.5*	2.6(1.1–4.4)	1.9*	

*We can not determine errors because of the limited statistics and/or strong coupling of the other parameters.

†Fitting is obtained for light curves in $2''\!.5$–$12''\!.5$ (A-2) and $2''\!.5$–$7''\!.5$ (BF-64) radius circles in order to avoid the pileup effect.

‡No fitting is possible because of the limited statistics and/or the boundary of the observations.

§We relax the flare peak time (t_p) to be free in order to obtain as good results as possible.

$^{\|}$This should be the upper limit because the fitting does not include the time bin with zero counts.

Chapter 6

Individual Sources

In this chapter, we show details of some interesting sources.

6.1 Protostars

6.1.1 A-49 – GY91

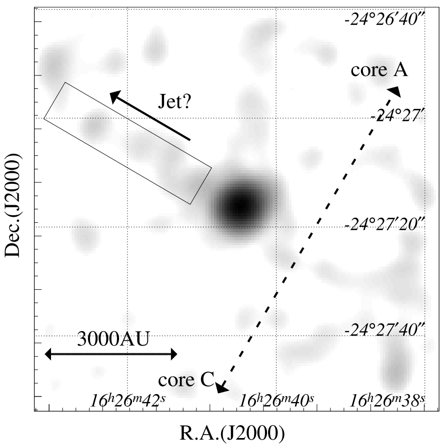

Fig. 6.1.— ACIS image around A-49 = GY91 in 0.5–9.0 keV, smoothed with a Gaussian of σ = 4 pixels. The solid rectangle represents the region for the X-ray data of jet-like emission (see text). Many cloud cores (not given in this figure) are aligned along the direction given by the dashed line (see Figure 3.1).

Figure 6.1 shows the ACIS image of a class I source GY91 (A-49). Besides significant X-rays from the central source, we can see weak diffuse jet-like emission to the north-east (the solid rectangle in Figure 6.1) perpendicular to the cloud core alignment; many cloud cores are aligned along the dashed line in Figure 6.1 (see also Figure 3.1). This X-ray "jet" is likely due to an outflow from GY91, although the significance level is still low ($\sim$2.3 σ). We make the spectrum from the rectangle region and fit it by the MEKAL model. Then we constrain the plasma temperature to be higher than $\sim$1 keV. This corresponds to the shock velocity of > 500 km s^{-1} (Favata et al., 2002), indicating surprisingly high jet activity. We note that such an extreme phenomenon has also been suggested by the *ASCA* detection of Doppler-shifted Fe lines from a class I in the R CrA cloud (Koyama et al., 1996). To confirm this jet-like X-rays with deeper exposure observations would be important to understand the outflow activity at the protostellar phase.

6.1.2 BF-26 – Elias29

A class I BF-26 = Elias29 exhibits an X-ray flare with a timescale of $\sim$10 ks (Figure A.1). $< kT >$ and $< L_X >$ during the flare are 5.8 keV and 5.3$\times$10^{30} ergs s^{-1}, while those in the quiescent phase are 3.8 keV and 2.0$\times$10^{30} ergs s^{-1}, respectively (Table 5.2). The *ASCA* satellite observed Elias29 twice with respective exposure times of 40 and 100 ks. In the first observation, it exhibited an X-ray flare similar to the present observation (Kamata et al., 1997). However, it became quiescent with $< L_X > = 3\times10^{30}$ ergs s^{-1} in the second observation (Tsuboi et al., 2000). It therefore infers that Elias29 shows the quiescent luminosity of $\sim$10^{30} ergs s^{-1} and exhibits frequent X-ray flares.

6.1.3 BF-50 – WL6

Kamata et al. (1997) claimed the detection of hard X-rays from a class I WL6 with *ASCA*, although nearby GY256, another class II source, may contaminate the X-rays from WL6. The *ASCA* light curve shows a sinusoidal shape of about 20 hour period. Since they found no temperature variation, which is typical of normal flares, they claimed that the modulation is due to stellar rotation. In the present observation, we clearly detect hard X-rays not only from WL6 (BF-50) but also from GY256 (BF-51). Two faint flares are found from GY256, with higher temperature than that in the quiescent phase (Table 5.2 and Figure A.1). However, we can see no sinusoidal light curve from WL6 nor from GY256.

6.1.4 BF-61 – YLW15A

ROSAT/HRI detected an extraordinary large X-ray flare from a class I YLW15A (Grosso et al., 1997). The inferred luminosity, however, depends largely on the assumed spectrum. We hence re-estimate the luminosity using our best-fit $< kT >$ (4.2 keV) and $N_{\rm H}$ (4.8$\times$10^{22} cm^{-2}) of YLW15A = BF-61 at a flare (Table 5.2). The HRI count rate at the flare peak of $\sim$17 cts ks^{-1} is then converted to the peak luminosity of $\sim$10^{33} ergs s^{-1}, which is about ten times brighter than that of the giant flare seen in YLW16A (see §6.1.5) but may not be extraordinary, comparable to the largest YSO flares detected with *ASCA* (V773 Tau: Tsuboi et al. 1998; ROXs31: Imanishi et al.

2002a, see also §6.2). The subsequent *ASCA* observation discovered quasi-periodic three X-ray flares with an interval of ∼20 hours (Tsuboi et al., 2000). Montmerle et al. (2000) interpreted these flares with a star-disk arcade conjecture in contrast to the X-ray emission from that of TTSs, which may have magnetic arcades at the stellar surface. Although *Chandra* confirms hard X-ray emission and finds a typical flare from YLW15A (Figure A.1), no multiple flares are found. Thus quasi-periodic flares are not always present but rather occasional phenomena.

Recently, VLA (Girart et al., 2000) and Subaru/COMICS (M. Honda, private communication) resolved YLW15A into a binary system with the separation angle of $\sim 0\farcs5$. The position of BF-64 favors that the origin of X-rays is the radio-faint and MIR-bright source VLA2 rather than VLA1.

6.1.5 BF-64 – YLW16A

The light curve of a class I BF-64 = YLW16A comprises two flares; the first is rather complex with spike-like structure and the second is a giant flare having an unusual profile (Figure 6.2 left). We examine spectral evolution by slicing the data in the time intervals as shown in Figure 6.2 (left). In the phases 7–9, we extract the spectra from the same region (a $2\farcs5$–$7\farcs5$ radius circle) as the light curve data, because these phases suffer the pileup effect (see §5.5). We first fit them by the MEKAL model allowing the abundance and $N_{\rm H}$ to be free for all the phases, then find no significant variation from phase to phase both in abundance ($\cong$ 0.3 solar) and $N_{\rm H}$ ($\cong 5.2\times10^{22}$ cm^{-2}). We hence fix the abundance to be 0.3 solar and fit them assuming that $N_{\rm H}$ is the same in all phases. Table 6.1 shows the resultant best-fit parameters for each time interval. As are seen in Figure 6.2 (left), the temperature (kT) and emission measure (EM) increase from phase 2 and reach their peak values at phase 3, then gradually decrease. The peak luminosity is estimated to be $\sim1\times10^{31}$ ergs s^{-1}. These phenomena of the first flare are similar to flares found in other YSOs. The second flare shows unusual time profiles in the flux and emission measure (EM). The temperature profile is, however, more typical of normal flares; at phase 7 it increases rapidly and stays almost constant or shows gradual decay. Such a property is similar to the giant flare of ROXs31 detected with *ASCA* (§6.2) and we interpret that it is due to a large loop length (§8.3).

Figure 6.2 (right) is the time-averaged spectrum during the large flare. A remarkable finding is an additional emission line near the 6.7 keV line of highly ionized (He-like) irons. The best-fit line center energy is 6.43±0.08 keV, which is attributable to neutral or low ionized irons. The most plausible origin is fluorescence from cold irons in the circumstellar matter. Assuming the spherical distribution of circumstellar gas around YLW16A, the equivalent width of iron (EW) is estimated to be

$$EW \approx 10 Z_{\rm Fe} (\frac{N_{\rm H}}{10^{22}\ {\rm cm}^{-2}})\ [{\rm eV}], \tag{6.1}$$

where $Z_{\rm Fe}$ and $N_{\rm H}$ are the abundance of iron and column density of the fluorescent medium, respectively (Inoue, 1985). If we regard that most of the observed column density (5.2×10^{22} cm^{-2}) originates from the circumstellar matter and use the iron abundance of 0.3 solar, we predict the maximum equivalent width to be ∼15 eV, which is significantly lower than the observed value of ∼200 eV. We therefore require non-spherical geometry; a larger amount of matter should be present out of the line-of-sight. A possible scenario is that YLW16A has a face-on geometry (Sekimoto et al., 1997) and the disk is responsible for the fluorescent 6.4 keV line. Since we see no time delay (reflection timescale) with $\gtrsim 10^4$ s between the flare on-set and 6.4 keV iron line appearance, the distance of the star and the reflecting region should be less than $\lesssim$ 20 AU, which is typical of the distance between the stellar surface and the inner edge of the disk (Feigelson & Montmerle, 1999).

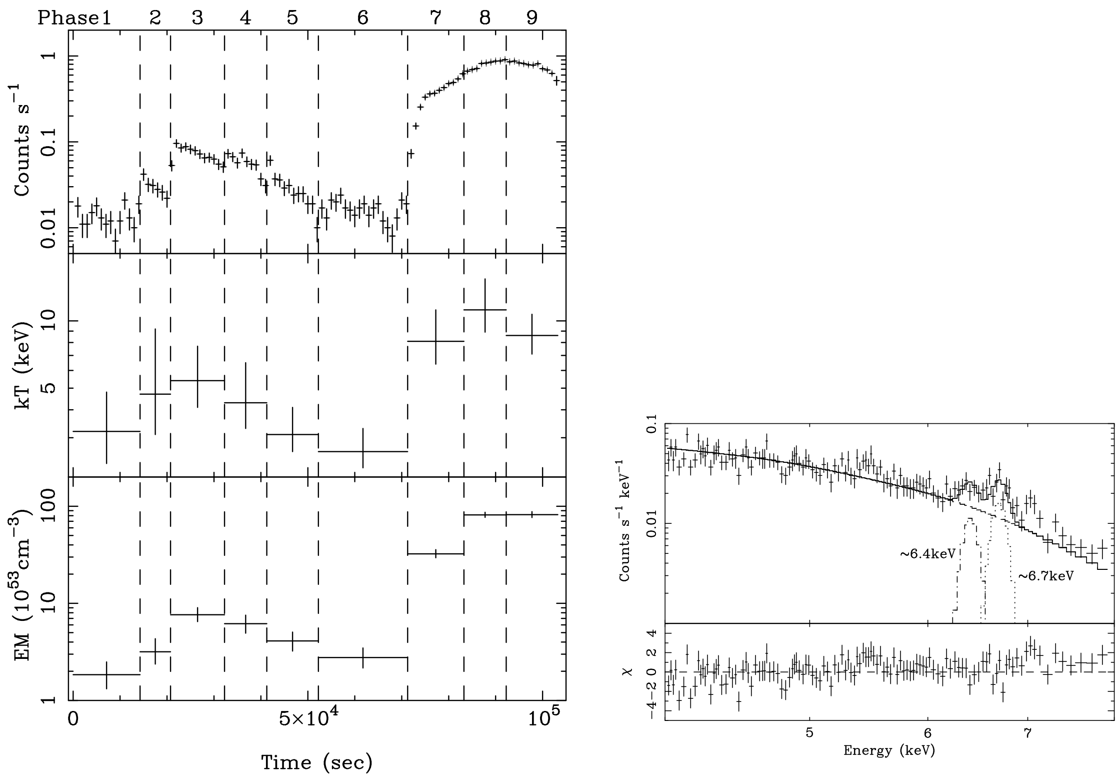

Fig. 6.2.— (left): (top) Light curve of BF-64 = YLW16A and (middle and bottom) time profile of the best-fit temperature and the emission measure. (right): Spectrum of YLW16A in phases 7–9. The upper panel shows data points (crosses) and the best-fit model (solid line), while the lower panel shows residuals from the best-fit model. Line structure exists at ∼6.4 keV and ∼6.7 keV.

Table 6.1: Best-fit parameters of BF64 = YLW16A

Phase*	kT (keV)	$\log(EM)$ (cm^{-3})	N_{H}† ($10^{22}\mathrm{cm}^{-2}$)	EW‡ (eV)	Flux§	L_X‖
1	3.2(2.3–4.8)	53.3(53.1–53.4)	5.2(5.0–5.4)	<217	0.3	0.2
2	4.7(3.1–9.2)	53.5(53.4–53.6)	5.2	<435	0.7	0.5
3	5.4(4.1–7.7)	53.9(53.8–54.0)	5.2	<59	1.8	1.1
4	4.3(3.3–6.5)	53.8(53.7–53.9)	5.2	<99	1.2	0.8
5	3.1(2.6–4.1)	53.6(53.5–53.7)	5.2	<97	0.6	0.5
6	2.6(2.2–3.3)	53.4(53.3–53.5)	5.2	<1466	0.3	0.3
7	8.1(6.4–11.2)	54.5(54.5–54.6)	5.2	181(78–284)	9.7	5.3
8	11.2(8.9–15.4)	54.9(54.9–54.9)	5.2	80(17–143)	26.7	13.8
9	8.6(7.1–10.7)	54.9(54.9–54.9)	5.2	<86	24.5	13.4

*See Figure 6.2.
†N_{H} is assumed to be the same value in all the phases.
‡Equivalent width for the 6.4 keV line.
§Observed flux (10^{-12} ergs s^{-1} cm^{-2}) in 0.5–9.0 keV.
‖Absorption-corrected luminosity (10^{31} ergs s^{-1}) in 0.5–9.0 keV.

6.1.6 VLA1623

Since there is no significant X-rays from a class 0 prototype VLA1623 (see also §6.5), we estimate its upper limit of $< L_X >$ assuming the MEKAL spectrum with the temperature of 1, 5, and 10 keV and with the abundance of 0.3 solar. From the radio data (André et al., 1993), the column density to VLA1623 is estimated to be $N_{\mathrm{H}} = (0.5\text{–}4)\times10^{23}$ cm^{-2}. We then calculate the upper limit of $< L_X >$ to be (0.78–78)$\times10^{29}$ ergs s^{-1}. Its uncertainty mainly comes from the difference of the assumed temperature (1, 5, and 10 keV). The upper limit is similar to that of faint class I sources in their quiescent phase (Figure 7.2a). The ratio of $< L_X >$ and radio intensity (388 μJy at 6 cm; Leous et al. 1991) is estimated to be <10^{13}–10^{15}, which is also comparable to that of other YSOs (§7.4.4). It may therefore be conceivable that VLA 1623 is an X-ray source but was in a quiescent phase during the *Chandra* observation. Further deep X-ray observations would be fruitful.

6.2 X-ray Brightest T Tauri Stars (DoAr21, ROXs21, and ROXs31)

Imanishi et al. (2002a) showed the *Chandra*/ACIS and *ASCA*/GIS results for a series of four long-term observations of DoAr21 (A-2), ROXs21 (BF-46) and ROXs31 (BF-96), the X-ray brightest TTSs in the ρ Ophiuchi cloud, then studied their long-term time variability and detailed structure of X-ray spectra. Here we show details.

6.2.1 Previous knowledge

The *Einstein* satellite first recognized these sources as bright X-ray sources (Montmerle et al., 1983). Subsequent optical observations revealed that they are K–M type stars having weak Hα emission (Bouvier & Appenzeller, 1992), which are classified as WTTSs (class III). Simon et al. (1995) observed them by using the lunar occultation in the infrared wavelengths and found that ROXs21 and ROXs31 are binary systems with separation angles of $0\farcs3$ and $0\farcs48$, respectively. Shevchenko & Herbst (1998) reported the rotation period of ROXs21 to be 1.39 days. Since they show no continuum emission at 1.3 mm (André & Montmerle, 1994), the circumstellar envelope would have already disappeared, while DoAr21 may still have an accretion disk as suggested by the detection of NIR polarized emission (Ageorges et al., 1997). Using the theoretical evolutionary tracks in the H-R diagram, the age of DoAr21 is estimated to be $\sim 10^5$ yr, which is younger than that of ROXs21 and ROXs31 ($\sim 10^6$ yr: Nürnberger et al., 1998). Finally, DoAr21 and ROXs31 show variable centimeter emission, which is probably due to gyro-synchrotron mechanism induced by surface magnetic field (Stine et al., 1988).

6.2.2 Long-term observations with *Chandra* and *ASCA*

We use the data of obs-BF for ROXs21 and ROXs31. Although DoAr21 suffers the pileup effect in obs-A, obs-BF detected X-rays from DoAr21 at the ACIS-S2 chip, which mitigates photon pileup because of the large off-axis angle (= large PSF size). We hence use the ACIS-S2 data for the following analysis. The background region for DoAr21 is taken from a source-free 19 arcmin^2 region on ACIS-S2, while that for ROXs21 and ROXs31 is the same as used in the previous analyses.

In order to examine long-term variability and spectral evolution of these sources, we additionally use the previous *ASCA* observations. Three observations (obs-A1, A2, and A3) were carried out with the two Gas Imaging Spectrometers (GISs: Ohashi et al., 1996) and the two Solid-state Imaging Spectrometers (SISs: Burke et al., 1991) onboard *ASCA*, which are at the foci of the X-ray telescopes (XRTs: Serlemitsos et al., 1995) sensitive to photons in 0.4–10 keV. However, they were outside of or at the edge of the SIS's field of view in the majority of the observations, hence we use the GIS data only. We retrieve the *ASCA* unscreened data from the HEASARC online service[1], then filtered out the data taken at a geomagnetic cutoff rigidity lower than 4 GV, at an elevation angle less than 5° from the Earth, and during passage through the South Atlantic Anomaly. Particle events were also removed using the rise-time discrimination method. The total available exposure times were ≈38 ks (obs-A1), 93 ks (A2), and 75 ks (A3) (Table 6.2).

Table 6.2: *ASCA*/GIS observation log

Obs.ID	Sequence ID	Observation Date (UT) Start	End	Exposure (ks)
A1 ...	20015010	1993 Aug 20 02:20	Aug 20 22:46	37.7
A2 ...	25020000	1997 Mar 2 07:32	Mar 4 21:21	93.1
A3 ...	96003000	1998 Aug 13 06:35	Aug 15 21:16	74.7

6.2.3 Time variability

Figures 6.3 and 6.4 show the X-ray light curves (no background subtraction) of (a) DoAr21, (b) ROXs21, and (c) ROXs31 obtained with *Chandra*/ACIS (obs-BF) and *ASCA*/GIS (obs-A1, A2, and A3), respectively. The vertical axis is photon counts normalized by the effective area at 1 keV for comparison with the different instruments and observation epochs. The time intervals of each data point are 10^3 s and 10^4 s for ACIS (Figure 6.3) and GIS (Figure 6.4), respectively. The energy bands of the ACIS and GIS data for DoAr21 are 0.5–9.0 keV, while the GIS light curves for ROXs21 and ROXs31 are limited in the soft energy band of 0.5–1.5 keV in order to avoid possible contamination from a nearby variable hard X-ray source YLW15A = BF-61 (Tsuboi, 1999; Tsuboi et al., 2000). To verify whether or not the contamination from YLW15A is significant in <1.5 keV, we check the amount of contamination from YLW15A and find that the best-fit absorption of $N_{\rm H}$ = 4.8×10^{22} cm^{-2} (Table 5.2) reduces the X-ray emission below 1.5 keV to less than 3 % of the 1.5–9 keV flux. Possible contamination from YLW15A to the GIS source circles of ROXs21 and ROXs31 is therefore insignificant in the 0.5–1.5 keV band. No data is shown in the light curve of ROXs21 (Figure 6.4b) from MJD = 50511.55–50512.20 due to significant contamination from an exceptionally giant flare of ROXs31 (see Figure 6.4c).

From Figures 6.3 and 6.4, we detect six, three, and two flares from DoAr21, ROXs21 and ROXs31, respectively. These are labeled as “F”, “F1”, “F2”, and “F3” with arrows in Figure 6.3 and 6.4, while the quiescent phases are indicated by “Q”. Among them, we find an extremely large

[1]http://legacy.gsfc.nasa.gov/cgi-bin/W3Browse/w3browse.pl.

flare from ROXs31 with the maximum flux of ∼100 times higher than the quiescent level (Figure 6.4c), which is separately treated in §6.2.7.

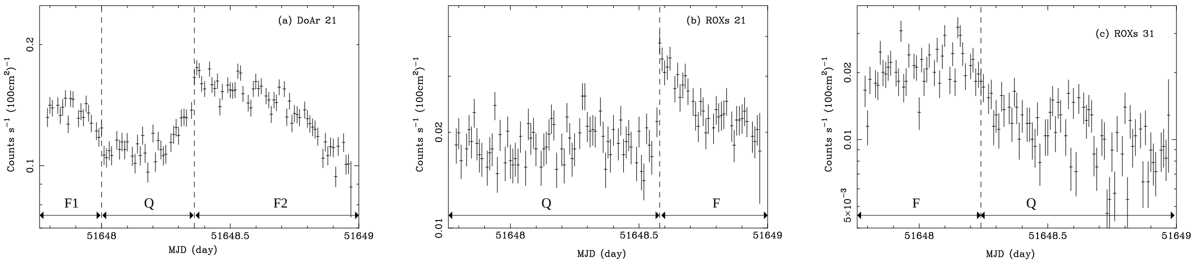

Fig. 6.3.— Light curves of (a) DoAr21, (b) ROXs21, and (c) ROXs31 in 0.5–9.0 keV obtained with *Chandra*/ACIS (obs-BF). The vertical axis is the X-ray count rate normalized by the effective area of 100 cm^2 at 1 keV. The lower arrows indicate the times of the flare and quiescent phases (see Table 6.3).

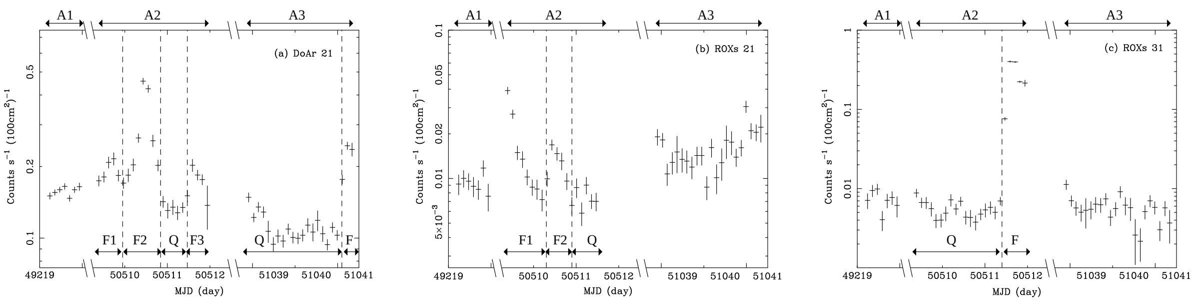

Fig. 6.4.— Light curves of (a) DoAr21 in 0.5–9.0 keV and of (b) ROXs21 and (c) ROXs 31 in 0.5–1.5 keV, obtained with *ASCA*/GIS (obs-A1, A2, and A3). The vertical axis is the X-ray count rate normalized by the effective area of 100 cm^2 at 1 keV. The lower arrows indicate the times of the flare and quiescent phases.

6.2.4 X-ray spectra

Figure 6.5 shows the background-subtracted ACIS spectra using all data of obs-BF. The spectra show several emission lines from highly ionized elements such as O, Ne, Na, Mg, Si, S, Ar, Ca, and Fe, which is characteristic of a thin thermal plasma. We hence fit them by the MEKAL model allowing the abundance of each element with prominent lines (indicated by arrows in Figure 6.5) to be free. For the study of time variation of the spectra, we separately fit the flare and quiescent spectra as shown in Figure 6.3. A single-temperature (1-T) model is not acceptable for all spectra except for DoAr21 and the flare phase of ROXs31. We hence fit them by a two-temperature (2-T) plasma model for ROXs21 and ROXs 31 and find acceptable fits. Table 6.3 shows the best-fit parameters. All elemental abundances are below the solar photospheric values (Anders & Grevesse, 1989) except for Ne in DoAr21 and Na in ROXs21. Figure 6.6 presents the best-fit abundances with the order of their first ionization potential (FIP).

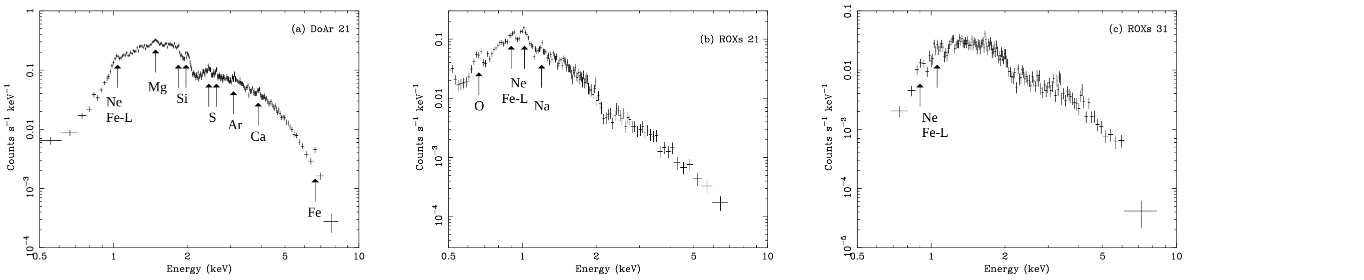

Fig. 6.5.— Time-averaged X-ray spectra of (a) DoAr21, (b) ROXs21, and (c) ROXs31. Arrows indicate prominent spectral features with the corresponding elements.

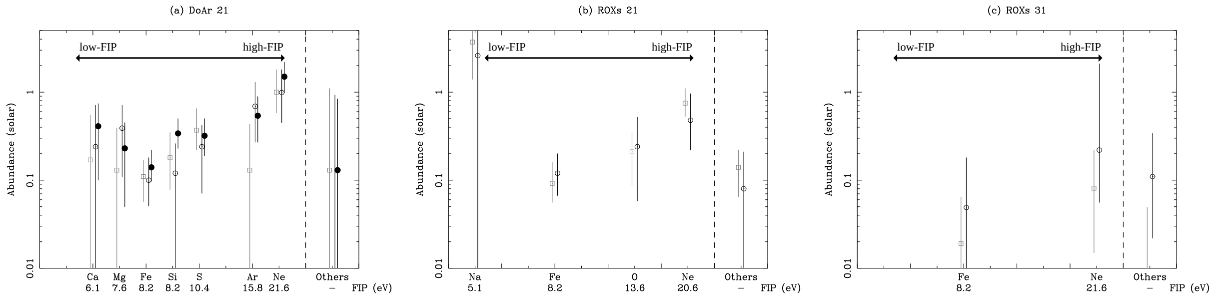

Fig. 6.6.— Elemental abundances of (a) DoAr21, (b) ROXs21, and (c) ROXs31. Errors indicate the 90 % confidence limits. The horizontal axis shows corresponding elements with their FIP values (eV). Gray squares, black-open, and black-filled circles represent abundances in the quiescent, first and second flare phases, respectively.

Table 6.3: Best-fit parameters of DoAr21, ROXs21, and ROXs31

Source*	— DoAr21 —			— ROXs21 —		— ROXs31 —	
Phase†	Q‡	F1	F2‡	Q	F	Q	F
$< kT_1 >$	2.5	2.9	2.9	0.69	0.86	0.23	0.27
(keV)	(2.4–2.6)	(2.7–3.1)	(2.8–3.1)	(0.65–0.74)	(0.78–4.5)	(0.15–0.31)	(0.21–0.41)
$< kT_2 >$	...	...	...	1.8	2.6	1.5	2.0
(keV)				(1.6–2.1)	(2.3–3.1)	(1.2–1.7)	(1.8–2.5)
N_H	1.0	1.0	1.10	0.13	0.081	1.7	1.7
(10^{22} cm^{-2})	(0.97–1.1)	(0.96–1.1)	(1.06–1.13)	(0.079–0.16)	(0.038–0.11)	(1.1–2.1)	(1.0–2.5)
Abundances							
(solar)							
O	... §	... §	... §	0.21	0.24	... §	... §
				(0.086–0.37)	(0.058–0.52)		
Ne...............	1.0	0.99	1.5	0.75	0.48	0.081	0.22
	(0.58–1.8)	(0.45–1.8)	(0.98–2.2)	(0.53–1.1)	(0.22–0.96)	(0.015–0.22)	(0.056–2.1)
Na	... §	... §	... §	3.7	2.6	... §	... §
				(1.4–8.2)	(<7.6)		
Mg	0.13	0.39	0.23	... §	... §	... §	... §
	(<0.39)	(0.11–0.71)	(0.050–0.45)				
Si	0.18	0.12	0.34	... §	... §	... §	... §
	(0.078–0.35)	(<0.26)	(0.23–0.50)				
S	0.37	0.24	0.32	... §	... §	... §	... §
	(0.22–0.65)	(0.071–0.42)	(0.19–0.50)				
Ar...............	0.13	0.69	0.54	... §	... §	... §	... §
	(<0.43)	(0.27–1.3)	(0.27–0.88)				
Ca	0.17	0.24	0.41	... §	... §	... §	... §
	(<0.55)	(<0.73)	(0.10–0.74)				
Fe...............	0.11	0.10	0.14	0.092	0.12	0.019	0.049
	(0.057–0.17)	(0.051–0.18)	(0.097–0.22)	(0.056–0.16)	(0.067–0.20)	(<0.064)	(<0.18)
Others...........	0.13	0	0.13	0.14	0.080	0.0080	0.11
	(<1.1)	(<0.93)	(<0.84)	(0.065–0.22)	(<0.21)	(<0.049)	(0.022–0.34)
$< L_X >$ ‖	28	34	38	1.5	1.9	22	30
(10^{30} ergs s^{-1})							
reduced-χ^2(d.o.f.)	0.953(175)	0.910(150)	1.03(275)	1.12(96)	1.07(88)	1.11(67)	0.931(85)

*The 1-T model for DoAr21 and the 2-T model for ROXs 21 and ROXs31 are used (see text). Parentheses indicate the 90 % confidence limits.

†See Figure 6.3.

‡The boundary between phases Q and F2 is not clear because of the existence of a rising part (Figure 6.3), however there are no significant differences in parameters when the boundary is changed.

§These are assumed to be the same as "Other" elements.

‖Absorption-corrected luminosity in 0.5–9.0 keV.

We investigate the Na overabundance seen in ROXs21 in further detail (Figure 6.6b), because Na is a relatively rare element compared with the major 4N nuclei (^{12}C, ^{16}O, etc) and because the Na Lyman-α line lies near the Lyman-β line of the more abundant element Ne. Figure 6.7a shows the best-fit result when the Na abundance is collectively varied with the other elements. There is significant data excess at ≈1.2 keV, near the Lyman-β line of Ne (1.211 keV). The intensity ratio of Lyman-β to -α lines of Ne should increase as a function of kT for $kT < 1$ keV and stay almost constant at ≈ 7 for $kT > 1$ keV (Mewe et al., 1985), hence 1/7 of the Lyman-α flux should be an upper-limit to the Lyman-β line flux. Since the flux of the Ne Lyman-α line is fairly strong, the Lyman-β line flux is well constrained as seen in Fig 6.7a. Thus the excess flux should originate from another element; the Lyman-α line of Na (1.236 keV) is the best candidate. Allowing the Na abundance to be a free parameter improves the fit as demonstrated in Figure 6.7b. The reduction of χ^2 (d.o.f.) from 114 (97) to 108 (96) is significant with ∼98 % confidence level for the F-test [2] (Bevington & Robinson, 1992).

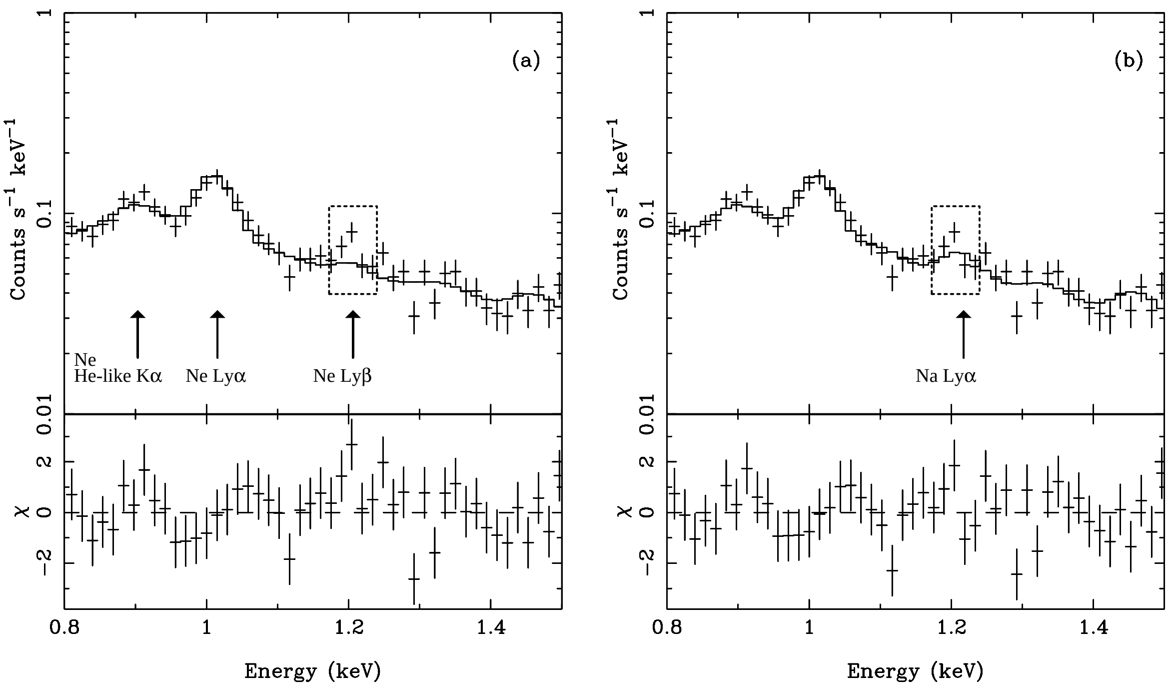

Fig. 6.7.— Close-up view of the fitting results of ROXs21 in phase Q, in which the Na abundance (a) is varied collectively with the "other" elements and (b) is treated as a free parameter. Arrows and dashed squares show the positions of K-shell lines from (a)Ne/(b)Na and the prominent feature near the Lyman-α line of Na, respectively.

[2] A statistical test to check the difference between the fitted and parent functions. See §11.4 in Bevington & Robinson (1992).

Using the GIS spectra of DoAr21, we investigate the long-term (∼yr) behavior of the spectral parameters. Since the energy resolution does not allow us to separate the emission lines from the key elements, we varied the abundances assuming the same value for all elements. The best-fit luminosity shows long-term variability in the range of (2–8)$\times 10^{31}$ ergs s^{-1}. The best-fit temperatures and abundances also vary from 2.5 to 4 keV and 0.15 to 0.5 solar, respectively. Both are possibly correlated with the X-ray luminosity as shown in Figure 6.8(a) and 6.8(b). The $N_{\rm H}$ value is consistent with being constant within a factor of ≈ 2.

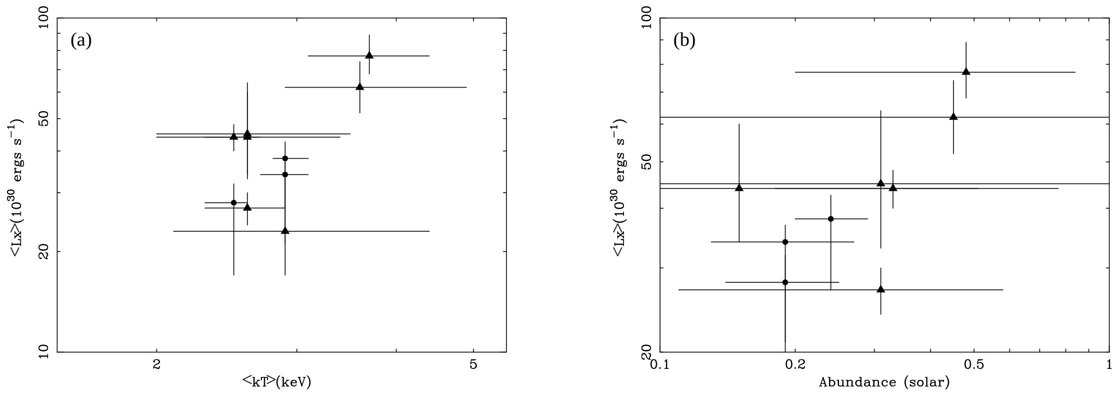

Fig. 6.8.— X-ray luminosity plotted against (a) the plasma temperature and (b) the mean abundance of DoAr21. Circles and triangles represent the data of ACIS and of GIS. Errors indicate the 90 % confidence limits.

6.2.5 Temperature structure

The high-quality spectra of the long *Chandra*/ACIS exposure reveal that the 2-T model gives a better fit than the 1-T model for ROXs21 and ROXs31. This supports previous 2-T model fits for some fractions of other bright TTSs (Carkner et al., 1996; Yamauchi et al., 1996; Preibisch, 1997; Costa et al., 2000; Ozawa, 2000; Tsujimoto et al., 2001). DoAr21, on the other hand, displays a simple 1-T spectrum with $< kT > \sim 3$ keV; it has no additional soft component. Since the age of DoAr21 (∼10^5 yr) is younger than those of ROXs21 and ROXs31 (∼10^6 yr: Nürnberger et al., 1998), coupled with the result of Tsujimoto et al. (2001) that 2-T spectra are found more often in older TTSs than in younger protostars, we speculate that the soft component (∼0.5 keV), probably a relatively steady corona, appears gradually as the system increases its age, finally reaching solar-like corona. In this scenario, the hard component (2–3 keV) would be the sum of unresolved flares.

6.2.6 Chemical composition of X-ray emitting plasma – the FIP and IFIP effects

Generally, the abundances of a stellar corona of MS stars may be different from those in a photosphere, depending on the FIP of the relevant elements. For instance, in the solar corona, elements with low FIP are overabundant relative to the solar photospheric values ("the FIP effect", Feldman 1992). Recent observations, however, showed that in some of stellar coronae the abundances of high-FIP elements are larger than the others (the Inverse FIP = IFIP effect). The IFIP effect appears in X-ray active stars, while the FIP effect is generally seen in less active stars (Audard et al., 2001; Brinkman et al., 2001; Güdel et al., 2001a,b,c; Huenemoerder et al., 2001; Kastner et al., 2002). The dependence of abundance on X-ray activity is also existent within individual stars; some sources show the enhancements in abundance from quiescent to flare phases, or even within a single flare phase (e.g., HR1099, Audard et al. 2001; V773 Tau, Tsuboi et al. 1998). Due to the limited statistics and samples, however, it is unclear whether or not abundance variations between quiescent and flare phases are common and the FIP/IFIP effects are present in low-mass YSOs.

The coronal abundances of DoAr21, ROXs21, and ROXs31 are sub-solar, consistent with the average values of low-mass YSOs (0.3 solar: Figure 5.4). From Figure 6.6(a) and (b), we see that both high-FIP (Ne and Ar) and low-FIP (Na, Mg, and Ca) elements show higher abundances than the other elements (the IFIP and FIP effects).

For the abundances in the solar corona, the FIP effect appears in elements with FIPs below 10 eV. A possible interpretation for the FIP effect is as follows (Feldman, 1992). The low-FIP elements (FIP $<$ 10 eV) are collisionally ionized in the chromosphere at 6000–7000 K temperature and electric fields would preferentially transfer them to the upper coronal region. DoAr21 and ROXs21 are a K0 star and a binary of K4 with M2.5, respectively, hence have surface temperatures of 4000–5000 K, which is 0.6–0.8 times of that of the sun (Nürnberger et al., 1998). If we simply assume that the FIP-effect energy-limit is a linear function of the surface temperature, it should be shifted from 10 eV to 6–8 eV, which is near Mg (FIP = 7.8 eV) and Ca (6.1 eV), but well above Na (5.1 keV). The abundance enhancements of Mg, Ca and Na provide independent evidence supporting the universality of the scenario proposed by Feldman (1992).

The X-ray luminosities of our TTS samples are a few $\times$ 10^{30-31} ergs s^{-1}, which is significantly higher than typical FIP sources of $\leq 10^{29}$ ergs s^{-1} (such as the sun, π^1 UMa, and χ^1 Ori; Güdel et al. 2001c). The high luminosity may also be responsible for the IFIP effect we observed. A related issue would be the dramatic abundance increase in the giant flare of ROXs31 (§6.2.7).

Güdel et al. (2001c) proposed a possible scenario for the IFIP effect. During the X-ray active phase, the high-energy non-thermal electrons (§2.3.1) produce a "downward-pointing" electric field, which suppresses the transfer of the ionized low-FIP elements into the corona. The electrons also lose the kinetic energy at the photosphere by collisional process, then heat up cool elements to a plasma temperature, making the abundance increase during the flare. The radio gyro-synchrotron emission from DoAr 21 and ROXs31 further supports this idea, because this is the direct evidence for the presence of the high-energy electrons. Since the abundance increase should be correlated with the non-thermal radio flux variations, simultaneous radio and X-ray observations would help to constrain physical models.

Another possibility for the IFIP effect (ionization mechanism of high-FIP elements) is photo-ionization by coronal X-rays, which is proposed to explain a solar flare in which Ne is enhanced relative to O (Shemi, 1991; Schmelz, 1993). Since sources with the IFIP effect have large X-ray luminosity of $< L_X > = 10^{29}$–10^{32} ergs s^{-1} (HR 1099, Brinkman et al. 2001; AB Dor, Güdel et al. 2001a; YY Gem, Güdel et al. 2001b; II Pegasi, Huenemoerder et al. 2001; and TW Hydrae, Kastner et al. 2002), they should suffer large X-ray photo-ionization at the photosphere, which increases the ionization fraction of high-FIP elements. This may also well explain the abundance increase in the X-ray active phase (Figure 6.8b). We should note, however, that this simple logic can work for all (both FIP and IFIP) elements, hence does not cause the enhancement of the ionization fraction of high-FIP elements. In order to solve the IFIP effect considering the effect of photo-ionization, other constraints (e.g., geometrical effect) should be considered.

6.2.7 Giant flare from ROXs31

For the detailed study of spectral evolution during the flare, we make and fit time-sliced GIS spectra of the giant flare from ROXs31 in obs-A2 (Figure 6.4c). The time intervals are shown in Figure 6.9 (left). The spectra show strong Kα emission of He-like Fe at $\approx$ 6.7 keV, hence we let the Fe abundance to vary. The flare spectra are well fitted by a 1-T model in contrast to the quiescent phase (2-T model). Since the flux of the soft component in the quiescent phase is 10–100 times lower than that of the flare flux, it is highly possible that the soft component does exist during the flare but is hidden by the more luminous harder component.

Figure 6.9 (right) shows the best-fit parameters for each time interval. As shown in the figure, this flare has an unusual time profile. The light curve increases slowly over $\sim$15 ks (see also Skinner 2000). The temperature reaches its peak value before the flux maximum and stays nearly constant during the decay phase.

The absorption ($N_{\rm H}$) and abundances dramatically change from quiescent to flare; $N_{\rm H}$ in the flare is $\sim 7.1\times10^{21}$ cm^{-2}, about two times smaller than that of the quiescent phase (obs-BF) of 1.7×10^{22} cm^{-2}, while the abundances increase by a factor of 3–30 from quiescent (0.01–0.1 solar) to the giant flare (0.26–0.29). They do not change during the flare. This could be due to the chromospheric evaporation by high-energy electrons, which may be produced just after magnetic reconnection. Evaporation by the flare X-rays may not be important, because the abundances and absorption do not change much during the flare. Thus, in the case of the IFIP effect in the giant flare of ROXs31, the high-energy electron origin is more likely than X-ray irradiation scenario.

The peak luminosity of $\sim 10^{33}$ ergs s^{-1} and temperature of $\sim$10 keV are comparable to the giant flare of another TTS binary system V773 Tau (Tsuboi et al., 1998). However, the time profile of the plasma temperature is different from that of V773 Tau. The rise timescale of ROXs31 is much longer ($\sim$3 ks). This may be due to a large magnetic loop (§8.7), although the effect of the partial occultation of the flare due to the stellar rotation may also be conceivable. The temperature arrives at the peak value preceding the flare peak and stays nearly constant at 4–5 keV in the decay phase. These imply the existence of successive energy release due to the magnetic reconnection and that the generation and heating of the plasma occur even in the decay phase, as suggested by Tsuboi et al. (1998); Schmitt & Favata (1999); Favata & Schmitt (1999). Such a phenomenon is also seen in long duration event (LDE) flares of the sun (Isobe et al., 2002).

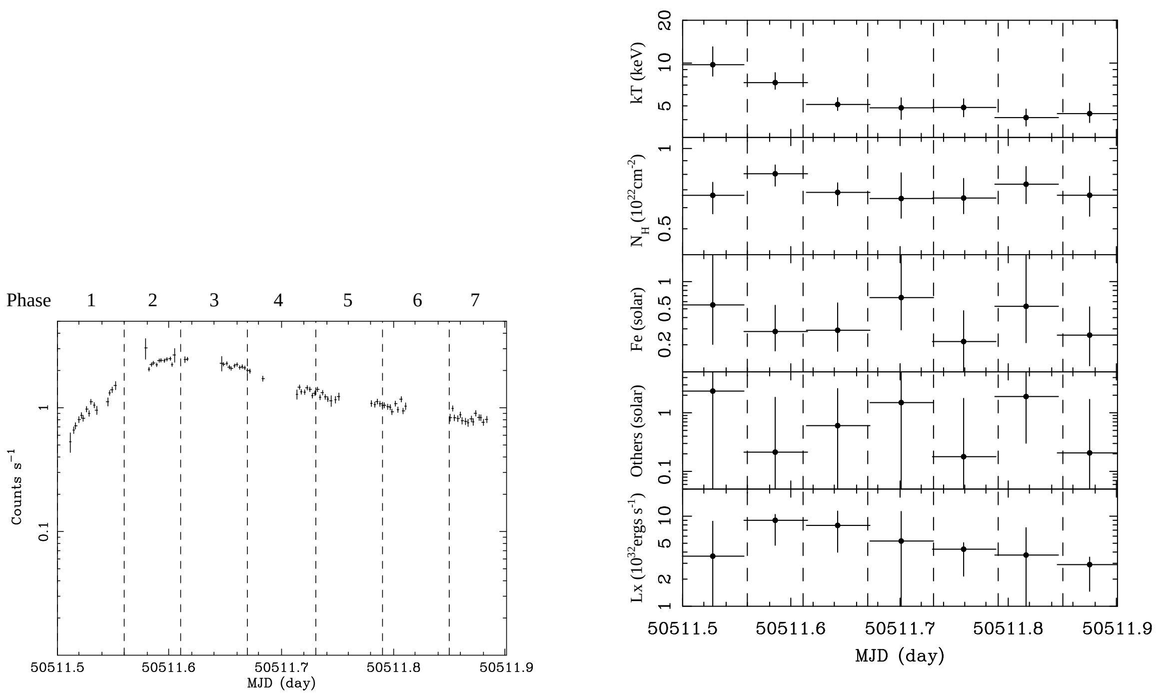

Fig. 6.9.— (left) A magnified view of the light curve of ROXs31 during the giant flare in 0.5–9.0 keV (Figure 6.4c). (right) Time profiles of the best-fit temperature, absorption column, abundances of Fe and other elements, and X-ray luminosity of ROXs31 during the giant flare in obs A2. Errors indicate the 90 % confidence limits.

6.3 Other T Tauri Stars

6.3.1 A-20 – GY12

A class III source GY12 (GSS30-IRS2) shows three flares in obs-A (Figure A.3). GY12 was also detected at the ACIS-S2 chip in obs-BF, hence we make light curve and time-sliced spectra as shown in Figure 6.10. Since $N_{\rm H}$ of $3.6^{+0.1}_{-0.2}\times10^{22}$ cm^{-2} is the same as A-20, the X-ray emitting source in obs-BF is surely GY12 regardless of the large positional uncertainty. In Figure 6.10, we detect four flares with our criterion (§5.5). We therefore conclude that GY12 is an X-ray active source showing frequent flare activity, 3–4 flares per 100 ks.

Near GY12, two class I sources GSS30-IRS1 and LFAM1 = GSS30-IRS3 are located with the respective separation angles of $\sim$17″ and $\sim$10″ from GY12. Also, CO observations revealed the expanding shell around them with the radius and expanding velocity of $\sim$15″ ($\cong$ 2000 AU) and $\sim$0.7 km s^{-1} (Zhang et al., 1997), which is probably due to cloud disruption as a result of young star formation. Although we see no significant X-rays from the two class I sources and from the shell for both observations, it may be conceivable for future works whether or not such complex systems affect the high flare frequency of GY12.

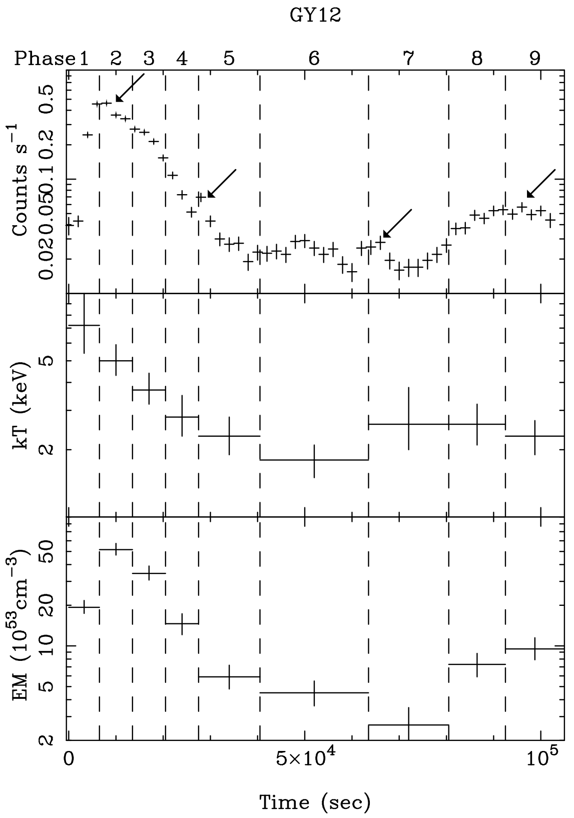

Fig. 6.10.— (top) Light curve in 0.5–9.0 keV and (middle and bottom) time evolution of kT and EM of GY12 in obs-BF. Flare time bins (§5.5) are represented by arrows.

6.3.2 A-23 – GY21

A class II A-23 = GY21 shows two flares in obs-A (Figure A.1). The spectra show strong He-like Fe emission at ∼6.7 keV both in the flare and quiescent phases (Figure 6.11). We hence fit them by the MEKAL model with the abundance to be free and obtain significantly higher values than the other sources; 1.0 (0.5–1.6), 3.5 (>0.6), and <15 solar for the quiescent, first flare, and second flare phases, respectively. GY21 thus shows not only over-abundance but also a possible abundance increase during the flare like HR1099 (Audard et al., 2001), V773 Tau (Tsuboi et al., 1998), and ROXs31 (Imanishi et al., 2002a, see also 6.2.7), although uncertainties are large. The expected magnetic field of the first flare (see §8.3.2) is among the largest values ($\gtrsim$1000 G). Since it has been considered that the abundance anomaly is related to the activity at the stellar surface (e.g., Güdel et al., 2001c), it would be fruitful for future works to investigate whether or not such a large magnetic field has any correlation with its abundance anomaly. Possible binary nature of GY21 and S2 = A-24 (Haisch et al., 2002) would also be conceivable (see also §6.3.3).

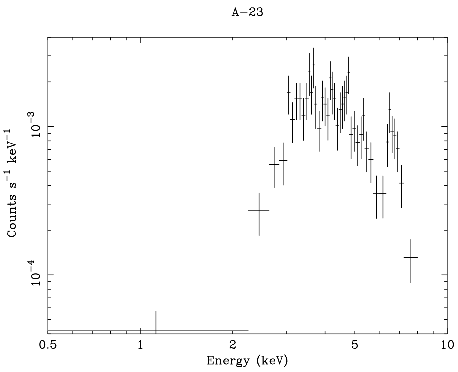

Fig. 6.11.— Time-averaged spectrum of A-23 = GY21. Prominent line emission is seen at ∼6.7 keV.

6.3.3 A-24 – S2

A class II source S2 = A-24 exhibits a clear flare with about ten times larger flux than that in the quiescent phase (Figure A.2). Similar to GY21 (§6.3.2), the spectra of S2 show strong He-like Fe emission (Figure 6.12). We fit them by the MEKAL model with the abundance to be free and obtain 0.6 (0.4–0.8) and 0.7 (0.5–0.9) solar for the quiescent and flare phases, respectively. S2 was also detected on ACIS-S2 in obs-BF. Although the light curve in obs-BF shows no flare, the time-averaged $< kT >$ ($2.9^{+0.4}_{-0.3}$ keV) and $< L_X >$ (9.1×10^{30} ergs s^{-1}) are significantly larger than those in the quiescent phase of obs-A, while the abundance is lower (0.2±0.1 solar). Since the absorption is nearly the same ($4.2^{+0.2}_{-0.3}\times10^{22}$ cm^{-2}), it is less possible that another source emits X-rays in obs-BF

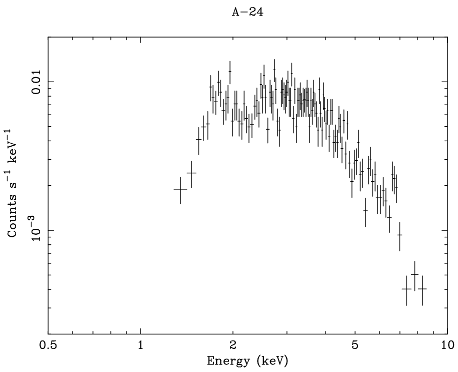

Fig. 6.12.— Time-averaged spectrum of A-24 = S2. Prominent line emission is seen at ∼ 6.7 keV.

despite of large positional uncertainty. S2 therefore has the large variation of $< L_X > = 10^{30}$–10^{31} ergs s^{-1} together with that of the abundance = 0.2–0.7 solar, although its mechanism is an open question.

Interestingly, both members of a candidate wide binary system, GY21 and S2 (Haisch et al. 2002; see also Figure 6.18) show overabundance. This may indicate anomaly of global chemical composition of this region, although this interpretation is insufficient to explain the abundance variations of GY21 and S2.

6.3.4 A-34 – GY51

The offset between A-34 and the nearest class II source GY51 is $\sim 0.''72$, which is slightly larger than the positional uncertainty of the *Chandra* observation ($\sim 0.''5$) at its small off-axis angle ($\sim 1.'1$, see Figure 5.3). However, the $N_{\rm H}/A_V$ and $< L_X >/L_{\rm bol}$ ratios between A-34 and GY51 are respectively $\sim 1.7\times10^{21}$ cm^{-2} mag^{-1} and $\sim 10^{-3}$, which are typical of YSOs (Figure 7.6 and 7.7). We hence regard that A-34 is surely associated with GY51. A detection of a solar-like flare (Figure A.1) is also consistent with out idea.

6.3.5 A-41 – S1

A class III S1 is among the brightest and hottest sources in ρ Oph ($L_{\rm bol} \sim 1000\ L_\odot$, $T_{\rm eff} \sim$ 20000 K), which is classified as “Herbig Ae/Be stars” (HAeBes = intermediate-mass YSOs: André et al., 1988). André et al. (1988) detected polarized non-thermal radio emission, which probably comes from gyro-synchrotron particles. This indicates that S1 has relatively strong magnetic field.

In obs-A, we detect significant X-rays (A-41) with a small-amplitude flare near the end of the observation (Figure A.3). S1 was also detected at the ACIS-S2 chip in obs-BF (Hamaguchi et al., 2002). The light curve of S1 in obs-BF shows no apparent flare, although it seems to decrease throughout the observation with the e-folding time of $\sim$40 ks.

Figure 6.13 shows time-averaged spectra of S1 in (left) obs-A and (right) obs-BF. Except for a marginal hump at $\sim$6.5 keV in obs-BF, clear emission lines can not be seen, indicating either low metal abundance or non-thermal nature. Also, there is possible edge absorption feature around 4 keV in obs-A. We hence fit them by the power-law model, as well as by the MEKAL model with abundance to be free. For obs-A, we separately make and fit the spectra in the flare and quiescent phases. Table 6.4 summarizes the fitting results. Both the thermal and non-thermal models well reproduce the spectra. The derived abundance of the thermal model is relatively low of 0–0.2 solar. For obs-A, we additionally apply the fitting with an edge absorption, which slightly reduces the

χ^2 values. This reduction is significant with ~96 (thermal) and ~99 (non-thermal) % confidence levels for the F-test (Bevington & Robinson, 1992).

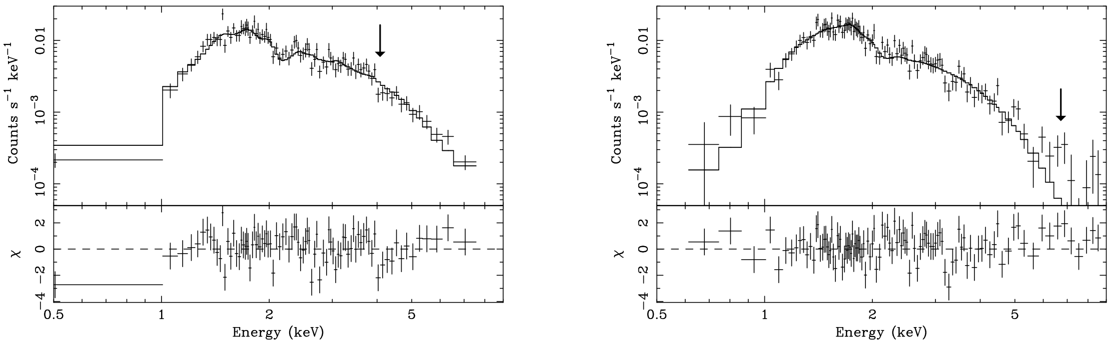

Fig. 6.13.— Time-averaged spectra of S1 in (left) obs-A and (right) obs-BF. The upper panels show data points (crosses) and the best-fit MEKAL model (solid line), while the lower panels show residuals from the best-fit model. Arrows indicate (left) possible edge absorption and (right) marginal hump (see text).

If X-rays are thermal in origin, $< kT >$ (~2–3 keV) and the $< L_X > /L_{\rm bol}$ ratio (~10^{-6}) are similar to those of HAeBes (Hamaguchi, 2001). Flare-like time variability is also consistent. If non-thermal X-rays are the case, on the other hand, most plausible scenario is bremsstrahlung emission from non-thermal electrons accelerated just after the magnetic reconnection event (§2.3.1), which is the same mechanism as hard (>10 keV) X-rays of the sun (§2.3.1). This is further supported by the radio observation which suggests the presence of MeV electrons around S1 (André et al., 1988). However, this requires that thermal plasma generated via magnetic reconnection should have lower temperature than those of the sun, because the non-thermal X-rays are dominant over the thermal component above ~1 keV. To verify which is the real case, more sensitive observations (for example, with *XMM-Newton*) would be needed.

The threshold energy of the edge absorption is ~3.9 keV, which corresponds to neutral Ca (4.04 keV) or ionized Ar (Ar XVI: 3.95 keV) with the temperature of ~$10^{6.6}$ K. However, the former is less possible, because it requires the extremely large Ca abundance of ~500 solar. In the case of Ar, light elements below N are fully ionized and do not affect the absorption, hence the unusually large abundance of Ar does not needed. It is therefore probable that the warm absorber makes Ar edge feature. Considering that the edge feature is not seen at the spectrum in obs-BF, the absorber should have much smaller size than the stellar radius and be located near the stellar surface, if we interpret the disappearance of the edge feature in obs-BF as the effect of the occultation. However, its detailed physical condition is still in discussion. More details about S1 are discussed in Hamaguchi et al. (2002).

Table 6.4: Best-fit parameters of S1

Model*	$< kT > / \Gamma$ †‡ (keV/–)	Abundance† (solar)	$< EM >$† (10^{53} cm^{-3})	N_H† (10^{22} cm^{-2})	E_{edge}†§ (keV)	τ†‖	$< L_X >$#	χ^2/d.o.f.
– obs-A –								
Mekal(Q)	1.9	0.20**	2.6	2.2**	···	···	2.2	138.6/126
	(1.7–2.1)	(0.05–0.39)	(2.2–3.2)	(2.1–2.4)				
(F)	2.7	···	2.3	···	···	···	2.3	···
	(2.1–3.0)		(1.9–2.9)					
Mekal*Edge(Q)	2.2	0.16**	2.3	2.1**	3.9**	0.47**	2.0	126.8/124
	(2.1–2.4)	(0.03–0.33)	(2.2–2.3)	(2.0–2.2)	(3.8–4.0)	(0.29–0.66)		
(F)	3.4	···	2.0	···	···	···	2.3	···
	(2.9–4.1)		(1.9–2.3)					
Power(Q)	3.3**	···	···	2.8**	···	···	5.8	142.2/128
	(3.1–3.5)			(2.6–3.0)				
(F)	···	···	···	···	···	···	6.6	···
Power*Edge(Q)	2.9**	···	···	2.6**	3.9**	0.56**	4.1	127.3/126
	(2.6–3.0)			(2.2–2.7)	(3.8–4.1)	(0.37–0.76)		
(F)	···	···	···	···	···	···	4.8	···
– obs-BF –								
Mekal	1.6	0.0	4.1	1.9	···	···	2.6	117.6/105
	(1.5–1.9)	(<0.11)	(3.4–5.0)	(1.7–2.0)				
Power	3.4	···	···	2.4	···	···	7.2	116.3/106
	(3.1–3.6)			(2.2–2.6)				

*Applied models; Mekal: thin-thermal plasma model, Power: power-law model, Edge: edge absorption. “Q” and “F” for obs-A denote the spectra in the quiescent and flare phases, respectively.
†Parentheses indicate the 90 % confidence limit.
‡Best-fit temperature and photon index for the Mekal and Power model, respectively.
§Threshold energy of the edge absorption.
‖Absorption depth at E_{edge}.
#Absorption-corrected X-ray luminosity (10^{30} ergs s^{-1}) in 0.5–9.0 keV.
**Parameters are derived by assuming the same values for the quiescent and flare spectra.

6.3.6 A-79/BF-17 – GY195

A class II source GY195 shows significant X-rays in both observations (A-79 and BF-17), with three flares (Figure A.2). In particular, GY195 shows unusual flares in obs-A. First, a sharp flare occurs at $t \sim 35$ ks, then reaches its peak about 50 times larger than the pre-flare flux. During the decay phase ($t \sim 50$ ks), a second flare appears but the rise and decay timescales are larger. Gagné (2001) interpreted this series of flares as a result of a re-heating event of the single loop, like quasi-periodic flares from YLW15A (Tsuboi et al., 2000). We hence make and fit the time sliced spectra of A-79 as shown in Figure 6.14, however no significant sign of increase of kT is found at the second flare but it keeps almost constant of 3–4 keV (phases 3–5 in Figure 6.14), which is a sharp contrast to the case of YLW15A (Figure 2 in Tsuboi et al., 2000).

6.3.7 BF-10 – WL22

The X-ray spectrum of a class II BF-10 = WL22 exhibits clear line structure at ∼3.2 and ∼3.9 keV (Figure 6.15). The line energies correspond to He-like Ca and Ar. We hence relax the abundances of these elements to be free and fit it by the MEKAL model. The best-fit $< kT >$ and $N_{\rm H}$ are 2.1 keV and $12{\times}10^{22}$ cm^{-2}, respectively (Table 5.2), while the abundances of Ar and Ca are $2.7^{+8.3}_{-2.7}$ and $5.0^{+7.9}_{-4.1}$ solar. Thus Ca is extremely overabundant, although the mechanism is an open question.

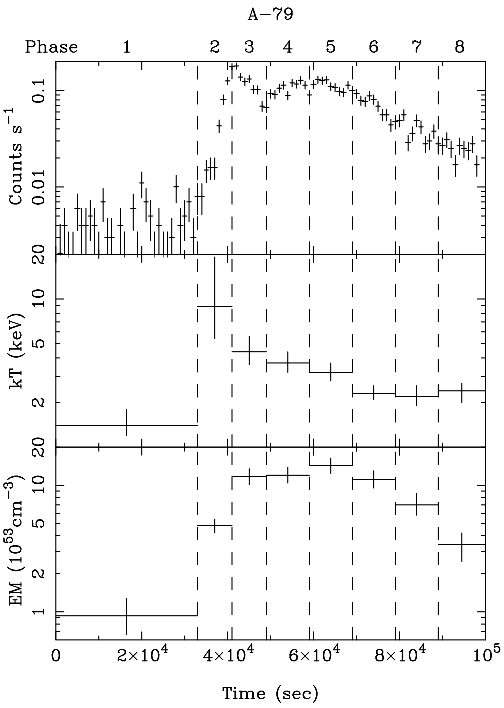

Fig. 6.14.— (top) Light curve and (middle and bottom) time evolution of kT and EM of A-79 = GY195.

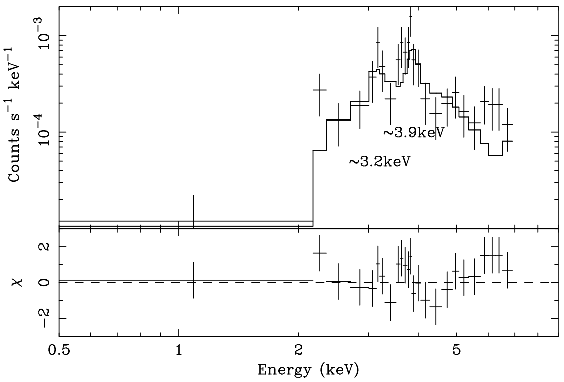

Fig. 6.15.— Spectrum of BF10 = WL22. The upper panel shows data points (crosses) and the best-fit MEKAL model (solid line), while the lower panel shows residuals from the best-fit model. The line structure at ∼3.2 keV and ∼3.9 keV is due to He-like Ar and Ca.

6.4 Brown Dwarfs

Imanishi et al. (2001b) did a systematic X-ray search from bona-fide and candidate brown dwarfs in ρ Oph. Here, we show details.

6.4.1 X-ray detection from brown dwarfs in ρ Oph

In the fields of view of obs-A and obs-BF, 18 late M dwarfs have been reported based on the water vapor absorption at λ = 2.4–2.5 μm (Wilking et al., 1999; Cushing et al., 2000). Among them, eight sources have the upper limit of the mass less than 0.08 $M_\odot$, which we call "bona-fide brown dwarfs" (here and after, BDs). Other seven sources have the lower limit of the mass less than 0.08 $M_\odot$, which is called "candidate brown dwarfs" (BD$_c$s)[3]. Table 6.5 shows their names and spectral types.

In the X-ray source catalogue (Table 5.2), we found X-ray counterparts for four BDs and BD$_c$s (A-30 = GY37, A-38 = GY59, BF-86 = GY310, and BF-S2 = GY141). Also, a BD$_c$ GY5 may be associated with a soft-band source A-S2, although Imanishi et al. (2001b) reported no X-ray emission from GY5 by using the NIR position of Barsony et al. (1997), which is $\sim 2''$ away from the 2MASS source. Since no apparent X-ray sources are found in the error radius of the other 11 catalogued BDs and BD$_c$s, we define a circle with a half radius of the PSF size around each IR position, then manually count X-ray photons. We note that a rather small source radius is selected so as to increase the signal-to-noise (S/N) ratio, particularly for faint X-ray sources. Nevertheless, as is demonstrated in the bright sources, the position error between IR and X-ray is always smaller than the source radius, because both have generally similar dependence on a source off-axis angle; both have the smaller values for sources with smaller off-axis angle. Therefore, most of the X-ray photons for the relevant BDs and BD$_c$s, if any, may fall in the source circles. Table 6.5 shows the X-ray counts thus counted. The mean background counts are estimated from the same regions used in §5.6. The soft band (0.5–2.0 keV) background counts (in units of 10^{-2} counts arcsec^{-2}) are 2.3 and 2.2 for obs-BF and obs-A, respectively, while those in the hard (2.0–9.0 keV) band are about three times larger, 6.8 and 6.5 for obs-BF and obs-A. The background counts in each source area are given in Table 6.5. We then separately calculate the confidence level (CL) of X-ray detection for the soft, hard, and total (0.5–9.0 keV) bands. Based on the Poisson statistics, we define the CL as

$$CL = \sum_{N'=0}^{N_0-1} e^{-N_{bg}} \frac{N_{bg}^{N'}}{N'!}, \tag{6.2}$$

[3]Imanishi et al. (2001b) regarded GY31, GY163, and GY326 as BD$_c$s. Now, however, the mass of these M dwarfs is regarded to be higher than the hydrogen burning limit (Wilking et al., 1999), hence we do not include them in the BD$_c$ sample.

where N_0 and N_{bg} are the detected and the background counts in the source circle, respectively (see e.g., Gehrels, 1986, and references therein). We set a detection (or an upper limit) criterion that the CL should be larger than 0.999 (= 3.3 σ) in any of the three energy band data. In Table 6.5, we show the maximum CL value for each source. For sources located in both fields of view (GY141 and GY202), we also estimate the CL for the combined data as well as the separate data. However, no higher CL value is obtained from all the sources. In addition to the seven X-ray sources, a BD$_c$ GY84 shows significant X-rays, although it may be possible that these X-rays are part of diffuse X-ray emission A-48 (see §6.6.2). We hence regard that the X-ray detection from GY84 is marginal.

Table 6.5: Bona-fide and candidate brown dwarfs in the ρ Oph cloud cores

Name	Sp. type*	ID†	X-ray‡	PSF§	X-ray counts‖			$1-CL$#	L_X**	$\log(L_X/L_{\rm bol})$	Ref‡‡
				(″)	Soft	Hard	BGD				
— Brown Dwarf (BD) —											
CRBR14	M7.5	A	···	5.7	4	0	0.5	ND (S)	<0.55	<-4.3	1
GY10	M8.5	A	···	3.2	2	0	0.2	ND (S)	<0.48	<-4.5	1
GY11	M6.5	A	···	3.3	1	1	0.2	ND (T)	<0.12	<-3.8	1, 2
CRBR31	M6.7	A	···	7.1	0	2	0.9	ND (H)	<0.56	<-3.6	2
GY64	M8	A	···	3.7	2	0	0.2	ND (S)	<0.93	<-3.5	1, 2
GY141	M8	BF	BF-S2	9.0	10	0	1.5	3.3×10^{-6} (S)	0.39	-3.4	2
		A	···	22.3	9	16	8.6	ND (S)	<0.33	<-3.5	
GY202	M7	BF	···	9.4	2	5	1.6	ND (S)	<1.2	<-3.7	1
		A	···	16.8	3	5	4.9	ND (S)	<2.0	<-3.4	
GY310	M8.5	BF	BF-86	9.2	190	56	1.5	$<1.0\times10^{-15}$ (T)	10	-3.4	1
— Candidate Brown Dwarf (BD$_c$) —											
CRBR15	M5	A	···	4.2	2	2	0.3	ND (S)	<1.1	<-4.2	1
GY5	M7	A	A-S2?	4.7	7	4	0.4	1.7×10^{-7} (S)	0.42	-4.8	1
GY37	M6	A	A-30	4.2	7	5	0.3	3.7×10^{-8} (S)	0.59	-4.2	1
GY59	M6	A	A-38	1.9	15	17	0.1	$<1.0\times10^{-15}$ (T)	2.6	-3.9	1
GY84††	M6	A	···	1.9	1	3	0.1	1.3×10^{-4} (T)	0.85	-4.7	1
GY218	M4.0	BF	···	7.2	3	5	0.9	ND (S)	<0.45	<-3.6	2
CRBR67	M4.4	BF	···	3.2	0	0	0.2	ND (–)	<0.31	<-3.5	2

*Spectral type determined by the water vapor absorption.
†Observation identification (see Table 5.1).
‡Identified X-ray sources picked up with the `wavdetect` command (see Table 5.2).
§Radius of the point-spread function.
‖X-ray counts in the soft (0.5–2.0 keV) and hard (2.0–9.0 keV) bands, and predicted background counts in the soft band within the source circle. Background counts in the hard band are ∼3 times larger than those in the soft band.
#CL is the confidence level of the source detection (Eq.6.2). Parentheses indicate the energy band in which the maximum CL value is obtained (S: 0.5–2.0 keV, H: 2.0–9.0 keV, T: 0.5–9.0 keV). ND represents non X-ray detection with $CL < 0.999$ (i.e., $1-CL > 10^{-3}$).
**Absorption-corrected luminosity (10^{28} ergs s^{-1}, "$< L_X >$" in the text) in 0.5–9.0 keV.
††X-ray emission may be part of diffuse emission A-48 (see §6.6.2).
‡‡References: (1): Wilking et al. (1999); (2): Cushing et al. (2000)

6.4.2 X-ray spectra and luminosities

For the brightest two sources —, one BD (GY310) and one BD_c (GY59) —, we could analyze the X-ray spectra (§5.6). Figure 6.16 shows their spectra. The best-fit plasma temperature (Table 5.2) is in the range of 1–4 keV.

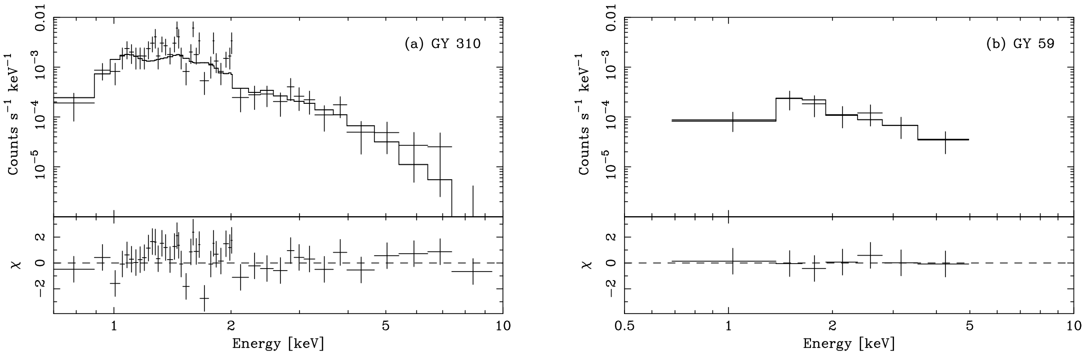

Fig. 6.16.— Time-averaged spectra of (a) GY310 and (b) GY59. The upper panels show data points (crosses) and the best-fit MEKAL model (solid line), while the lower panels are the data residuals from the best-fit model.

For the faint or non-X-ray sources, we assume the spectrum to be a thin-thermal plasma of 2 keV temperature (the mean value of the bright sources), while the absorption column is estimated from the empirical relation, $N_{\rm H} = 1.38{\times}10^{21}\ A_V$ cm^{-2} (§7.4.1), where A_V is the visual extinction derived with IR photometry (Wilking et al., 1999; Cushing et al., 2000). We then calculate the X-ray luminosities or those of the 99.9 % upper limits in the soft band, which is summarized in Table 6.5.

6.4.3 Time variability

Figure 6.17 shows the light curves of (a) GY310 and (b) GY59 in 0.5–9.0 keV, where the background levels are represented by dashed lines. The light curve of GY59 is flare-like, although our criterion (Eq.5.1) rejects this as a flare. This light curve is typical of those of low-mass main-sequence and pre-main-sequence stars; fast rise and slow decay. The flare-decay timescale ($\sim$10^4 s) is also the same. GY310, on the other hand, shows no clear flare, but exhibits aperiodic variability of flux change by a factor of $\sim$2 within 100 ks exposure. Since we see no large intensity variation in the background flux, we conclude that its variability is highly significant.

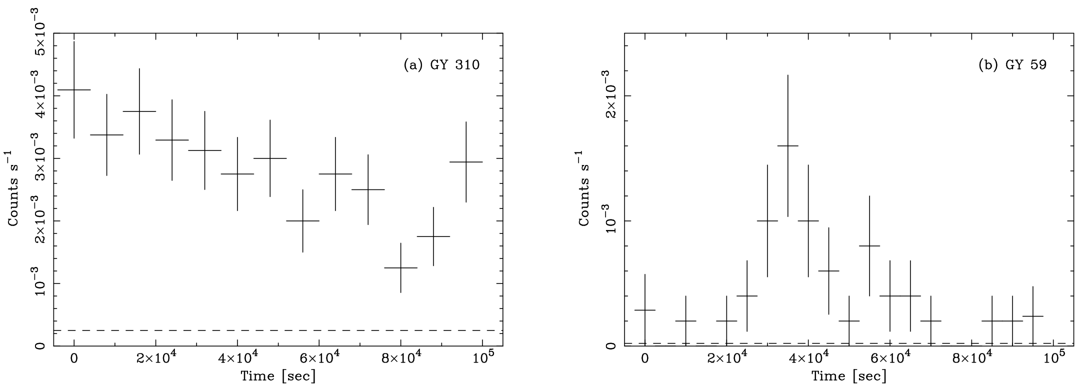

Fig. 6.17.— Light curves of (a) GY310 and (c) GY59 in 0.5–9.0 keV. Dashed lines show the background levels.

6.4.4 X-ray detection rate

We detect X-ray emission from two out of eight BDs and three out of seven BD$_c$s. The X-ray detection rate is thus 25 % (BD) and 43 % (BD$_c$). Neuhäuser et al. (1999) claimed the X-ray detection of only one BD (GY202) with *ROSAT*/PSPC in the same field. Our present observations find no X-rays from GY202 with the upper limit of 1.2×10^{28} ergs s^{-1}. Instead, we find a class II WL1 (A-78 = BF-16) within the PSPC error circle of GY202. This source emits X-rays with comparable luminosity to that of GY202 reported with *ROSAT*/PSPC. Conversely, Neuhäuser et al. (1999) found no X-rays with an upper limit of $\sim10^{28}$ ergs s^{-1} from all *Chandra* detected BD and BD$_c$s. They, however, estimated the X-ray luminosity assuming $< kT >= 1$ keV and $A_{\rm v}$ = a few mag (i.e., $N_{\rm H}$ = a few $\times10^{21}$ cm^{-2}), which may be significantly lower than the real case. We hence re-estimate the upper limit with the same assumption adopted in this paper (§6.4.2), then find that the *ROSAT* upper limit could be nearly one or two order magnitude higher than those of the original paper. If these newly estimated upper limits are adopted, we find no significant flux change from the *ROSAT* to the *Chandra* era.

In Table 6.5, we display the ratio of the X-ray ($< L_X >$) and bolometric ($L_{\rm bol}$) luminosities. The $< L_X >/L_{\rm bol}$ value lies between 10^{-3}–10^{-5}, which is similar to low-mass YSOs (Figure 7.7) and dMe stars (Giampapa et al., 1996), but is significantly higher than that of the quiescent solar corona; $\sim5\times10^{-7}$ (Vaiana & Rosner, 1978). We should also note that most of the upper limits of $L_X/L_{\rm bol}$ of X-ray non-detected BDs and BD$_c$s are scattered around 10^{-3}–10^{-5}, which are comparable with or slightly lower than those of X-ray detected BDs and BD$_c$s. We therefore suspect that these X-ray non-detected BDs and BD$_c$s may emit X-rays below (but possibly near) the current sensitivity limit of *Chandra*.

6.5 New YSO Candidates – A-29, A-31, and BF-36

6.5.1 Source selection and X-ray images

Imanishi et al. (2001a) suggested that most of unidentified sources are likely background active galactic nuclei (AGNs; see also §6.6). However, some fractions would be IR-faint cloud members, possibly brown dwarfs and/or very young stellar objects like class 0–I protostars. To search for new YSO candidates, we select the unidentified sources located near 850 μm clumps (Johnstone et al., 2000), then find three candidates (A-29, A-31, and BF-36: Imanishi et al., 2002b) in the dense millimeter/sub-millimeter cores of SM1/SMM J16264−2424 and SMM J16264−2423 in ρ Oph-A, and B1-MM4/SMM J16272−2430 in ρ Oph-B1 (Motte et al., 1998; Johnstone et al., 2000).

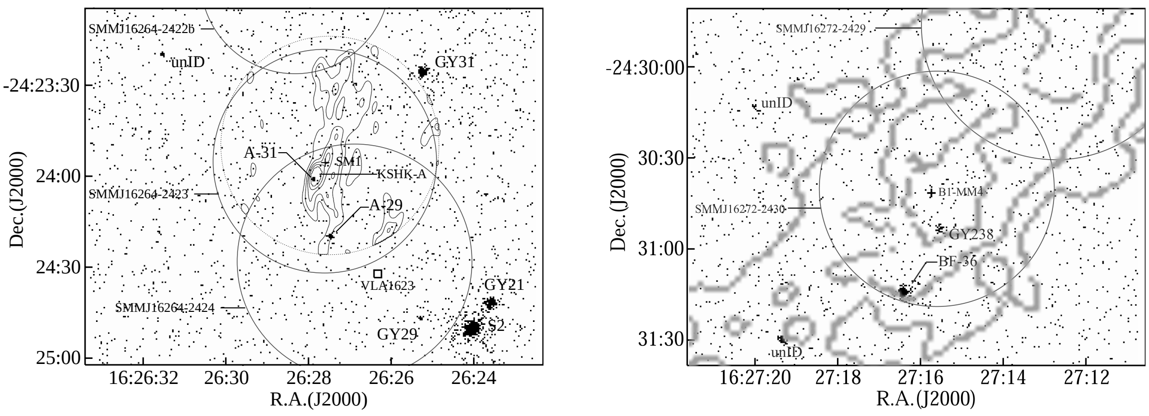

Fig. 6.18.— ACIS images around the mm cores (left) SM1 and (right) B1-MM4 in the 2.0–9.0 keV band. The contour is the (left) 3 mm and (right) 1.3 mm radio intensities (Motte et al., 1998; Kamazaki et al., 2001). Crosses, Large solid and dotted circles represent the center of each mm core, size of 850μm clumps (Johnstone et al., 2000) and field of view of the 3 mm observation, respectively. A square shows the position of the class 0 source VLA 1623. Other X-ray sources are known YSOs (GY21, S2, GY29, GY31, and GY238) and unidentified sources (designated as unID).

Figure 6.18 (left) shows the ACIS image of obs-A around SM1 in the hard X-ray band (2.0–9.0 keV), which is overlaid on a 3 mm contour map (Kamazaki et al., 2001). Large circles represent the 850 μm clumps (Johnstone et al., 2000). We see two point-like sources (A-29 and A-31) near the center of the 850 μm clump SMM J16264−2424 and at only $\sim 2''$ away from the center of the 3 mm core A (hereafter, KSHK-A). Since there is no significant soft X-ray (0.5–2.0 keV) from A-29 and A-31, they are deeply embedded in the cores. Another point source located near the core, a class II source GY29 (A-27), on the other hand, is clearly visible in the soft band because of relatively small absorption ($N_{\mathrm{H}} = 2.5\times10^{22}$ cm^{-2}; Table 5.2), hence may be located in front of the core.

The hard band (2.0–9.0 keV) ACIS image near ρ Oph B1 is shown in Figure 6.18 (right). There is a hard X-ray source (BF-36) about 30$''$ south of the 1.3 mm peak B1-MM4. A class II source GY238 (BF-33) is also appeared near the center of SMM J16272$-$2430, which would be located in the clumps, as supported by the large absorption of $N_{\mathrm{H}} = 4\times10^{22}$ cm^{-2} (Table 5.2).

6.5.2 Time variability

Figure 6.19 shows the X-ray light curves (background is not subtracted) of A-29, A-31, and BF-36 in the 2.0–9.0 keV band. We have detected solar-like flares from A-29 and BF-36 (§5.5). The light curve of A-31 also seems to be time variable; A-31 has only 12 photons and about 80 % of them (10/12) are concentrated in a limited time interval of $\sim$30 ks. We estimate the chance probability of such a photon clustering from a constant-flux source to be less than 1 % with the Kolmogorov-Smirnov test (Press et al., 1992). Thus the time variability of A-31 is also significant. The X-ray active time intervals are shown with dotted vertical lines in Figure 6.19 and are referred as the flare phase hereafter. The hard band counts in the quiescent phase (time periods outside of the flare phase) for A-29, A-31, and BF-36 are 5, 2 and 81, while those of the expected background counts are 0.7, 0.5, and 1.8, respectively. This means that A-31 has no significant quiescent flux with $\geq$ 99.9 % of the confidence level (Poisson statistics; see §6.4.1).

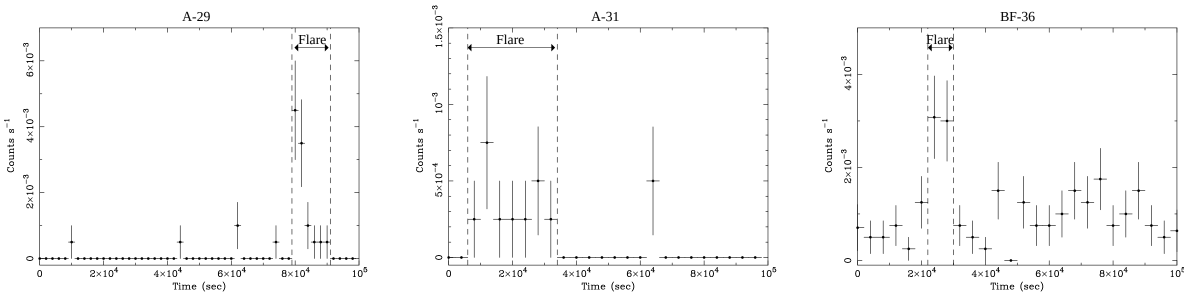

Fig. 6.19.— Light curves of (left) A-29, (middle) A-31, and (right) BF-36 in the 2.0–9.0 keV band. The time bins of each data point are 2000 (A-29), 4000 (A-31), and 4000 (BF-36) s. The arrows indicate the times of the flare phase (see text).

6.5.3 X-ray spectra and luminosities

Figure 6.20 shows the X-ray spectra of A-29, A-31, and BF-36 during the flare phases and that of BF-36 in quiescent. We fit them by the MEKAL model with the fixed abundance of 0.3 solar. However, reasonable constraint can not be obtained on $< kT >$ and $N_{\rm H}$ with the limited statistics for A-29 and A-31. We hence fix the temperature at three typical values (1, 5, and 10 keV) of the other X-ray sources. The 1 keV temperature is typical of class II–III sources in quiescent, while some flares from class I–II sources have the 5 keV temperature and extremely high temperature of 10 keV is found in some giant flares; e.g., YLW16A = BF-64 (§6.1.5). Although all fittings are acceptable, the assumed temperature of 1 keV gives uncomfortably high luminosity of (4–7) $\times 10^{31}$ ergs s^{-1}, hence we discard the case of the 1 keV temperature. Table 6.6 shows the best-fit parameters, while the best-fit models (5 keV models for A-29 and A-31) are shown in Figure 6.20. For the quiescent phase of A-29 and A-31, we assume the same parameters as those of the flare. Since no significant X-ray is found in the quiescent phase for A-31, we estimate the 99.9 % upper limit of the X-ray luminosity (Table 6.6). The quiescent luminosities are 2–30 times lower than those in the flare phases.

Table 6.6: Spectral parameters of A-29, A-31, and BF-36

No.	Cts*	$< kT >$ (keV)	$< EM >$‡ (10^{52} cm^{-3})	$N_{\rm H}$‡ (10^{23} cm^{-2})	$< L_X >$(flare)‡§ (10^{29} ergs s^{-1})	$< L_X >$(quiescent)§ (10^{29} ergs s^{-1})
A-29†	21(5)	5	7.5(3.1–16)	2.5(1.3–4.7)	11	0.37
	···	10	5.0(2.1–10)	2.2(1.1–4.4)	8.1	0.27
A-31†	10(2)	5	5.0(0.53–110)	5.4(1.5–20)	6.9	<1.3
	···	10	2.9(0.35–82)	5.0(1.2–20)	4.9	<0.90
BF-36(flare)	24	7.6(>1.7)	3.1(1.6–20)	0.92(0.53–1.6)‖	5.1	···
BF-36(quiescent)	80	2.7(1.1–43)	2.7(0.75–21)	···	···	2.9

*X-ray counts in 2.0–9.0 keV during the flare phase. For A-29 and A-31, those during the quiescent phase are given in the parentheses.

†Spectral parameters are obtained with fixed temperatures of 5 and 10 keV (see text).

‡These parameters for A-29 and A-31 are derived from the flare spectra. Parentheses indicate the 90 % confidence limits.

§Absorption-corrected X-ray luminosity in 0.5–9.0 keV. $< L_X >$ in the quiescent phase for A-29 and A-31 is derived with the assumption of the same absorption as that in the flare phase.

‖Derived by the simultaneous fitting of the flare and quiescent spectra.

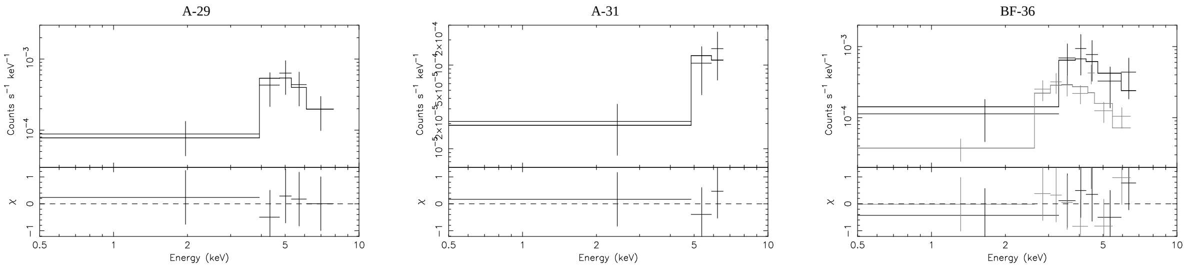

Fig. 6.20.— X-ray spectra of (left) A-29, (middle) A-31, and (right) BF-36. Black and gray lines indicate spectra of the flare and quiescent phases, respectively. The upper panels show the data points (crosses) and the best-fit MEKAL models (solid line). For A-29 and A-31, we show the best-fit models with the assumed 5 keV temperature. The lower panels are the data residuals from the model.

6.5.4 Possible origin of A-29, A-31, and BF-36

A-29

A-29 is found near the center of the 850 μm core SMM J16264$-$2424 with the separation angle of $\sim$11$''$. This is larger than the position accuracy of *Chandra* but is comparable to that of the beam size of the 850μm observation ($\sim$14$''$, SCUBA). Assuming a uniform density core, the column density of SMM J16264$-$2424 is estimated to be $\sim$10^{23} cm^{-2} from the radio flux (Johnstone et al., 2000), which is consistent with the X-ray-determined $N_{\rm H}$ of A-29 ($\sim$ 2$\times$10^{23} cm^{-2}) within large uncertainty for both the values. It is hence highly possible that A-29 is located in or behind SMM J16264$-$2424. Using the Log$N$–log$S$ relation by Mushotzky et al. (2000), we estimate the chance probability to detect a background AGN within the $\sim$11$''$ radius to be $\sim$5 %. Although this value is relatively large, A-29 shows a clear X-ray flare typical of low-mass stars but not seen in usual AGNs (Figure 6.19). No NIR counterpart of $K <$ 15 mag, the association with the sub-millimeter core SMM J16264$-$2424, and the large absorption lead us to conclude that the origin of A-29 is an embedded star younger than class I.

A-31

A-31 is located within $\sim$2$''$ from the center of the 3 mm clump KSHK-A (Kamazaki et al., 2001), the central source of millimeter/sub-millimeter clump SM1/SMM J16264$-$2423 (Johnstone et al., 2000). Taking into account of the physical size of KSHK-A ($\sim$4$''$) and position uncertainty of *Chandra* and the Nobeyama Millimeter Array interferometer observation ($\sim$5$''$), we can conclude that A-31 is surely associated with KSHK-A. The chance probability to detect a background AGN in the KSHK-A region is only ∼0.2 %. Furthermore, A-31 exhibits variable X-rays typical of low-mass YSOs. The column density of KSHK-A is $\sim 10^{24}$ cm^{-2} (Kamazaki et al., 2001), which is about twice of the X-ray determined $N_{\rm H}$ of A-31 ($\sim 5\times10^{23}$ cm^{-2}). Thus A-31 would be a YSO embedded near the center of the compact core KSHK-A. KSHK-A is spatially coincident with a 6 cm continuum source LFAM6 (Leous et al., 1991), which may be produced by a shock of outflow from a putative protostar (e.g., Rodriguez et al.1989, and references theirin). No NIR counterpart with $K < 15$ mag, its close location at the compact core center KSHK-A, the large absorption ($\sim 5\times10^{23}$ cm^{-2}), and the presence of the 6 cm enhancement indicate that A-31 is a strong candidate of X-ray emitting class 0.

A northwest part of the CO molecular outflow from the class 0 VLA1623 (designated as E–H in Yu, & Chernin 1997) is not aligned to the central part (B–D) but is slightly shifted to the north direction pointing to A-29 and A-31 (Figure 6.21). We speculate that the origin of the outflow E–H is A-29 or A-31 (not from VLA1623), although there is no CO emission at their closer vicinity (Kamazaki et al., 2001).

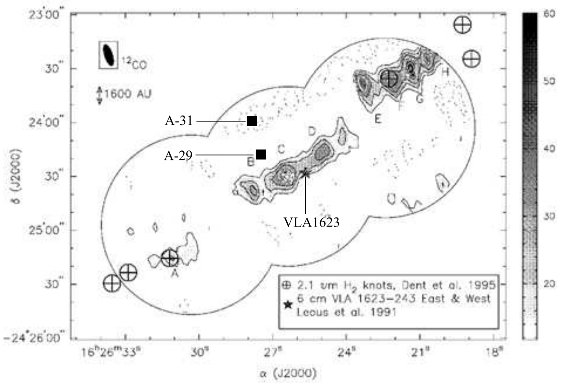

Fig. 6.21.— ^{12}CO (J=1–0) map around VLA1623 (Yu, & Chernin, 1997). Filled squares represent the positions of A-29 and A-31.

BF-36

BF-36 is located in the 850 μm clump SMM J16272−2430 with about 30″ separation from its center. It lies in an elongated 1.3 mm core chain with local peaks of B1-MM2, 3, and 4 (Motte et al., 1998). The source is about 30″ south of the peak of B1-MM4 (Figure 6.18). The chance probability of background AGN to be associated within 30″ radius from the core center is ∼20 %. However, BF-36 is among the brightest unidentified sources and is very unique which exhibits a clear flare. We therefore suggest that BF-36 is also a cloud member embedded near the dense core B1-MM4. Since millimeter/sub-millimeter peak fluxes of B1-MM4/SMM J16272−2430 are about ten times fainter than those harbor A-29 and A-31, although the clump size is comparable (6200 AU), the 2–6 times smaller $N_{\rm H}$ of BF-36 (9×10^{22} cm^{-2}) than those of A-29 and A-31 is consistent with the embedded star scenario.

Considering that $N_{\rm H}$ of BF-36 is rather typical of those of class I sources (see Figure 7.3), it is located at rather off-center position, and a class II source GY238 (BF-33) is closer to the center of SMM J16272−2430, BF-36 would be a more evolved star than the class 0 stage, possibly class I or II. Assuming the average ratio of $< L_X >/L_{\rm bol}$ to be $10^{-4.0}$ in the quiescent phase for YSOs (§7.4.2) and using $N_{\rm H}$ of 9×10^{22} cm^{-2}, $L_{\rm bol}$ and A_V of BF-36 are expected to be $\sim$0.8 $L_\odot$ and $\sim$60 mag (§7.4.1). These are above the current detection limit; some NIR-detected sources have nearly the same values (see Figure 7.1). One possibility of no NIR counterpart is that BF-36 is a YSO with very active X-rays. Assuming $< L_X >/L_{\rm bol}$ of $\approx10^{-3.5}$, we then expect $L_{\rm bol}$ of 0.08 $L_\odot$, which is below or near the current detection limit (Figure 7.1).

6.5.5 Ionization effect to circumstellar materials

The flare luminosity and duty ratio of A-29, A-31, BF-36 are $\sim10^{30}$ ergs s^{-1} and roughly one per 100 ks, respectively. Due to the large absorption, a significant fraction of X-ray energy is supplied into circumstellar materials. Using the parameters in Table 6.6, we estimate the X-ray ionization rate (ζ_X: Lorenzani & Palla 2001); the fraction of protons to be photo-ionized per unit time, which is defined as

$$\zeta_X = 1.7 \frac{< L_X > \tilde{\sigma}}{4\pi r^2 \Delta\epsilon} \frac{\int J_\nu e^{-n_{\rm H}\tilde{\sigma} r (\frac{\nu}{\nu_X})^{-n}} d\nu}{\int J_\nu d\nu} \ [{\rm s}^{-1}], \tag{6.3}$$

where $\sigma(E) = \tilde{\sigma}({\rm E/1keV})^{-n}$ is the total photoelectric cross section with $n = 2.51$ and $\tilde{\sigma} = 2.16\times10^{-22}$ cm^2, ΔE ($\equiv$ 35 eV) is the mean energy to make an ion-electron pair with cosmic abundance, $n_{\rm H}$ is the proton mass, J_ν is monochromatic X-ray flux (ergs s^{-1} Hz^{-1}), and r is the distance from the X-ray source. We assume $n_{\rm H}$ of A-31 and BF-36 to be 1.5×10^8 and 1.3×10^6 cm^{-3}, following Motte et al. (1998) and Kamazaki et al. (2001). Since $N_{\rm H}$ of A-29 is about a half of A-31, $\rm n_H$ is assumed to be 7.5×10^7 cm^{-3} for A-29. Then we obtain the "ionization radius", in which ζ_X exceeds that of cosmic rays, to be $\sim10^{2.5}$, $10^{2.4}$, and $10^{3.1}$ AU, respectively (Figure 6.22). These sizes are significantly smaller than the "parent" core size of typically $10^{3.8}$ AU, hence have no large impact in global structure. In a smaller scale of close vicinity of the YSOs (KSHK-A, for example), however, the X-ray ionization may still have significant effect on the circumstellar materials. Since the mass accretion is thought to be coupled to the magnetic field (Feigelson & Montmerle, 1999), our result may put significant influence on the growth of YSOs.

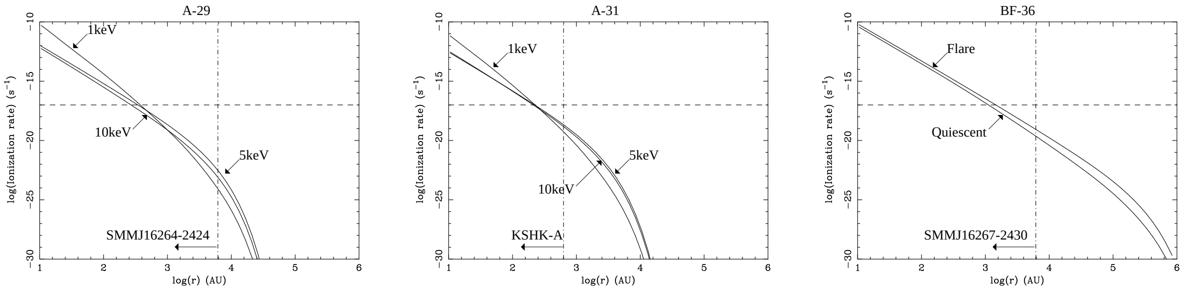

Fig. 6.22.— The relation between the X-ray ionization rate and the distance from the source for (left) A-29, (middle) A-31, and (right) BF-36. For A-29 and A-31, we represent three lines for the flare phase with the assumed temperatures (1, 5, and 10 keV). For BF-36, the flare and quiescent phases are separately estimated. Dashed and dash-dotted lines represent the ionization rate from cosmic rays and the core radii.

6.6 Unidentified Sources

6.6.1 Overall feature

In order to examine the average feature of unidentified sources, we co-add and make composite spectra, separately for total-band, soft-band, and hard-band sources (hereafter, we call them "total-band unidentified sources" and so on). We do not include A-29, A-31, BF-36, A-75 = BF-11, BF-92, BF-S7, and BF-H3 because they have different nature from the other unidentified sources. A-H2 is also excluded because of severe contamination from A-2 (DoAr21). Figure 6.23 shows the composite spectra. First we fit them by the MEKAL model. However, uncomfortably high temperature (> 20 keV) is obtained for the total- and hard-band unidentified sources. We hence re-fit them by a power-law model and find acceptable fits. Figure 6.23 (solid lines) and Table 6.7 show the best-fit models and parameters, respectively.

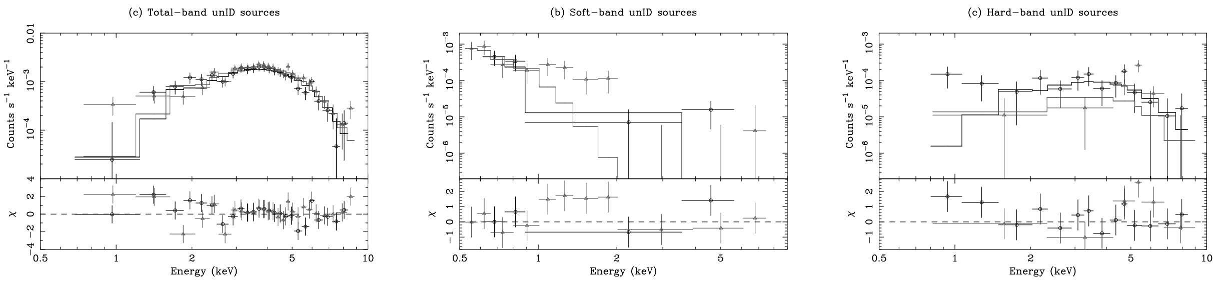

Fig. 6.23.— Composite spectra of (a) total-band, (b) soft-band, and (c) hard-band unidentified sources. The upper panels show data points (crosses) and the best-fit non-thermal (a and c) and thermal (b) model (solid line), while the lower panels are the data residuals from the best-fit model. Circles and triangles represent the data for obs-A and obs-BF, respectively.

The best-fit photon index (∼1.5) of the total-band unidentified sources is similar to that of the canonical value of active galactic nuclei (AGNs: ∼1.7), while the best-fit $N_{\rm H}$ of 5.3×10^{22} cm^{-2} is nearly equal to the average value through this cloud (Tachihara et al., 2000). Inversely, if the background sources have a mean photon index of 1.5 and are absorbed by the cloud gas of $N_{\rm H} = 5.3\times10^{22}$ cm^{-2}, the $\log N - \log S$ relation by Mushotzky et al. (2000) predicts the detectable source numbers to be several tens, which is consistent with the total number of unidentified sources (∼80). Also, the spatial distribution of the total-band unidentified sources seems to be anti-correlated with the molecular cloud (Figure 6.24). Most of the total-band unidentified sources therefore are likely to be background AGNs, as well as the radio bright unidentified source A-75/BF-11 = LFAM21 (§6.6.3).

The average temperature of the soft-band unidentified sources is ~0.2 keV, which is significantly lower than those of YSOs, although the data excess around 1–2 keV (Figure 6.23a) indicates the existence of higher temperature component of $< kT > = 1$–2 keV. Considering the low temperature plasma and small absorption column ($\sim 2{\times}10^{21}$ cm^{-2}), one plausible idea is coronal emission of MS stars in front of the ρ Oph cloud. However, it would be less possible because there is no optical counterpart (Chini, 1981). Another idea is that an outflow from YSOs in ρ Oph collides at a dense interstellar matter and makes a low temperature (0.1–0.5 keV) plasma, like X-ray emission from Herbig-Haro objects (HHs: Pravdo et al., 2001; Favata et al., 2002). In particular, A-S1 is located in the direction of CO outflow from the class 0 source VLA1623 (Figure 6.25), hence is a strong candidate of jet-induced X-rays. The average flux (absorption-corrected) per one source of $1.4{\times}10^{-15}$ ergs s^{-1} cm^{-2} is converted to $< L_X >$ of $3.5{\times}10^{27}$ ergs s^{-1} assuming the distance of 145 pc, which is about 100 times lower than those of HHs ($\sim 10^{29}$ ergs s^{-1}). This indicates that the emitting region of soft-band unidentified sources has smaller volume and/or density than that of HHs.

The hard-band unidentified sources show nearly the same spectral parameters as the total-band sources, although the average flux is about four times lower, hence are also thought to be background AGNs.

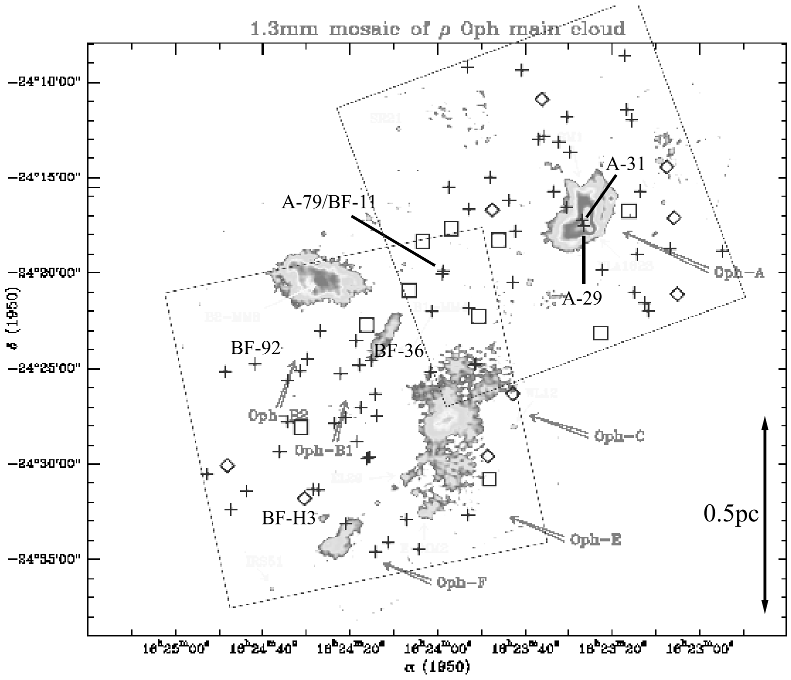

Fig. 6.24.— Spatial distribution of unidentified sources overlaid on the 1.3 mm continuum map (Motte et al., 1998). Crosses, squares, and diamonds represent total-band, soft-band, and hard-band unidentified sources, respectively.

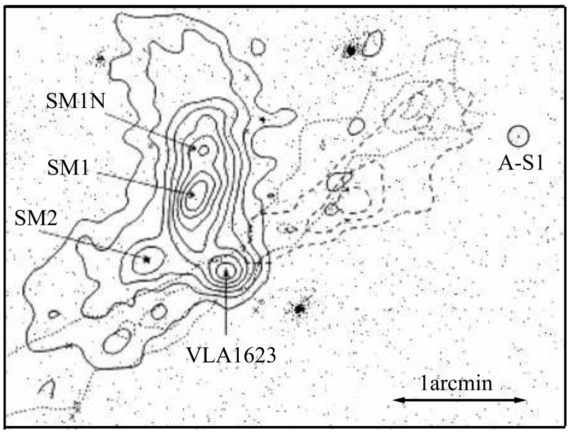

Fig. 6.25.— ACIS image around the ρ Oph core A region in 0.5–2.0 keV. Solid, dotted, and dashed contours show 1.3 mm radio continuum, blueshifted and redshifted CO (2–1) intensities, respectively (André et al., 1993). Arrows indicate the positions of the class 0 source VLA1623 and mm cores (SM1, SM1N, and SM2). The position of A-S1 is shown by the circle.

Table 6.7: Best-fit parameters of the composite spectra of unidentified sources

Class*	$N^{\dagger}$	$< kT >/\Gamma^{\ddagger\S}$ (keV/–)	$N_{\rm H}^{\S}$ (10^{22} cm^{-2})	Flux$^{\parallel}$ (10^{-15} ergs s^{-1} cm^{-2})	Flux$_c^{\#}$
Total	60	1.5(1.1–1.7)	5.3(4.2–6.6)	441.7(7.4)	905.3(15.1)
Soft	10	0.16(0.042–0.26)	0.20(<0.59)	3.5(0.35)	14.4(1.4)
Hard**	7	<2.2	4.0(2.0–10)	14.8(2.1)	27.8(4.0)

*See text.
†The total number of sources added in the spectra.
‡Best-fit temperature for soft-band unidentified sources and photon index for the others.
§Parentheses indicate the 90 % confidence limit.
‖Observed flux in 0.5–9.0 keV. Parentheses indicate the average value per one source.
#Absorption-corrected flux in 0.5–9.0 keV. Parentheses indicate the average value per one source.
**The best-fit value of Γ is not determined, hence we assume $\Gamma = 1.5$ (best-fit value for the total-band unidentified source) for the estimation of the other parameters.

6.6.2 A-48

The shape of this unidentified source seems to be diffuse with a radius of $\sim 5''\cong 10^3$ AU (Figure 6.26), which is significantly larger than the default PSF size ($\sim 1\farcs3$), although we can not reject the possibility that A-48 is a possible false source. We also note that a BD $_c$ GY84 is located at the edge of the diffuse emission. We previously reported significant X-ray emission from GY84 (Imanishi et al., 2001b), which may be part of the diffuse emission, although any relation between GY84 and A-48 would be conceivable.

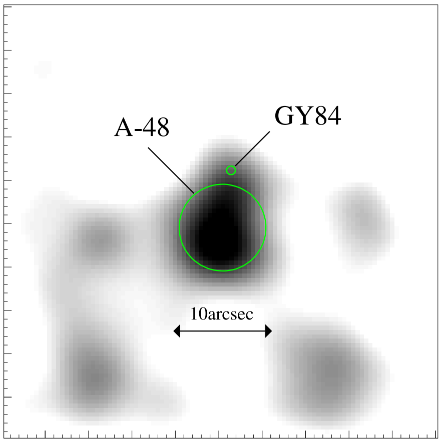

Fig. 6.26.— ACIS image around A-48 in 0.5–9.0 keV smoothed with a Gaussian of $\sigma = 6$ pixels. Large and small circles represent the position of A-48 and a BD_c GY84, respectively.

6.6.3 A-75/BF-11 – LFAM21

A-75 = BF-11 has no NIR counterpart but is spatially identified with the radio-bright source LFAM21, a candidate of a compact extragalactic AGN (Stine et al., 1988). Both X-ray spectra of LFAM21 seem to be non-thermal typical of AGNs and show line-like structure at $\sim$5 keV (Figure 6.27). We hence fit them by a (power-law + gaussian) model assuming the same absorption. The best-fit models and parameters are shown in Figure 6.27 and Table 6.8. The best-fit photon index of 1.2–1.4 and $N_{\rm H}$ of $\sim 6\times10^{22}$ cm^{-2} are reasonable to consider that the typical AGN spectrum is absorbed at the ρ Oph cloud (Tachihara et al., 2000). The line center energy is 4.8–5.0 keV. If this is a redshifted neutral iron (6.4 keV) frequently seen in the AGN spectra (Awaki et al., 1991), a redshift (z) of LFAM21 is estimated to be $\sim$ 0.3.

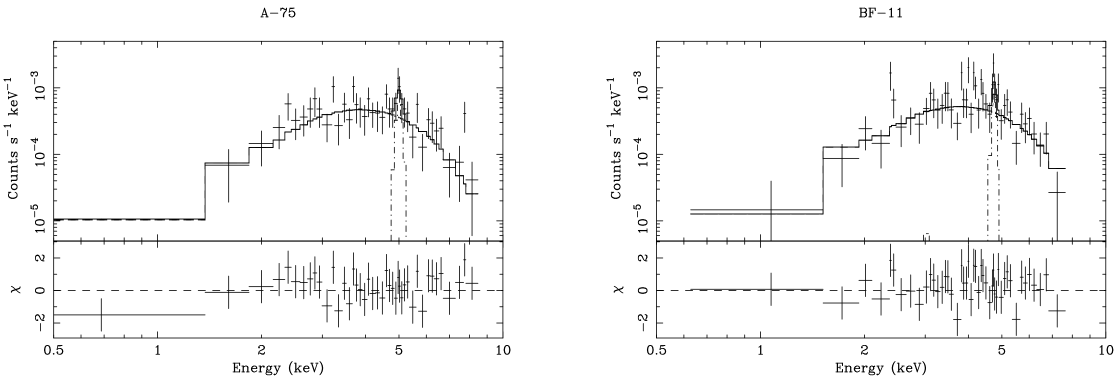

Fig. 6.27.— X-ray spectra of LFAM21 in obs-A (A-75, left) and obs-BF (BF-11, right). The upper panel shows data points (crosses) and the best-fit (power-law + gaussian) model (solid and dashed lines), while the lower panel shows residuals from the best-fit model.

Table 6.8: Best-fit parameters of LFAM21

No.	Γ^*	$N_{\rm H}{}^*$ (10^{22} cm^{-2})	$E_{\rm gauss}{}^{*\dagger}$ (keV)	$EW^{*\ddagger}$ (eV)	Flux§ (10^{-14} ergs s^{-1} cm^{-2})	Flux$_c{}^\S$
A-75	1.2(1.1–1.5)	5.9(5.2–7.0)	5.0(4.9–5.7)	380(130–640)	6.4	11.5
BF-11	1.4(1.1–1.8)	5.9$^\|$	4.8(4.7–4.8)	290(120–510)	7.3	14.1

*Parentheses indicate the 90 % confidence limit.

†The gaussian center energy.

‡Equivalent width for the gaussian line.

§Observed and absorption-corrected fluxes in 0.5–9.0 keV.

$^\|$Derived by the simultaneous fitting of the spectra of A-75 and BF-11.

6.6.4 BF-92

An unidentified source BF-92 shows a weak flare (Figure A.4) similar to the new YSO candidates (A-29 and BF-36; §6.5). Although there is neither mm core nor cm emission at the position of BF-92, Grosso et al. (2001) detected jet-like H_2 emission 20–40″ away from BF-92 as shown in Figure 6.28. They concluded that the origin of the jet is the class I source YLW15A (BF-61) located ∼9′ away from the H_2 jet, however we infer that the origin may be BF-92, a new YSO (probably class 0–I protostar) having violent jet activity. The flare light curve and highly absorbed spectrum ($N_{\rm H}$ ∼6×10^{22} cm^{-2}) also indicate the YSO nature of BF-92. Followup deep NIR and radio observations would be fruitful.

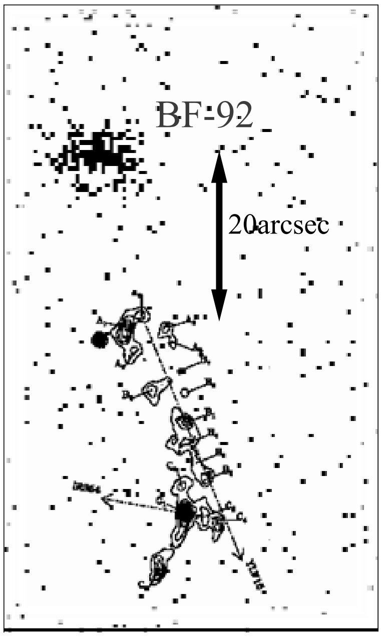

Fig. 6.28.— ACIS image around BF-92 overlaid on the H_2 contour map (Grosso et al., 2001).

6.6.5 BF-S7

A soft-band source BF-S7 is located near a class I CRBR85, although the offset (3.″7) is significantly large considering its off-axis angle (6.′9). Also, the detection only in the soft band is inconsistent with the X-ray emission from class I, because class I sources generally suffer large absorption (§7.3) and consequently are hard to see at the soft band. One possible scenario is that an outflow from the central source collides at dense circumstellar envelope and makes low temperature (0.1–0.5 keV) plasma, like X-ray emission from Herbig-Haro objects (HHs:

Pravdo et al. 2001; Favata et al. 2002; see also Figure 2.9). Although CRBR85 has shown no evidence for outflow activity, bipolar nebulosity was detected, indicating the existence of an edge-on circumstellar disk (Brandner et al., 2000). We therefore suspect that jet-induced X-rays with a large offset from the central source are possible because of the large inclination angle.

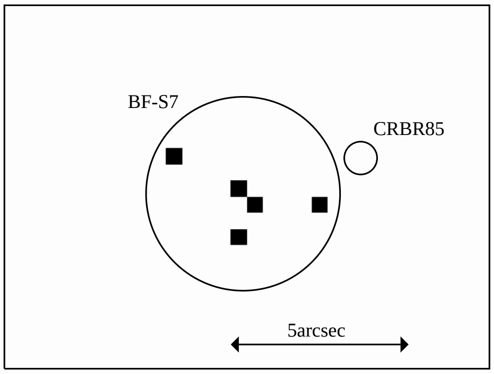

Fig. 6.29.— Close-up ACIS image around BF-S7 and CRBR85. Circles represent the position of BF-S7 and CRBR85. Filled squares correspond to one X-ray photon.

6.6.6 BF-H3

A hard-band source BF-H3 has no NIR counterpart, but is associated with an optical [S_{II}] source A2, a candidate of HH (Gómez et al., 1998). Hence BF-H3 may be the third sample of X-ray emitting HHs following HH2 (Pravdo et al., 2001) and L1551 IRS5 (Favata et al., 2002), although there is no other evidence for its HH nature and for the origin of A2. Interestingly, BF-H3 shows X-ray emission only in the hard band (2.0–9.0 keV), hence would have much higher temperature plasma ($\gtrsim$2 keV) than that of L1551 IRS5 and HH2 (0.1–0.5 keV). This indicates high-velocity outflow activity, which is the similar case to GY91 (§6.1.1).

Chapter 7

Overall Feature of X-ray Emission from YSOs

7.1 X-ray Detection Rate

We detected 195 X-ray sources from the ~1 pc × 2 pc region of the ρ Oph main body. About 60% (110) of them are identified with NIR sources. Table 7.1 summarizes the number of X-ray sources and detection rate for each class. High detection rate ($\geq$ 50%) is obtained for class I sources as well as class II and III sources, while that is slightly lower for class III$_c$, BD, and BD$_c$ sources ($<$ 40%). Figure 7.1 shows the relation between the bolometric luminosity ($L_{\rm bol}$) and visual extinction (A_V) for the ρ Oph sources (Table B.1). We see the tendency that most sources with no X-ray detection (gray symbols in Figure 7.1) are distributed at the upper-left area in this figure, i.e., having relatively lower $L_{\rm bol}$ and higher A_V. Considering the almost constant $< L_X >/L_{\rm bol}$ and $N_{\rm H}/A_V$ correlations (§7.4.1 and §7.4.2), this means that the X-ray non-detected sources have lower $< L_X >$ and higher $N_{\rm H}$ even if they emit X-rays. It hence would be conceivable that the X-ray non-detected sources may emit X-rays below the current sensitivity limit of *Chandra*. Lower detection rate of class III$_c$, BD, and BD$_c$ sources is simply due to lower $L_{\rm bol}$ ($\cong$ lower $< L_X >$) of these classes. On the other hand, X-ray non-detected class I sources have relatively high $L_{\rm bol}$ with moderate A_V (e.g., GSS30, G304, and GY378; Figure 7.1). However, this could be partly due to short time variability. For example, WL21 (BF-8) and GY256 (BF-51) are hardly visible except when they exhibit X-ray flares (see Figure A.1). Also long-term variability, like the 11-year cycle of the solar X-ray activity, may exist. We therefore expect that virtually all YSOs, at least in ρ Oph, are potential X-ray emitters regardless of their classes.

Table 7.1: The number of X-ray sources and detection rate for each class

Class	Source*	X-ray†	Ratio‡
I	15	8	53 %
II	70	58	83 %
III	17	17	100 %
III$_c$	27	9	33 %
Unclassified NIR	···	12	···
BD&BD$_c$	15	5	33 %
F	3	1	33 %
unidentified	···	85	···

*The number of sources within the ACIS field of view.
†The number of X-ray detected sources.
‡The X-ray detection rate.

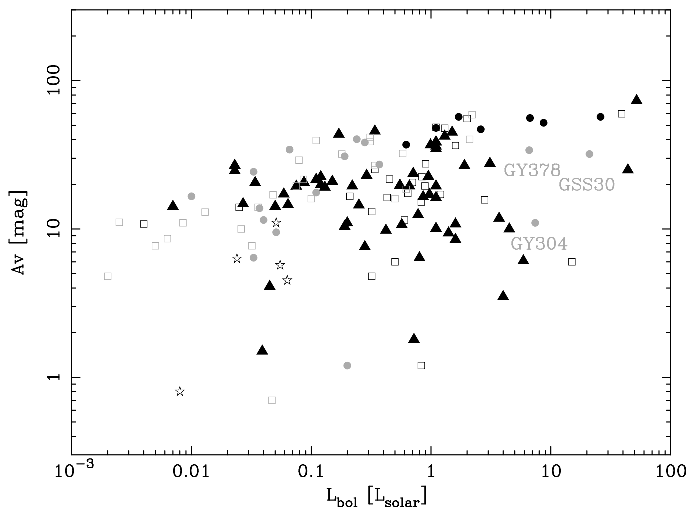

Fig. 7.1.— Relation between the bolometric luminosity ($L_{\rm bol}$) and visual extinction (A_V: Bontemps et al., 2001, see also TableB.1). Circles, triangles, squares, and stars represent class I, class II, class III+III$_c$, and BD/BD$_c$ sources, respectively. Gray symbols are sources with no X-ray detection. Three X-ray non-detected class I sources with relatively high $L_{\rm bol}$ are also indicated (GSS30, GY304, and GY378).

7.2 Luminosity Function

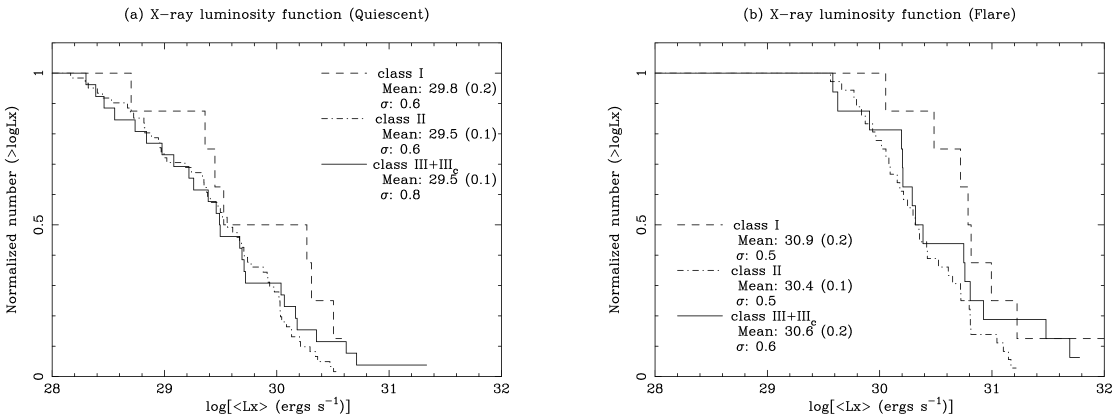

Fig. 7.2.— Normalized X-ray luminosity functions of class I (dashed), class II (dash-dotted), and class III (solid) sources in the (a) quiescent and (b) flare phases. The mean value (Mean) and standard deviation (σ) of log[$< L_X >$] in the unit of ergs s^{-1} for each class are shown in the figures. Parentheses indicate errors of the mean values.

We calculate the X-ray luminosity function for the detected X-ray sources of class I, II, and III+III$_c$ (Figure 7.2), using the ASURV statistical software package (rev.1.2) [1] based on the maximum likelihood Kaplan-Meier estimator in order to examine the differences along the evolutional stages. The luminosity function of class I seems to be shifted toward the higher values than those of class II and III+III$_c$ both in the quiescent and flare phases.

To be more quantitative, we estimate the significance level using two nonparametric two-sample tests in ASURV; the Gehan's generalized Wilcoxon test (GW) and the logrank test (Feigelson & Nelson, 1985). The results are given in Table 7.2, where blank (...) indicates that the significance level is less than 90 %. From Table 7.2, we see that both the GW and logrank tests for the $< L_X >$ difference between class I and the others in the flares show the marginal significance level of ∼94 %. We further should note that the effect of "undetected" faint flares of class I can not be ignored; if we assume an undetected class I has $< L_X >$ smaller than 10^{30} ergs s^{-1} which is near the detection threshold of a class I flare, and add this source to the GW and logrank test sample, then the relevant significance level is largely reduced to < 90 %. We hence conclude that the higher $< L_X >$ of class I than class II+III during flares is marginal.

On the other hand, from Table 7.2, we see no significant difference between class II and III+III$_c$ source in the flare phase. This is contrary to the results of the Taurus-Auriga-Perseus

[1] see http://www.astro.psu.edu/statcodes.

samples (Stelzer et al., 2000), for which there was a significant difference between the distribution of flare $< L_X >$ of class II (CTTS) and class III+III$_c$ (WTTS) sources.

Also, we see no significant difference of $< L_X >$ in the quiescent phase among all the classes. This is consistent with the previous estimation for this region with *ROSAT* derived by Grosso et al. (2000). They tried to estimate the significances rather strictly by considering the upper limit of undetected sources. Our samples give more severe constraint because the detection threshold is largely reduced to give the mean luminosities of $10^{29.5}$–$10^{29.8}$ ergs s^{-1}, which is about 10 times lower than that of *ROSAT*.

7.3 Distribution of X-ray Parameters

In Figures 7.3–7.5, histograms of $N_{\rm H}$, $< kT >$, τ_r, and τ_d are shown for each class separately, together with the mean values and standard deviations. We exclude the samples whose best-fit parameters and/or those errors are not determined due to the limited statistics. For sources with multi-temperature plasma (BF-46 and BF-96), we regard $< kT >$ of the soft and hard components as the quiescent and flare values, respectively, following the discussion that the former would be steady coronal emission while the latter is flare activity (§6.2). Like the case of L_X, we estimate the significance level for the differences of these parameters among all the classes with two nonparametric two-sample tests in ASURV. The results are also given in Table 7.2.

Absorption ($N_{\rm H}$)

$N_{\rm H}$ is distributed from $10^{21.5}$ to $10^{23.5}$ cm^{-2} (Figure 7.3). The mean value of $N_{\rm H} \sim 10^{22.5}$ cm^{-2} is roughly consistent with the average value through this cloud derived by the C^{18}O radio observations (Tachihara et al., 2000). Also, the distribution of $N_{\rm H}$ of class I sources is larger than that of the others. Using ASURV, we estimate that the significance level of this tendency is rather high of $\gtrsim$97 %. This supports the idea that X-rays from class I sources come near the central source deeply embedded in denser envelopes and suffer larger intrinsic absorption.

Plasma temperature ($< kT >$)

Most of the $< kT >$ values in the quiescent phase are in the range of 0.2–5 keV, while it becomes systematically higher (1–10 keV) in the flare phase, indicating the plasma heating during the flare. Although the flare temperature of all classes is distributed around 3–4 keV, some flares of class I and II sources show higher temperature than 5 keV, while all flares of class III+III$_c$ sources have $< kT >$ less than 5 keV. The mean values of $< kT >$ during flares for class I and II (4–5 keV) is therefore larger than that of class III+III$_c$ (2.7 keV).

From Table 7.2, we see that both the GW and logrank tests for the difference of $< kT >$

during flares between class I+II and class III+III$_c$ sources show high significance level of 94 % and 98 %. One may concern that systematically large absorption of class I and II sources makes artificial spectral hardening of these classes. We however argue that the observed tendency of higher $< kT >$ during flares for younger sources is not changed by the extinction differences with the following reasons;
(1) If the intrinsic distribution of the flare $< kT >$ in class III+III$_c$ is the same as classes I and II, some of the class III+III$_c$ flares should show higher $< kT >$ than 5 keV, but there is no such flare in class III+III$_c$.
(2) We re-estimate the mean $< kT >$ of class I+II and class III+III$_c$ during the flare for the limited sources of $N_{\rm H} \leq 5{\times}10^{22}$ cm^{-2} (most of class III+III$_c$ sources have lower $N_{\rm H}$ than this value). Although the mean $N_{\rm H}$ is nearly the same (2.5$\pm$0.2 and 2.2$\pm$0.3 $\times$ 10^{22} cm^{-2} for class I+II and class III+III$_c$), the mean $< kT >$ is still higher for class I+II (3.7$\pm$0.4 keV) than for class III+III$_c$ (2.4$\pm$0.3 keV).

In the quiescent phase, on the other hand, ASURV shows the significance level of >95% for the tendency of higher $< kT >$ of class I than the others (Table 7.2). However, we suspect this may be a bias effect because the quiescent temperatures are systematically low ($\lesssim$ 5 keV), hence would be significantly affected by the absorption compared with the flare temperatures.

Flare timescales (τ_r and τ_d)

The rise and decay timescales of the flares (τ_r and τ_d) are distributed around $10^{3.5}$ s and 10^4 s, respectively. Although the mean value of τ_r indicates that younger sources have shorter rise timescale, the difference of τ_r among these classes is not statistically significant (<90 %, Table 7.2). The larger mean values for class III+III$_c$ sources are primarily due to the flares with unusually long timescales of $\gtrsim$50 ks (A-2, A-63, and BF-96); such flares are not seen in class I and II sources ($\approx$30 ks at the maximum). Since we can not reject the possibility that these long timescales are simply because of the composition of unresolved two (or more) flares, we further estimate the mean τ_r and τ_d values of class III+III$_c$ sources without these flares to be 3.1$\pm$0.6 and 6.9$\pm$0.8 ks, which is comparable to those of the other classes.

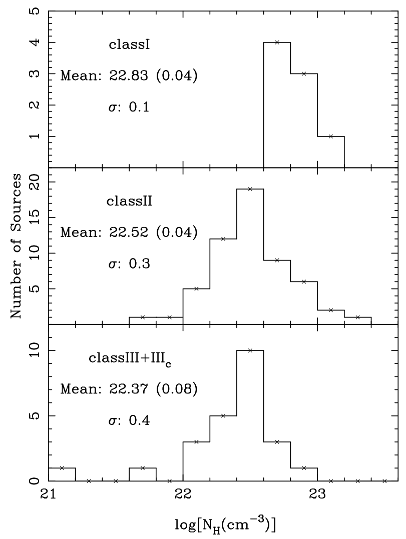

Fig. 7.3.— The histogram of $\log(N_{\rm H})$ for each class, with their mean values (Mean) and standard deviation (σ). Parentheses indicate errors of the mean values.

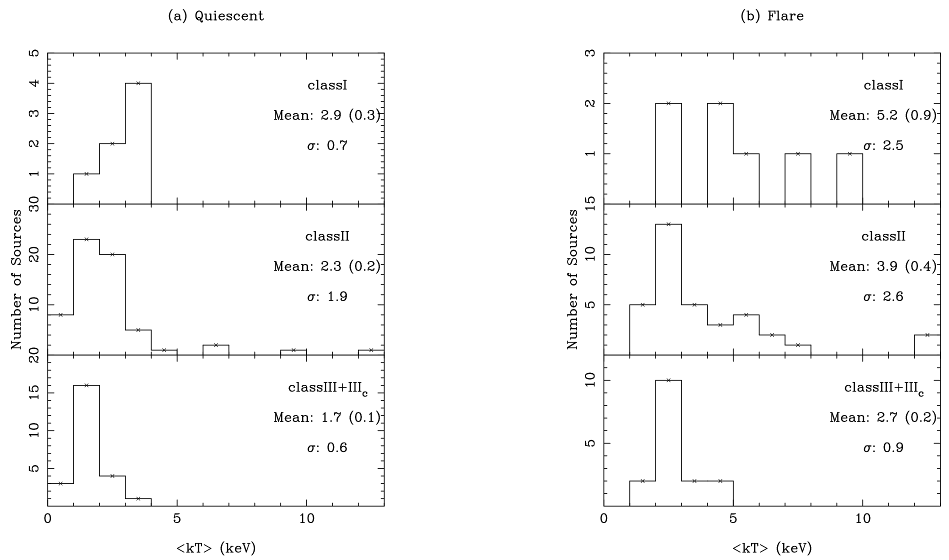

Fig. 7.4.— Same as Figure 7.3, but for $< kT >$ in the (a) quiescent and (b) flare phases for each class, with their mean values (Mean) and standard deviation (σ) in the unit of keV for each class. Parentheses indicate errors of the mean values.

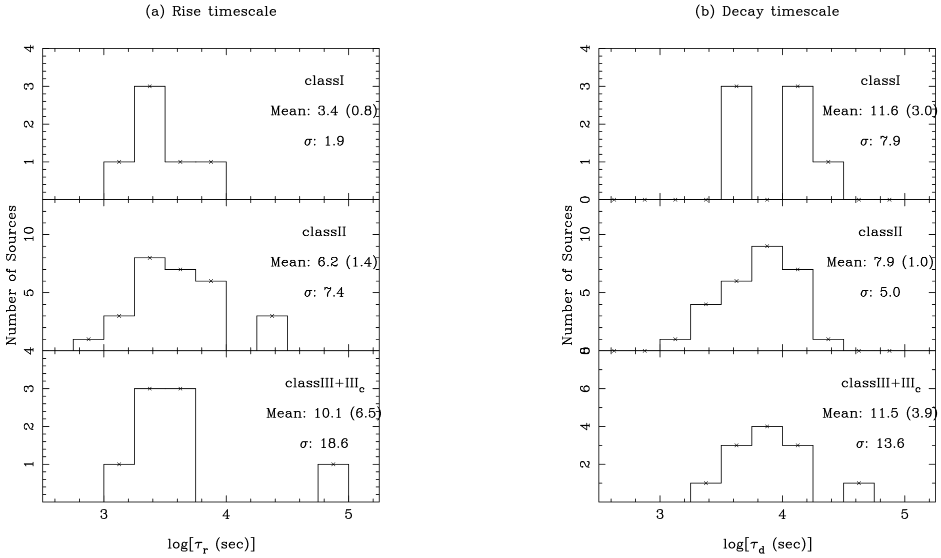

Fig. 7.5.— Same as Figure 7.3, but for flare rise and decay timescales (τ_r and τ_d), with their mean values (Mean) and standard deviation (σ) in the unit of ks. Parentheses indicate errors of the mean values.

Table 7.2: Results of two-sample tests for the differences of the observed parameters among classes

Parameter	— Sample size* —			— Probability for the null hypothesis† —					
	I	II	III+III$_c$	I vs II+III+III$_c$		I+II vs III+III$_c$		II vs III+III$_c$	
				GW	logrank	GW	logrank	GW	logrank
logL_X (Flare)	8	36	16	0.059	0.063	...	...	...	...
logL_X (Quiescent)	8	61	26	...	...	...	...	...	...
log$N_{\rm H}$	8	56	24	0.005	0.028	0.031	0.015	...	0.086
$< kT >$ (Flare)	7	35	16	0.079	...	0.060	0.017	...	0.047
$< kT >$ (Quiescent)	7	61	24	0.008	0.022	0.046	0.037	...	0.026
τ_r	6	28	8	...	...	...	...	...	...
τ_d	7	28	12	...	...	...	...	...	...

*The number of data points used for the two-sample tests.

†Probability that the hypothesis of two distributions being the same is true, which is derived with the Gehan's generalized Wilcoxon test (GW) and the logrank test (Feigelson & Nelson, 1985). Blank (...) indicates that the probability is larger than 0.1.

7.4 Correlation between X-ray and Other Physical Parameters

7.4.1 $N_{\rm H}$ vs A_V

The relation between the X-ray and visual extinction ($N_{\rm H}$ and A_V) is a key to understand the gas-to-dust ratio of the interstellar medium, since X-ray and optical–IR photons are mainly absorbed and scattered by interstellar gas and dust, respectively. We find a good log-linear correlation as shown in Figure 7.6. The best-fit linear model (dashed line) is

$$(\frac{N_{\rm H}}{10^{21}{\rm cm}^{-2}}) = (1.38 \pm 0.03)(\frac{A_V}{\rm mag}). \tag{7.1}$$

The $N_{\rm H}/A_V$ ratio of 1.38 is roughly consistent with that of other star-forming clouds; OMC 2/3 (1.49: Tsujimoto et al., 2001) and Mon R2 (1.32: Kohno, Koyama, & Hamaguchi, 2002), but slightly lower than that in the average interstellar space of our Galaxy (1.79: Predehl & Schmitt, 1995). This indicates that the gas-to-dust ratio is lower in star-forming clouds than that in the interstellar medium.

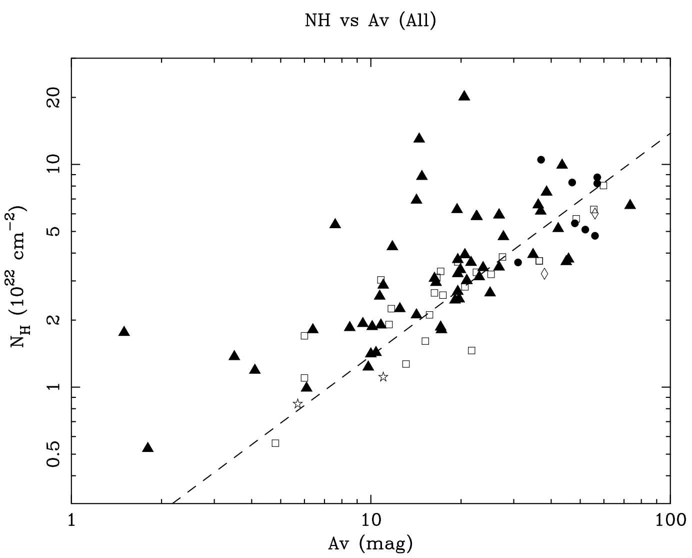

Fig. 7.6.— Relation between the absorption column ($N_{\rm H}$) and visual extinction (A_V: Bontemps et al., 2001, see also TableB.1). Circles, triangles, squares, diamonds, and stars represent class I, class II, class III+III$_c$, unclassified NIR, and BD/BD$_c$ sources, respectively. The dashed line shows the best-fit linear model (see text).

7.4.2 $< L_X >$ vs $L_{\rm bol}$

The ratio of the X-ray ($< L_X >$) and bolometric ($L_{\rm bol}$) luminosities is often used to estimate relative activity level of X-ray emission of various classes. We show the relation of $< L_X >$ and $L_{\rm bol}$ for the ρ Oph X-ray sources with NIR counterpart in Figure 7.7. In the quiescent phase, most sources have $< L_X > /L_{\rm bol}$ of 10^{-5}–10^{-3}, which is comparable to those for other star-forming clouds (Feigelson et al., 2002; Preibisch & Zinnecker, 2002) and is significantly larger than that for the quiet sun ($\sim 5\times10^{-7}$: Vaiana & Rosner, 1978). $< L_X >/L_{\rm bol}$ for the flare X-rays is also large and some flares exceed the saturation level of coronally active stars ($< L_X >/L_{\rm bol} = 10^{-3}$: Fleming et al., 1995). These results directly indicate that YSOs have much higher X-ray activity level than MSs. On the other hand, the magnetic B star S1 (= A-41) shows much lower $< L_X > /L_{\rm bol}$ value of $\sim 10^{-6}$ than, but almost comparable $< L_X >$ of $\sim 10^{29}$ ergs s^{-1} to the other (low-mass) YSOs. This is consistent with the *ASCA* results for intermediate-mass YSOs (Herbig Ae/Be stars: Hamaguchi, 2001), hence suggests that the X-ray emission mechanism for intermediate-mass YSOs is nearly the same as that of low-mass YSOs, although the relative X-ray activity level normalized by the total stellar emission is significantly low. It is also conceivable that S1 shows peculiar spectral features, indicating possible non-thermal emission (see §6.3.5).

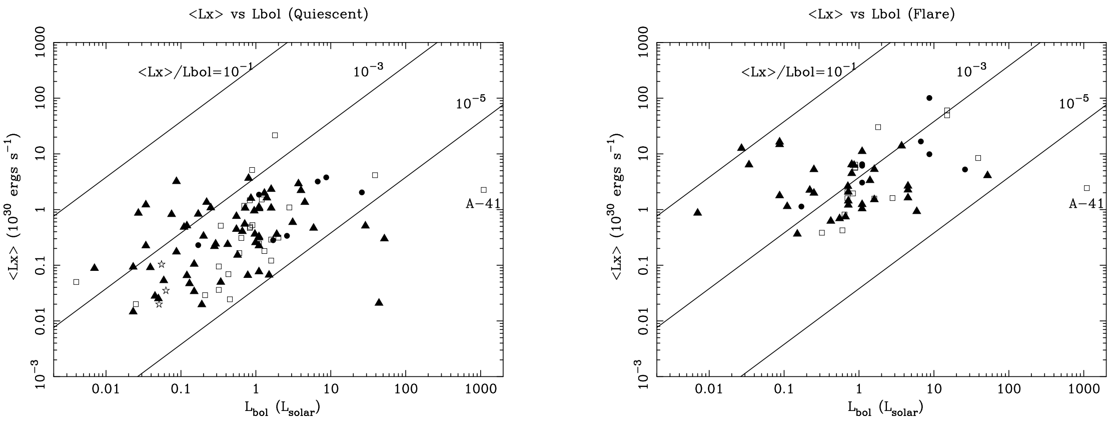

Fig. 7.7.— Relation between the bolometric ($L_{\rm bol}$) and X-ray ($< L_X >$) luminosities for the (left) quiescent and (right) flare phases. Symbols are the same as Figure 7.6. Solid lines represent the relations of $< L_X >/L_{\rm bol} = 10^{-1}$, 10^{-3}, and 10^{-5}. The position of the magnetic B star S1 (= A-41) is indicated in the figure.

7.4.3 $< L_X >$ vs Mass

Figure 7.8 shows the relation between $< L_X >$ and their stellar mass (M). Within the range of $M < 2M_\odot$, $< L_X >$ seems to be roughly proportional to M, which is the same as another star-forming region IC348 ($< L_X > \propto M^2$: Preibisch & Zinnecker, 2002). Since the stellar mass is roughly as a function of $L_{\rm bol}$ (Figure 2.1), this is basically the same as the constant $< L_X > /L_{\rm bol}$ relation (§7.4.2).

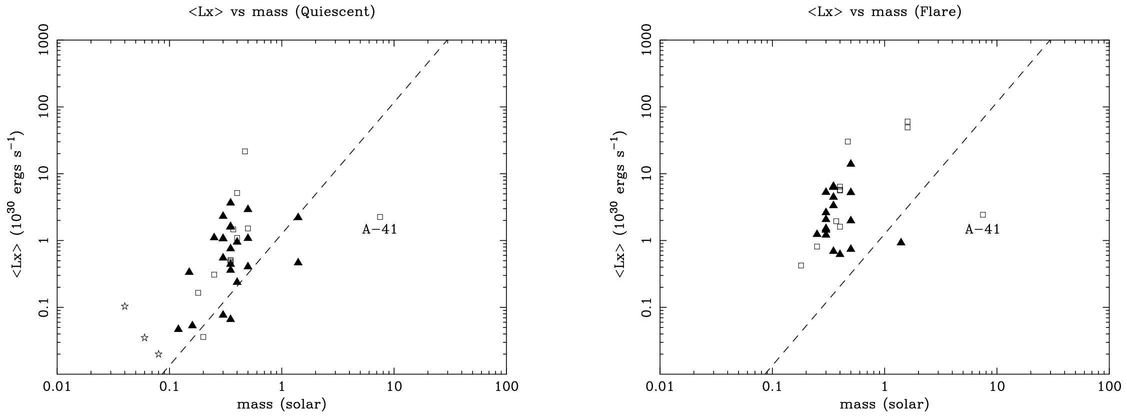

Fig. 7.8.— Relation between the stellar mass and X-ray luminosity ($< L_X >$) for (left) quiescent and (right) flare phases. Symbols are the same as Figure 7.6. Dashed lines are the $< L_X >$–mass relation derived for X-ray sources in IC 348 (Preibisch & Zinnecker, 2002). The position of the magnetic B star S1 (= A-41) is indicated in the figure.

7.4.4 $< L_X >$ vs L_R

Figure 7.9 shows the relation between $< L_X >$ and monochromatic radio luminosity at 1.5 GHz (L_R ergs s^{-1} Hz^{-1}) for sources detected at this wavelengths (André et al., 1987; Stine et al., 1988; Leous et al., 1991, see column 3 in Table 5.3). Possible log-linear correlation can be seen for both the quiescent and flare X-rays except for A-75/BF-11; most sources have log($< L_X > /L_R$) of 13.5–15.5, which is almost comparable to those of MS stars (Güdel & Benz, 1993). Although it is not clear that cm emission of the ρ Oph sources is thermal or non-thermal, the $< L_X >$ vs L_R relation indicates that the majority of its origin is basically the same as that of X-rays. One plausible idea is that accelerated non-thermal electrons (see §2.3.1) emit synchrotron radio continuum, then heat ambient matter which gives rise to the thermal X-ray flux. We also note that the background AGN candidate LFAM21 (A-75 = BF-11, §6.6.3) has much lower log($< L_X > /L_R$) of $\sim$11 than the others. This is the typical value of AGNs (Smith et al., 1999), hence further supports its AGN nature. On the other hand, other unidentified sources detected at the cm wavelengths (A-4, A-31, A-37, and BF-37[2]) have large $< L_X > /L_R$ comparable to YSOs and MSs. We therefore expect that these are possible candidates of new YSOs, as already proposed for A-31 (§6.5).

[2]BF-37 is not plotted in Figure 7.9 because we can not determine $< L_X >$ due to the limited statistics. However, BF-37 = LFAM32 has relatively small L_R of $\sim 1.5\times10^{14}$ ergs s^{-1} Hz^{-1}, hence would be in this class.

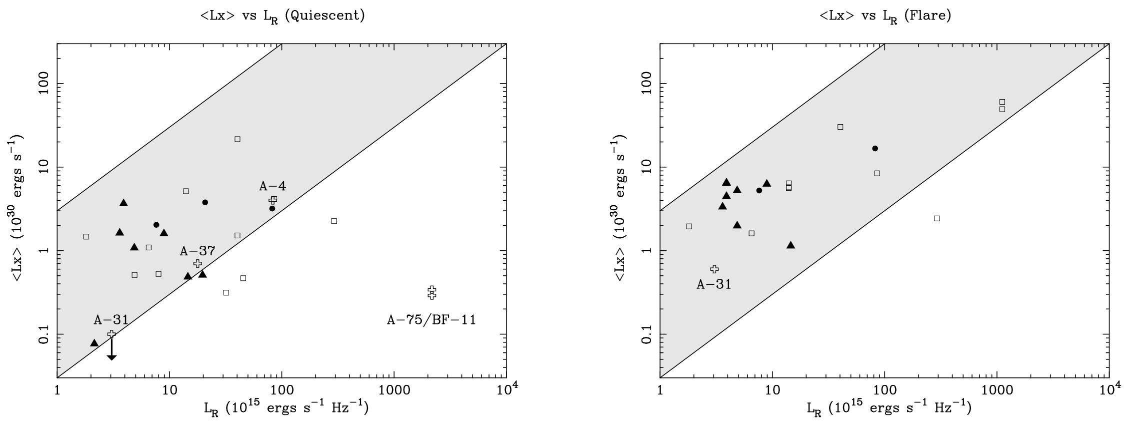

Fig. 7.9.— Relation between the radio (L_R) and X-ray ($< L_X >$) luminosities for the (left) quiescent and (right) flare phases. Symbols are the same as Figure 7.6. A shaded region represents the approximate position of MS stars (Güdel & Benz, 1993). Four unidentified sources detected at the cm wavelengths are also indicated (A-4, A-31, A-37, and A-75 = BF-11, see also §6.5 and §6.6.3).

Chapter 8

Systematic Study of YSO Flares

We detected 71 X-ray flares from the ρ Oph X-ray sources. Using this enormous sample, we make a systematic study on flare activity of low-mass YSOs in this chapter.

8.1 Flare Rate

Table 8.1 shows the number of sources and detected flares sorted by several physical parameters such as class, age, mass, and binarity. We should note that our flare detection method (§5.5) largely depends on the quiescent flux level; the higher quiescent count rate results in a higher sensitivity to smaller amplitude flares due to small statistical errors. We hence show the mean quiescent flux for each class in the last column of Table 8.1. Following Stelzer et al. (2000), the flare rate (F) is defined as

$$F = \frac{(\bar{\tau_r} + \bar{\tau_d})N_F}{NT_{obs}} \pm \frac{\sqrt{\sigma_{\tau_r}^2 + \sigma_{\tau_d}^2}\sqrt{N_F}}{NT_{obs}}, \tag{8.1}$$

where ($\bar{\tau_r}$, $\bar{\tau_d}$) and (σ_{τ_r}, σ_{τ_d}) are the mean value and uncertainty of (τ_r, τ_d), N and N_F are the number of sources and detected flares, and T_{obs} is the duration of the observations (≈100 ks). All derived values of F are much higher than that derived with *ROSAT* ($F \sim 1$ %: Stelzer et al. 2000), which may be primarily due to the extended sensitivity in the hard X-ray band of the *Chandra* observations, because the flare activity (flux increase) is clearer in the harder X-ray band.

We see larger flare rate of class III+III$_c$ than that of class II. However, this is simply due to the effect of the flares with unusually long timescales (A-2, A-63, and BF-96). In fact, if we regard those unusual flares are affected by other unknown components (unresolved flares, for example) and exclude them, F of class III+III$_c$ becomes ∼5.0 % (parentheses in Table 8.1), which is significantly smaller than those of class I–II sources. Such a tendency is consistent with the *ROSAT* results (F

= 1.1±0.4 % and 0.7±0.2 % for class II and III). Also, there is a relation that lower mass sources show lower flare rate (∼5 %). However, this would be merely due to lower quiescent flux (≅ lower luminosity) for lower mass sources (Figure 7.8 left), hence it is still controversial whether the flare rate is affected by the stellar mass or not. In the last row of Table 8.1, we show the data of sources previously revealed as binary systems (Simon et al., 1995; Haisch et al., 2002); A-22, A-23/A-24 (see §6.3.2 and §6.3.3), A-41, A-78, A-82, BF-46, BF-61, and BF-96. Although the flare rate of binary sources is significantly larger than the others like the Taurus-Auriga-Perseus sources (Stelzer et al., 2000), the effect of the flare detection sensitivity can not be negligible; the quiescent flux of the binary sources is ∼4–10 times larger than the others.

Table 8.1: Flare rate sorted by several physical parameters

Parameter range	N^*	$N_F{}^\dagger$	$\bar{\tau_r}^\ddagger$ (ks)	$\bar{\tau_d}^\ddagger$ (ks)	$F^\S$ (%)	log[Flux(Q)]$^\parallel$
– Class –						
Class I	8	8	3.4±0.8	11.6±3.0	15.0±1.1	−13.2
Class II	63	36	6.2±1.4	7.9±1.0	8.0±0.2	−13.6
Class III+III$_c$	27	16	10.1±6.5	11.5±3.9	12.6±1.1	−13.6
			(3.1±0.6)	(6.9±0.8)	(5.0±0.1)	
– Age (Myr) –						
$t \leq 0.1$	11	11	3.6±0.6	29.2±12.1	32.8±3.6	−13.2
			(3.7±0.8)	(8.6±2.0)	(10.9±0.7)	
$0.1 < t \leq 0.5$	20	15	7.9±2.4	9.4±1.6	13.0±0.6	−13.3
$0.5 < t$	12	7	17.8±10.8	5.4±1.6	13.5±2.4	−13.4
			(8.2±6.3)	(4.0±1.0)	(6.6±1.4)	
– Mass ($M_\odot$) –						
$M \leq 0.2$	11	4	3.3±1.2	9.7±3.7	4.7±0.7	−14.2
$0.2 < M \leq 0.4$	23	20	8.4±2.2	11.4±3.1	17.2±0.7	−13.1
			(8.7±2.3)	(8.5±2.5)	(14.8±0.7)	
$0.4 < M$	9	9	9.3±6.7	28.7±15.8	38.0±5.7	−12.9
			(2.5±0.5)	(6.2±2.2)	(7.4±0.8)	
– Binarity –						
Binary$^\#$	9	9	8.4±6.0	8.9±1.6	17.3±2.1	−12.9
			(2.5±0.4)	(8.3±1.7)	(10.8±0.6)	
Others	102	57	4.9±0.8	11.9±2.6	9.8±0.2	−13.7
			(4.9±0.9)	(7.9±0.9)	(7.2±0.1)	

*The number of X-ray sources.

†The number of detected flares (§5.5).

‡Mean values of τ_r and τ_d. Parentheses indicate the mean values when we exclude the flares with unusually long timescales (A-2, A-63, and BF-96).

§Flare rate defined by Eq.(8.1) (Stelzer et al., 2000). Parentheses indicate the mean values when we exclude the flares with unusually long timescales (A-2, A-63, and BF-96).

$^\parallel$Mean value of quiescent X-ray flux (ergs s^{-1} cm^{-2}).

$^\#$Sources previously revealed as binary systems (Simon et al., 1995; Haisch et al., 2002).

8.2 Correlation between the Flare X-ray Parameters

Figures 8.1 and 8.2 show the correlations between the derived parameters of flares; τ_r vs τ_d and $< kT >$ vs τ_r. In these figures, we exclude those flares that could not determine errors mainly due to the limited statistics. Possible positive and negative log-linear correlations can be seen in τ_r vs τ_d and $< kT >$ vs τ_r, respectively. We hence check the significances of these correlations using the Cox's proportional hazard model (Isobe et al., 1986) in ASURV. This gives the significances of $\sim$99 % (τ_r vs τ_d) and $\sim$94 % ($< kT >$ vs τ_r). We further estimate the best-fit log-linear models with ASURV to be

$$(\frac{\tau_d}{\mathrm{s}}) = 10^{2.5\pm0.4}(\frac{\tau_r}{\mathrm{s}})^{0.4\pm0.1}, \tag{8.2}$$

$$(\frac{\tau_r}{\mathrm{s}}) = 10^{3.8\pm0.1}(\frac{< kT >}{\mathrm{keV}})^{-0.4\pm0.3}. \tag{8.3}$$

These models are shown by the solid lines in Figures 8.1 and 8.2.

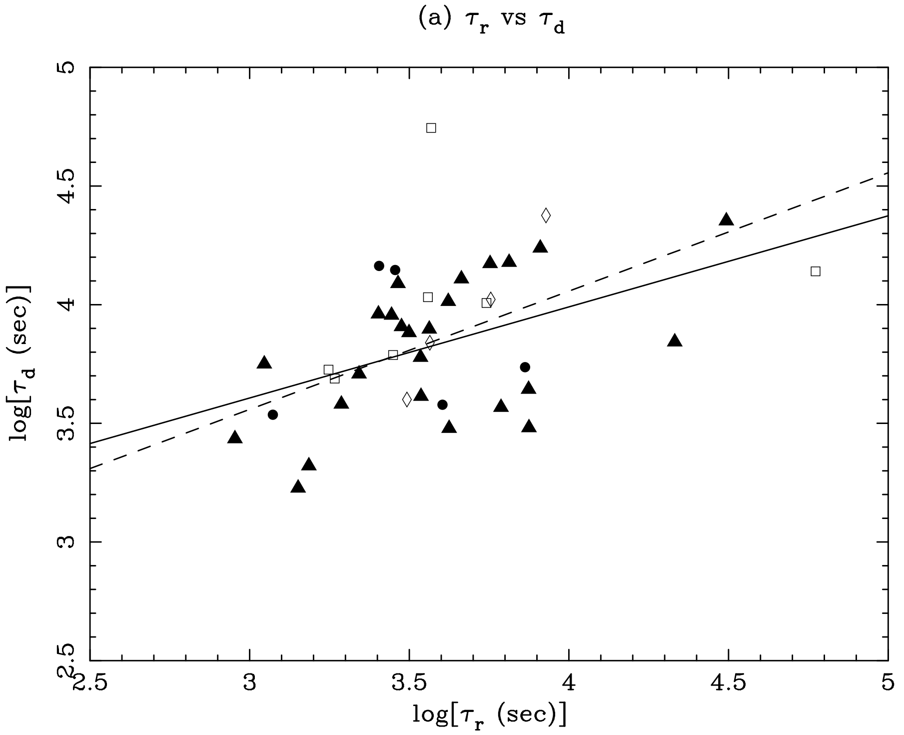

Fig. 8.1.— Relation between the rise and decay timescales of flares (τ_r and τ_d). Symbols are the same as Figure 7.6. The solid line represents the best-fit log-linear correlations derived with ASURV (Eq.8.2). The dashed line is the best-fit model of Eq.(C.12).

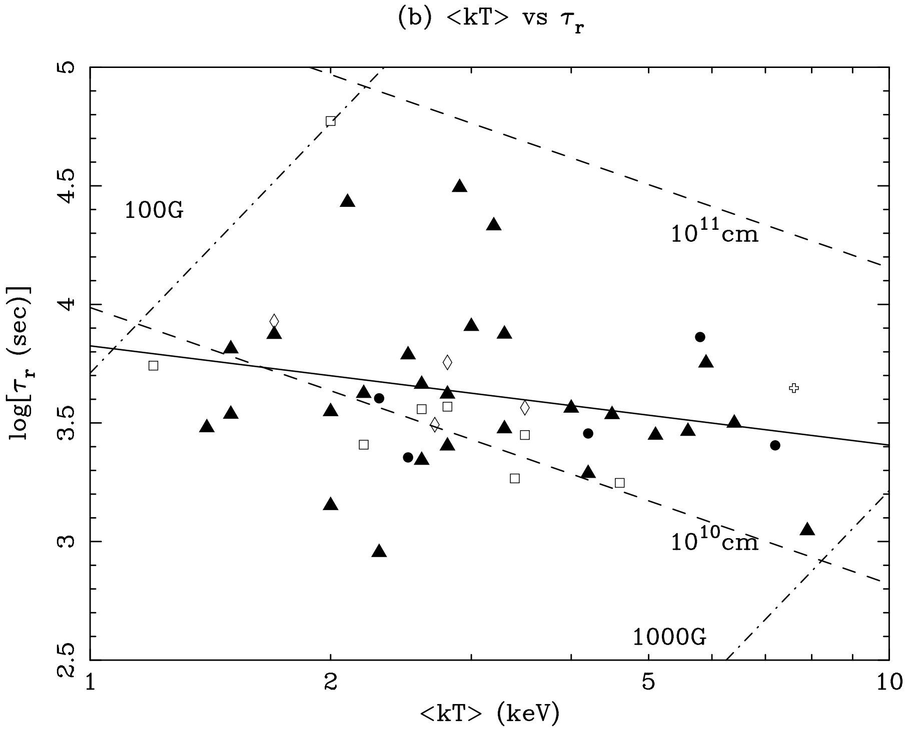

Fig. 8.2.— Relation between the temperature and rise timescale of flares (kT and τ_r). Symbols are the same as Figure 7.6. The solid line represents the best-fit log-linear correlations derived with ASURV (Eq.8.3). The dash-dotted and dashed lines in (b) are constant B and L lines derived by Eqs.(C.14) and (C.15) with the assumption of $n_c = 10^{10.48}$ cm^{-3}.

8.3 Magnetic Reconnection Model

In order to explain the observed features of the flare parameters, we formulate τ_r, τ_d, and $< kT >$ as a function of pre-flare (coronal) electronic density (n_c), half-length of the reconnected magnetic loop (L) and strength of magnetic field (B), which are based on the idea of a standard magnetic reconnection model (Petschek, 1964) and the balance between reconnection heating and conductive cooling (Shibata & Yokoyama, 2002). For simplicity, we assume that τ_d is equal to the radiative loss timescale (τ_{rad}), although it would be possible that τ_d is slightly larger than τ_{rad} (see Appendix C.4). We also assume that the reconnection rate M_A (ratio of the reconnection interval and Alfvén timescales; Eq.C.7) is 0.01, which is the mean value of M_A for the solar observations (0.001–0.1, Table 2 in Isobe et al. 2002). Details of the formulae are given in Appendix C.

8.3.1 τ_r vs τ_d – Implication of the pre-flare density

From Eq.(C.12), the reconnection model predicts the positive correlation between τ_r and τ_d as $\tau_d = A\tau_r^{1/2}$. The slope of 1/2 shows good agreement with the observed value of 0.4±0.1 (Eq.8.2), hence supports our assumption that the decay phase is dominant by radiative cooling. From Eq.(C.12), we re-estimate log(A) with the fixed slope of 1/2 to be 2.06±0.04 (the dashed line in Figure 8.1). We also calculate log(A) separately for each class, then obtain 2.1±0.1, 2.0±0.1, and 2.0±0.1 for class I, II, and III+III$_c$, respectively. We see no significant difference between the classes, hence A is assumed to be the same for all sources. Since A is a function of n_c (Eq.C.13), we can determine n_c to be

$$n_c = 10^{10.48\pm0.09}(\frac{M_A}{0.01})\ [\mathrm{cm}^{-3}]. \tag{8.4}$$

Considering the possible range of M_A (0.001–0.1), this favors higher pre-flare density for YSOs (10^9–10^{12} cm^{-3}) than that for the sun ($\sim10^9$ cm^{-3}). In fact, Kastner et al. (2002) derived the plasma density of a CTTS (TW Hydrae) using the ratio of $\mathrm{Ne_{IX}}$ and $\mathrm{O_{VII}}$ triplets and found extremely high density of $\sim10^{13}$ cm^{-3} even in their quiescent phase. Hence larger n_c value for YSOs than that for the sun would be common feature.

8.3.2 $< kT >$ vs τ_r – Loop length and magnetic field strength

The predicted correlations between $< kT >$ and τ_r are shown in Eqs. (C.14) and (C.15). Positive ($\tau_r \propto < kT >^{7/2}$) and negative ($\tau_r \propto < kT >^{-7/6}$) correlations are expected for the constant B and L values, respectively. The dash-dotted and dashed lines in Figure 8.2 show the constant B and L lines, in which we uniformly assume $n_c = 10^{10.48}$ cm^{-3} (Eq.8.4). Our observed negative correlation therefore predicts that flares with higher temperature is mainly due to larger magnetic field. However, the observed slope of -0.4 ± 0.3 is significantly flatter than $-7/6$ (Eq. C.15), hence the effect of L would not be negligible. We estimate the mean B and L for each class (Table 8.2) using the mean values of $< kT >$ and τ_r (Figures 7.4b and 7.5a), which is summarized in Table 8.2. Younger sources tend to show larger B values; the mean values of B are ∼500, 300, and 200 G for class I, II, and III+III$_c$ sources, respectively. This is consistent with the observed result of higher plasma temperature for younger sources. Also, the estimated values of L (10^{10}–10^{11} cm) suggest that L is nearly the same among these classes, comparable to the typical radius of YSOs. These results indicate that the flare loops for all classes are localized at the stellar surface, which is in sharp contrast with the idea of the flares for class I sources triggered by the larger flare loops connecting the star and the disk (Montmerle et al., 2000).

It is conceivable that the class III flares with unusually long timescales (A-2, A-63, and BF-96) mainly affect the systematically lower B for class III sources. Since it is possible that two or more flares make such unusually long timescales, we re-estimate B and L using the mean value of τ_r without these flares (§7.3). The results are shown by the parentheses in Table 8.2. Again, we confirm the same results; class III+III$_c$ sources have lower B than, and comparable L (but slightly lower) to class I and II sources.

Table 8.2: The estimated mean values of the flare physical parameters

Class	— This work —			— kT vs EM —	
	$\log(n_c)^{\dagger\ddagger}$ (cm^{-3})	$\log(B)^{\dagger}$ (G)	$\log(L)^{\dagger}$ (cm)	$\log(B_{SY})^{\S}$ (G)	$\log(L_{SY})^{\S}$ (cm)
I	10.48±0.09	2.7±0.1	10.3±0.1	2.6±0.1	10.4±0.2
II	...	2.5±0.1	10.4±0.1	2.5±0.1	10.4±0.1
III+III$_c$	...	2.3±0.1	10.4±0.2	2.2±0.1	10.7±0.1
		$(2.4\pm0.1)^{\|}$	$(10.0\pm0.1)^{\|}$		
Equation*	(8.4)	(C.14)	(C.15)	(C.18)	(C.19)

*Equations in the text used for the estimation of each parameter.
†The values are derived by assuming $M_A = 0.01$
‡We assume the same values of n_c for all classes (see text).
§These values are estimated using the derived values of n_c ($= 10^{10.48}$ cm^{-3}, column 2).
‖The mean values for class III+III$_c$ when we exclude the flares with unusually long timescales (A-2, A-63, and BF-96).

8.4 Comparison with the kT-EM scaling law

Shibata & Yokoyama (2002) showed that L and B of flares can be estimated from the kT–EM plot (see Appendix C.3). This method is completely independent of the flare timescales (τ_r and τ_d), hence can be used as the consistency check of our estimation derived in §8.3. The $< kT >$–$< EM >$ relation of the ρ Oph flares is shown in Figure 8.3. Using ASURV, we determine the mean values of $\log(< EM >)$ to be 53.77±0.20, 53.33±0.07, and 53.48±0.16 for class I, II, and III+III$_c$ sources, respectively. We then calculate the mean values of the magnetic field strength and loop length (B_{SY} and L_{SY}) by Eqs.(C.18) and (C.19) using the estimated value of $n_c = 10^{10.48\pm0.09}$ cm^{-3} (§8.3.1). The results are shown in Table 8.2. The values of B_{SY} (100–1000 G) are much higher than those derived in Shibata & Yokoyama (2002) and Paper I (50–150G). This discrepancy is caused by two different assumptions of n_c value; 10^9 cm^{-3} for Shibata & Yokoyama (2002) and Paper I (typical value of the solar corona), and $10^{10.48}$ cm^{-3} for this paper. B_{SY} and L_{SY} show good agreement with those derived in §8.3.2 (B and L in Table 8.2); higher B_{SY} values for younger sources and the same order of L_{SY} comparable to the typical stellar radius. Therefore our estimation of n_c, L, and B using the τ_r–τ_d and $< kT >$–τ_r relations is cross-checked.

The same conclusion of §8.3 and this section also indicates the propriety of our assumption of $M_A = 0.01$. If we assume the smaller (or larger) value of M_A, n_c (Eq.8.4) becomes smaller (larger), which causes smaller (larger) estimations of B_{SY} (Eq.C.18) and makes larger discrepancy between B and B_{SY} (Table 8.2).

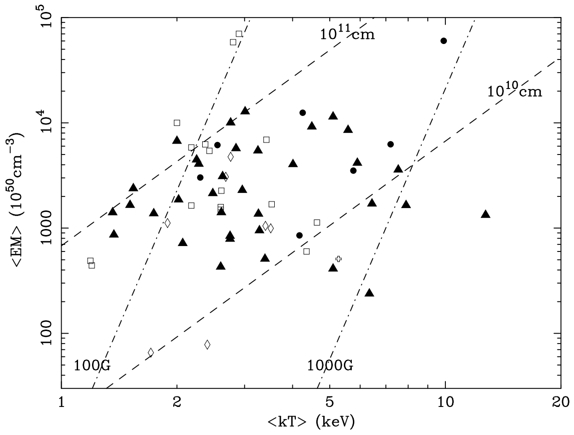

Fig. 8.3.— Plot of $< kT >$ and $< EM >$ in the flare phases. Symbols are the same as Figure 7.6. The dashed-dotted and dashed lines are constant B and L lines derived by Eqs.(C.18) and (C.19) with the assumption of $n_c = 10^{10.48}$ cm^{-3}.

8.5 Effect of the Quiescent X-rays on the Flare Analysis

It is conceivable that the quiescent X-rays put significant influence on the results of our flare analysis. Hence, in this subsection, we make and fit the flare spectra by subtracting the quiescent spectra as a background level and compare the results with those in the previous section. For the spectral fittings, the absorption column ($N_{\rm H}$) is fixed to be the best-fit value in Table 5.2.

Figure 8.4 shows the histogram of the newly estimated $< kT >$ in the flare phases. Since the statistics are highly limited due to the higher background level than that for the previous analysis, many faint flares can not constrain the 90 % confidence limit of $< kT >$. Hence, we only use the data whose errors are well determined. Although the mean values of $< kT >$ are systematically higher and lower than the previous results, overall properties are the same; higher $< kT >$ for class I and II sources than class III+III$_c$. Using ASURV, the significance level of higher $< kT >$ for class I and II sources is estimated to be $\gtrsim$ 92 %. This value is a bit smaller than the previous analysis (Table 7.2), which would be simply due to the limited samples for this analysis.

The plot of $< kT >$ and τ_r is shown in Figure 8.5. Similar to Figure 8.4, we only use the data whose 90 % confidence limit is well determined. The mean values of L are ∼2.6, 2.7, and 3.1 $\times 10^{10}$ cm, while those of B are ∼600, 300, and 200 G for class I, II and III+III$_c$, respectively.

Although there are slight differences between these values and the previous results, the relative tendency is the same; higher B for younger sources and almost comparable L to the stellar size.

We hence conclude that, even if we use the quiescent spectra as the background level for the flare spectra, the main results in the previous section are not affected so seriously.

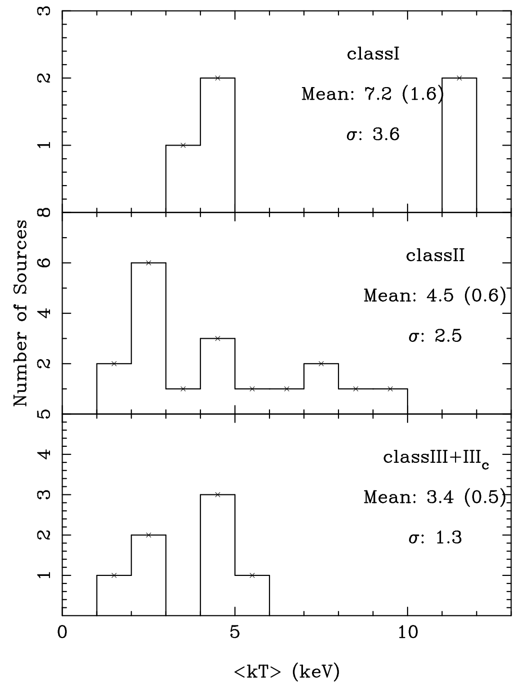

Fig. 8.4.— Same as Figure 7.4(b), but for the fitting results when the quiescent X-rays are used as background spectra.

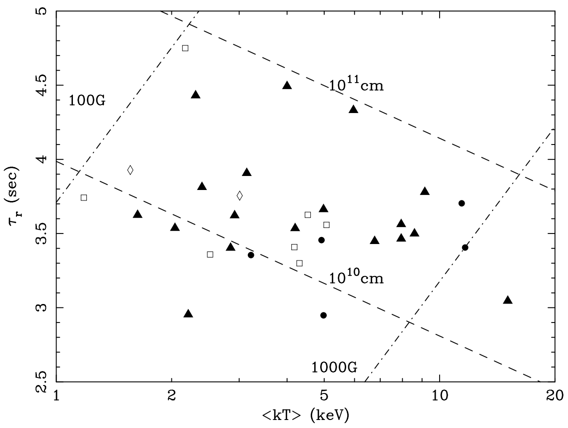

Fig. 8.5.— Same as Figure 8.2, but for the results when the quiescent X-rays are used as background spectra. Symbols are the same as Figure 7.6. The dashed and solid lines are the constant L and B lines derived by Eqs.(C.15) and (C.14).

8.6 Evolution of YSOs and Their Flare Activity

Combining all the results discussed in the previous sections, we propose a simple view of the evolution of flare activity on low-mass objects as follows. In their earlier stage (class I), sources have relatively strong magnetic field (≈500 G) and show frequent X-ray flares with higher temperature (≈5 keV). As stars evolve (class II and IIIs), the magnetic field gradually decreases (200–300 G) and makes moderate temperature plasma (2–4 keV) via X-ray flares. During these phases (class I–III), the length of the flare loop does not change significantly (10^{10}–10^{11} cm). As approaching to the main-sequence stage, the magnetic field and length of the flare loop are becoming weak (50–150 G for the sun) and short (10^8–10^9 cm), which causes lower plasma temperature (0.1–1 keV) and shorter flare timescales (10–100 s) as seen in the sun.

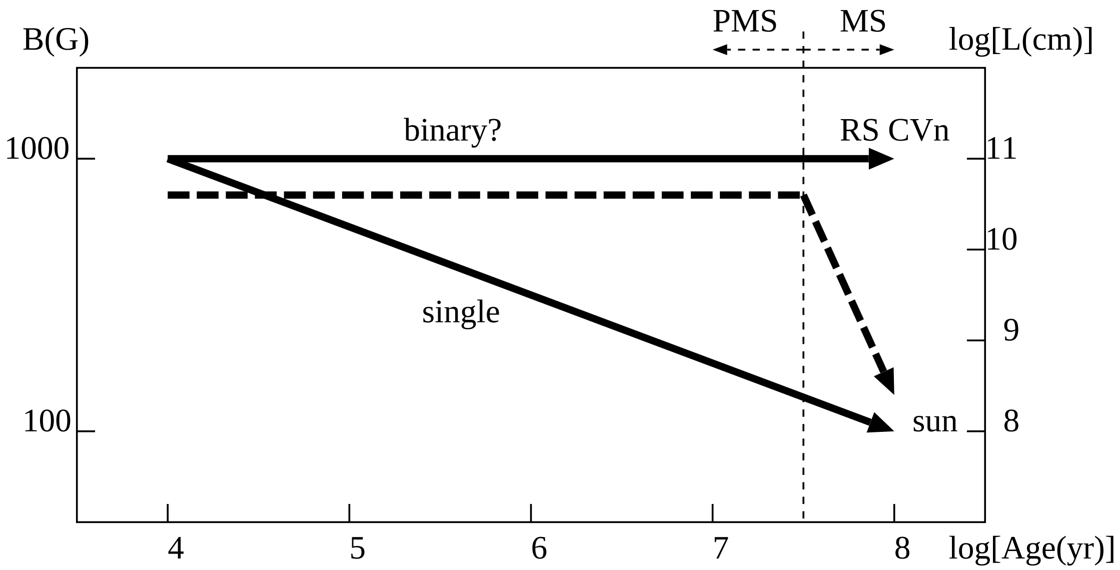

Fig. 8.6.— Schematic view of the evolution of X-ray flares of low-mass objects. Thick solid and dashed lines represent the predicted evolution of the magnetic field strength (B) and loop length (L), respectively.

We should note that the flare from the class 0 candidate A-29 (§6.5) has relatively short rise and decay timescales (1–2 ks). Although we could not plot the data of the A-29 flare in the $< kT >$–τ_r plane because $< kT >$ is not determined due to the limited statistics, the small τ_r value predicts that A-29 has a large magnetic field; if $< kT >$ is larger than 10 keV, the expected B value is $\gtrsim$1000 G, which may be the initial value of magnetic field in the YSO evolution.

Generally, RS CVn systems show smaller flare timescales than YSOs (∼100 s), while $< kT >$ is comparable (∼5 keV). Based on the above idea, this may be due to larger B value. In fact, Donati et al. (1990) estimated B of RS CVns as ≈1000 G, which is as large as the maximum value for YSOs (Figures 8.2 and 8.3).

8.7 Comment on the Giant Flares and Quiescent X-rays

Figure 8.3 indicates that the giant flares ($< EM > \gtrsim 10^{55}$ cm^{-3}) previously detected with *ASCA* such as V773 Tau (class III: Tsuboi et al. (1998)) and ROXs31 (class III: §6.2), as well as BF-64 = YLW16A (class I; $< EM > \sim 10^{55}$ cm^{-3}), should have either large L or B, if the sustained heating is negligible. Since the flares of ROXs31 and YLW16A show relatively large rise timescale ($\sim 10^4$ s), they may have large L values (10^{11}–10^{12} cm). The rise time of V773 Tau, on the other hand, is among the shortest ($\sim 10^3$ s), then the large L_X would be primarily due to the large B value. In fact, the detailed flare decay time analysis for V773 Tau predicted extremely large B value of $\gtrsim$1000 G (Favata et al., 2001). We suspect that the binary nature of V773 Tau (Welty, 1995) causes such an exceptionally large B, which would be the same case as the main-sequence RS CVn systems.

Although the mechanism of making the quiescent X-ray emission from YSOs is still controversial, one possible idea is the composition of multiple unresolved faint flares. If we assume that the magnetic field with the same strength as those of the flares makes quiescent X-rays, unresolved flares are expected to have smaller loop length, considering the systematically lower $< kT >$ and $< L_X >$ ($\cong < EM >$) values (Figures 7.2 and 7.4), which causes shorter flare timescales (Eq.C.8 and Eq.C.11). Such flares are hard to be detected because of the limited statistics. Future observations with much higher sensitivity would reveal what makes quiescent X-rays.

Chapter 9

Conclusion

We summarize the main results of the systematic analysis of two *Chandra* observations of ρ Oph with $\approx$100 ks exposure as follows;

1. From the central $\sim$1 pc $\times$ 2 pc region of ρ Oph, we detect 195 X-ray sources. About 60 % of them (110) are identified with optical and/or infrared counterpart, including class I, II, and III sources and some young brown dwarfs. The X-ray detection rate is surprisingly high of $\sim$60 %, hence we suspect that virtually all YSOs in ρ Oph may emit X-rays.

2. A total of 71 flares are detected. Most of the flares show the typical profile of the solar and stellar flares, while some bright flares have unusually long rise timescale.

3. All the X-ray spectra are well fitted by a single temperature thin plasma model of 0.3 solar abundances except for some sources. The plasma temperature is 0.6–5 keV in the quiescent phase, then becomes systematically higher (1–10 keV) in the flare phase. Class I–II sources show higher flare temperature than class III sources.

4. We find positive correlations of $N_{\rm H}$ vs A_V, $< L_X >$ vs $L_{\rm bol}$, $< L_X >$ vs mass, and $< L_X >$ vs $L_{\rm R}$.

5. There is a positive correlation between τ_r and τ_d, which is well explained by the standard magnetic reconnection model. Shorter τ_r and τ_d are due to the smaller L and/or larger B values.

6. We find a negative correlation between $< kT >$ and τ_r, which indicates the same order of the flare loop length regardless of their classes. Larger $< kT >$ values for class I and II sources are due to larger B values.

7. The expected loop length is comparable to the stellar size (10^{10}–10^{11} cm), indicating that the scenario of the star-disk arcade magnetic loop is unlikely.

Appendix A

Flare Light Curves

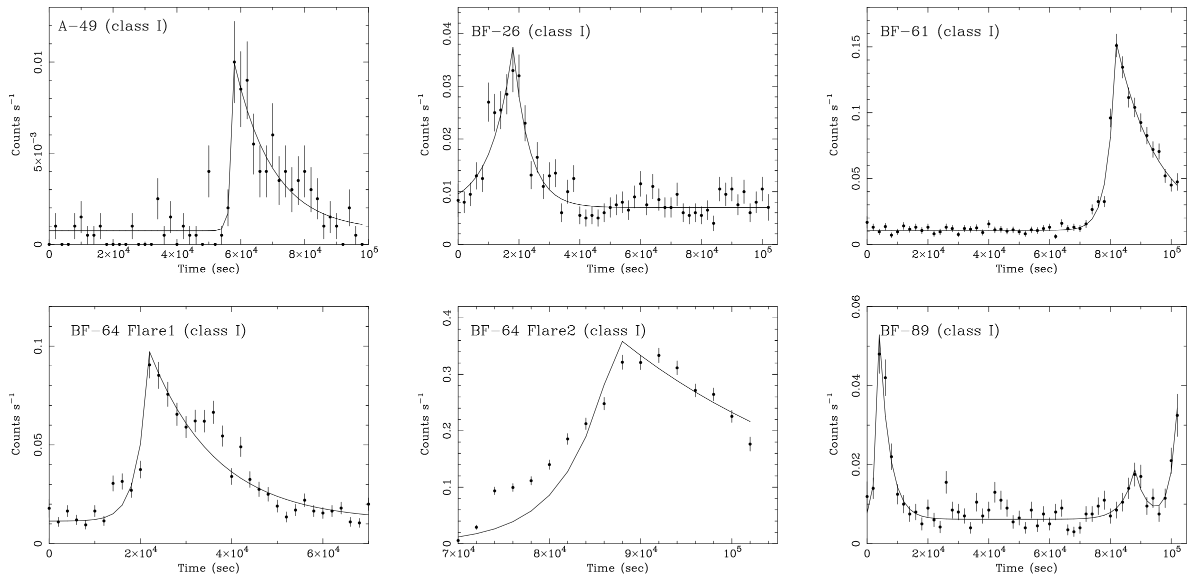

Fig. A.1.— Light curves of detected flares in 0.5–9.0 keV for class I sources, binned in 2000 s interval. Solid lines are the best-fit exponential model. Source name for each flare is shown at the upper-left of the panels. The time axis starts at MJD = 51679.9944 (obs-A) and 51647.7848 (obs-BF). Since the light curve of BF-64 suffer the photon pileup during the second flare, we show the two flares separately (the former is extracted from the 7.″5 radius and the latter is from 2.″5–7.″5).

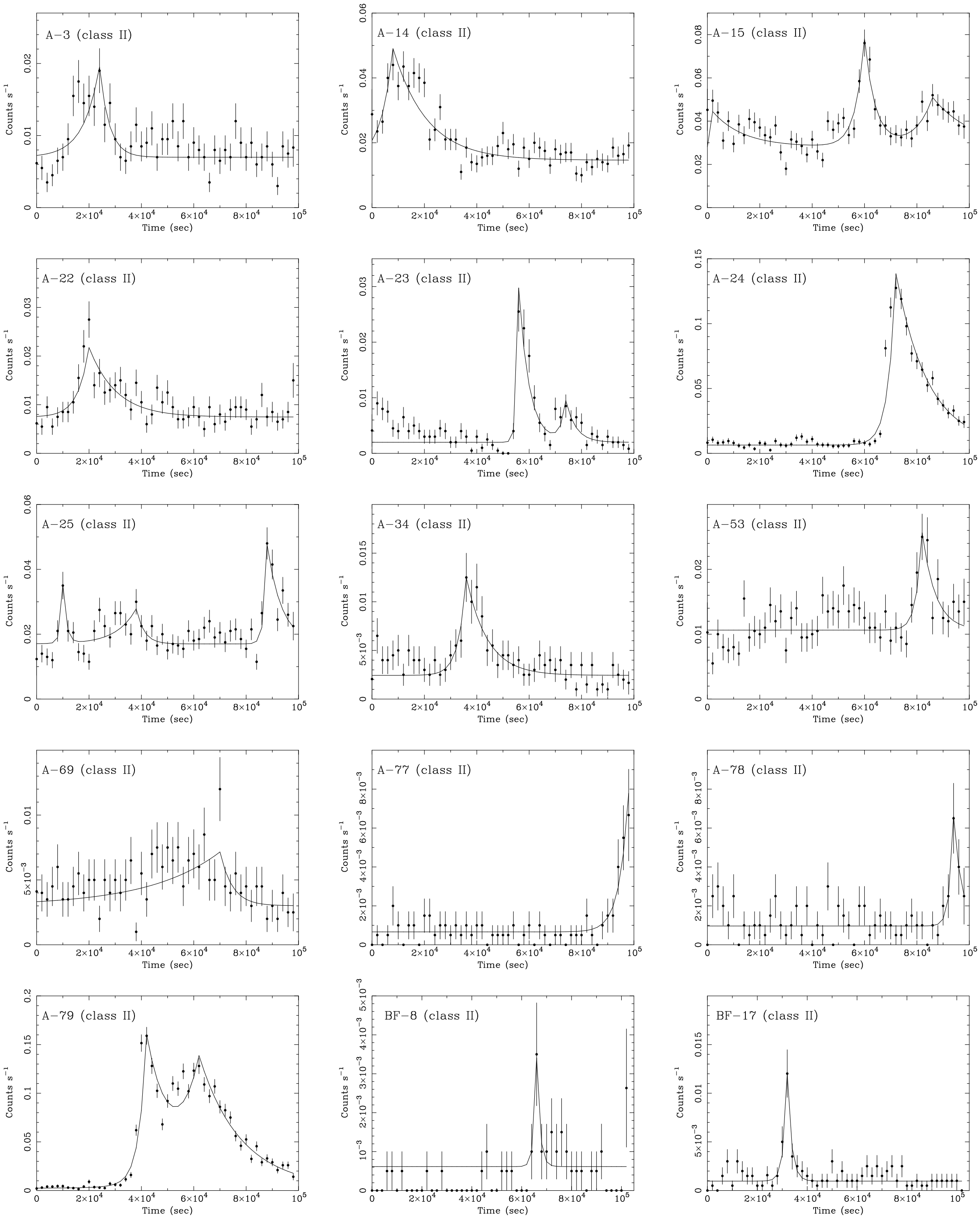

Fig. A.2.— Same as Figure A.1, but for class II sources.

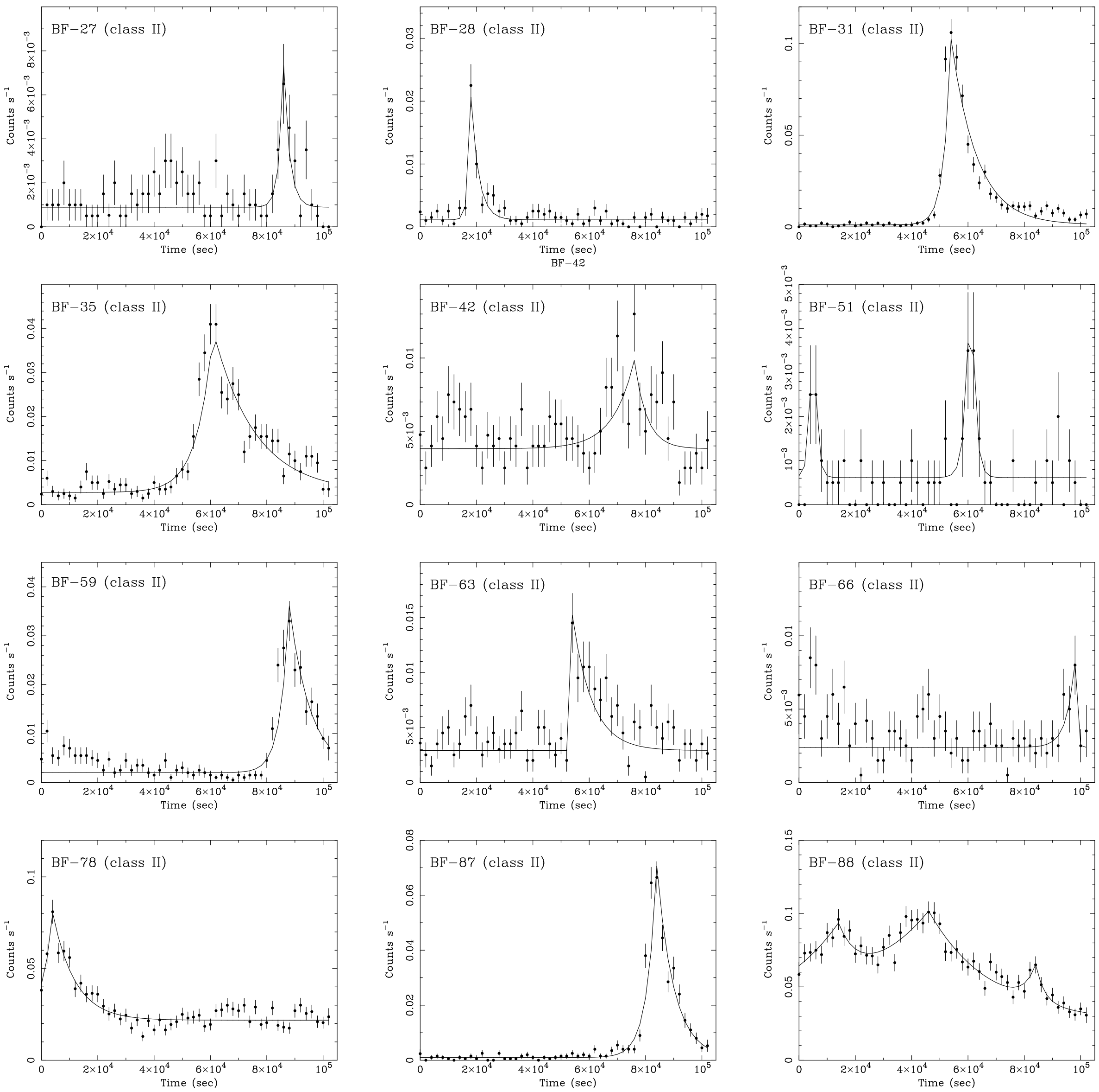

Fig.A.2 (Continued)

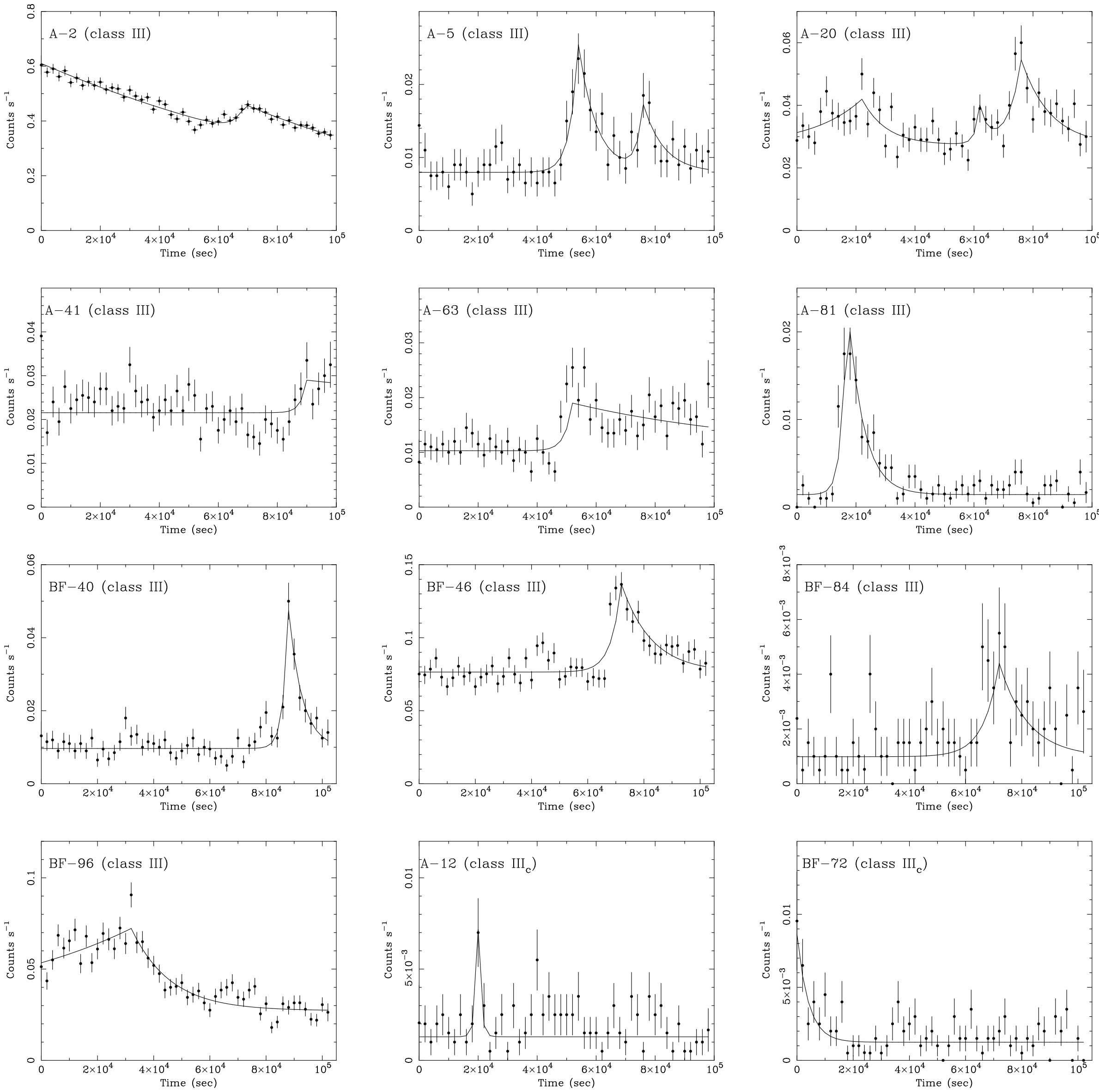

Fig. A.3.— Same as Figure A.1, but for class III+III$_c$ sources. The light curve of A-2 is extracted from a $2\farcs5$–$12\farcs5$ radius circle in order to avoid the pileup effect.

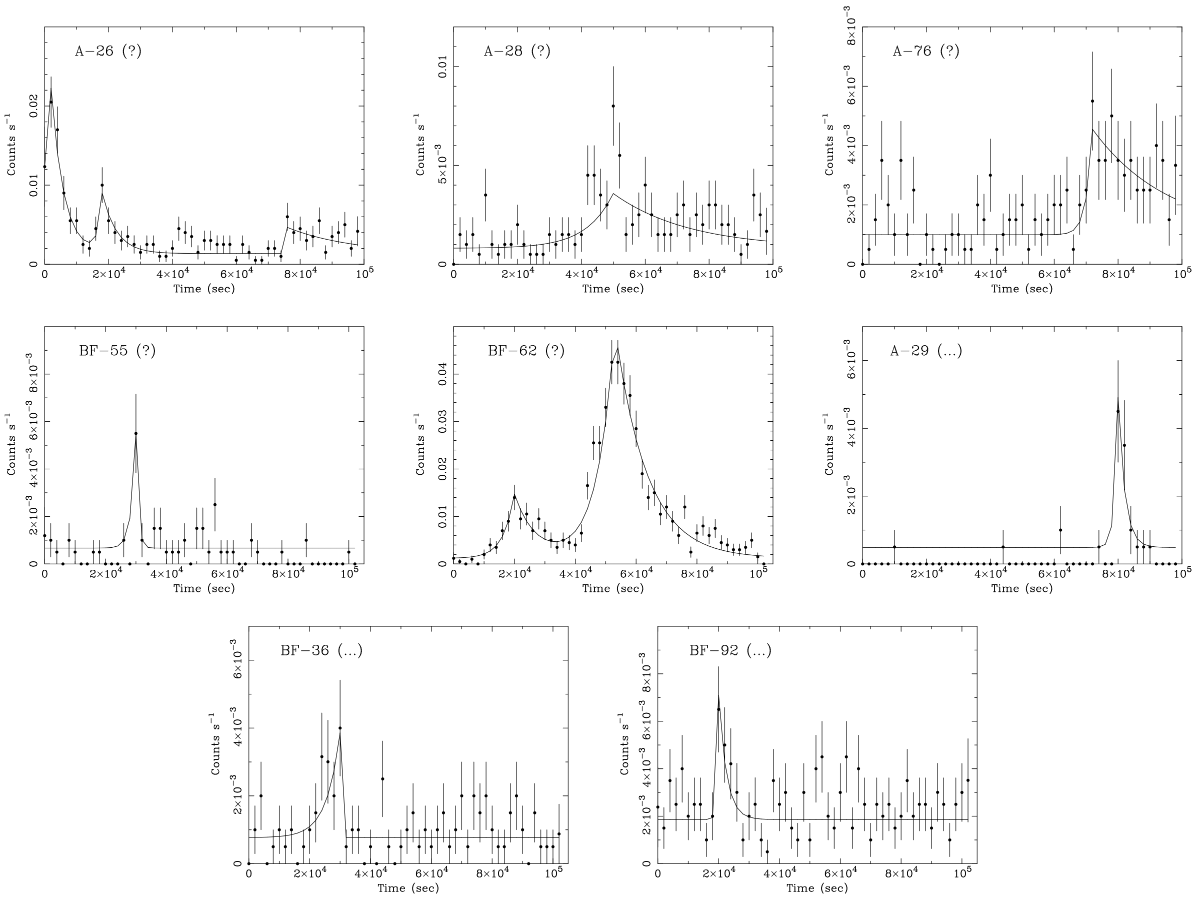

Fig. A.4.— Same as Figure A.1, but for unclassified NIR and unidentified sources.

Appendix B

Physical Parameters of YSOs

Here we summarize the physical parameters of YSOs. We estimate the stellar mass and age for sources whose $L_{\rm bol}$ and $T_{\rm eff}$ are well determined with the infrared spectroscopy (Luhman & Rieke, 1999), by comparing the position in the H-R diagram to the theoretical evolutionary model (D'Antona & Mazzitelli, 1997).

Table B.1:: Physical parameters of YSOs

No.	A_V * (mag)	$L_{\rm bol}$ † ($L_\odot$)	$T_{\rm eff}$ ‡ (K)	Sp. ‡	Age § (Myr)	Mass § ($M_\odot$)
		— Class I —				
A-49	···	0.17	···	···	···	···
BF-1	47‖	2.6	···	···	···	···
BF-26	57‖	26	···	···	···	···
BF-50	57‖	1.7	···	···	···	···
BF-61	56‖	6.7	···	···	···	···
BF-64	52‖	8.7	···	K8	···	···
BF-68	37‖	0.62	···	···	···	···
BF-89	48‖	1.1	···	···	···	···
BF-S7	···	0.36	···	···	···	···
		— Class II —				
A-3	19.5	0.22	···	···	···	···
A-6	22.6	0.95	3955	K8	0.5	0.40
A-14	9.4	1.4	4205	K6	0.3	0.35
A-15	1.8	0.72	3850	M0	0.5	0.30
A-19	17.1	0.97	···	···	···	···

Table B.1 (Continued)

No.	A_V * (mag)	L_{bol} † ($L_\odot$)	T_{eff} ‡ (K)	Sp.‡	Age§ (Myr)	Mass§ ($M_\odot$)
A-22	6.1	5.9	5080	K1	0.5	1.40
A-23	14.5	0.25	3850	M0	3	0.50
A-24	11.8	3.7	3955	K8	0.1	0.50
A-25	10.0	4.5	...	...	...	...
A-27	19.1	0.13	3010	M5	0.3	0.12
A-34	21.6	0.11	...	...	...	...
A-44	7.6	0.28	...	...	...	...
A-53	8.5	1.6	3850	M0	0.07	0.30
A-54	14.6	0.064	...	...	...	...
A-59	16.3	1.1	3955	K8	0.2	0.30
A-61	38.6	1.1	...	...	...	...
A-64	26.8	0.023	...	...	...	...
A-66	43.5	0.17	...	...	...	...
A-69	19.7	0.55	3850	M0	0.7	0.35
A-72	19.9	0.12	...	...	...	...
A-73	14.2	0.050	...	...	...	...
A-77	20.5	0.034	...	...	...	...
A-78	20.9	0.15	...	...	...	...
A-79	20.6	0.087	...	...	...	...
A-82	3.5	4.0	6590	F4	30	1.40
A-83	10.7	0.57	...	...	...	...
BF-2	(= A-61)					
BF-3	10.4	0.19	...	...	...	...
BF-4	(= A-64)					
BF-7	(= A-69)					
BF-8	14.2	0.007	...	...	...	...
BF-9	17.2	0.059	3180	M4	3	0.16
BF-10	...	29	...	...	...	...
BF-12	25‖	44	...	...	...	...
BF-15	(= A-77)					
BF-16	(= A-78)					
BF-17	(= A-79)					
BF-20	1.5	0.039	...	...	...	...
BF-21	22.5	0.12	...	...	...	...

Table B.1 (Continued)

No.	A_V * (mag)	L_{bol} † ($L_\odot$)	T_{eff} ‡ (K)	Sp. ‡	Age § (Myr)	Mass § ($M_\odot$)
BF-24	12.5	0.78	3955	K8	0.5	0.35
BF-25	19.4	0.075	···	···	···	···
BF-27	36.2	1.1	···	···	···	···
BF-28	73.4	52	···	···	···	···
BF-31	34.8	1.1	···	···	···	···
BF-33	45.7	0.34	···	···	···	···
BF-35	16.5	0.86	3850	M0	0.5	0.35
BF-39	36.9	0.99	···	M4	···	···
BF-41	24.7	0.023	···	···	···	···
BF-42	19.5	1.1	3595	M1.5	0.07	0.25
BF-44	42.2	1.3	···	···	···	···
BF-49	27.7	3.1	···	···	···	···
BF-51	31 ‖	···	···	···	···	···
BF-59	23.7	0.71	3680	M1	0.5	0.30
BF-63	9.8	0.42	3850	M0	1	0.40
BF-66	19.5	0.66	4132	K6.5	1	0.50
BF-71	26.8	1.9	3955	K8	0.1	0.35
BF-76	23.0	0.29	···	···	···	···
BF-78	10.8	1.6	3955	K8	0.07	0.30
BF-82	44.9	1.5	···	···	···	···
BF-85	10.1	1.1	3955	K8	0.2	0.30
BF-87	14.8	0.027	···	···	···	···
BF-88	6.4	0.80	3850	M0	0.5	0.35
BF-91 ††	11	0.20	3090	M4	0.3	0.15
BF-98	4.1	0.045	···	···	···	···
		— Class III —				
A-2 #	6.0	30	4800	K1	0.08	1.6
A-5	20.6	0.70	···	···	···	···
A-20	19.5	0.89	3955	K8	0.5	0.40
A-33	25.2	0.34	3595	M1.5	1	0.35
A-41	11.7 **	1100	18700	B3	0.2	7.5
A-51	55.5	2.0	···	···	···	···
A-52	48.5	1.1	···	···	···	···
A-56	15.2	0.83	3850	M0	0.5	0.35

Table B.1 (Continued)

No.	A_V * (mag)	L_{bol} † ($L_\odot$)	T_{eff} ‡ (K)	Sp.‡	Age§ (Myr)	Mass§ ($M_\odot$)
A-63	15.7	2.8	4205	K6	0.07	0.40
A-71	22.5	0.84	3955	K8	0.5	0.35
A-81	36.5	1.6	···	···	···	···
A-84	17.1	1.2	4205	K6	0.5	0.50
BF-19	(= A-81)					
BF-40	59.8	39	···	···	···	···
BF-46#	1.2	0.63	3800	M0	0.6	0.37
BF-75	27.5	0.90	···	···	···	···
BF-84	11.5	0.60	3180	M4	0.07	0.18
BF-96#	6.0	0.50	3890	K7	1	0.47
— Class III$_c$ —						
A-12	17.4	0.64	3595	M1.5	0.2	0.25
A-32	21.7	0.45	···	···	···	···
A-36	16.6	0.21	···	···	···	···
A-45	14.0	0.025	···	···	···	···
BF-56	10.8	0.004	···	···	···	···
BF-69	47.8	1.3	···	···	···	···
BF-72	13.1	0.32	···	···	···	···
BF-79	4.8	0.32	3180	M4	0.7	0.20
BF-90	16.3	0.43	···	···	···	···
— Unclassified NIR sources —						
A-16	···	···	···	···	···	···
A-26††	56	0.71	2840	M5.5	<0.1	0.10
A-28	···	···	···	···	···	···
A-46	···	···	···	···	···	···
A-60	···	···	···	···	···	···
A-76	···	···	···	···	···	···
A-80	···	···	···	···	···	···
BF-22	···	···	···	···	···	···
BF-55	38‖	···	···	···	···	···
BF-57	···	···	···	···	···	···
BF-62	···	···	···	···	···	···
BF-74	···	···	···	···	···	···
— BD —						

Table B.1 (Continued)

No.	A_V* (mag)	L_{bol}† ($L_\odot$)	T_{eff}‡ (K)	Sp.‡	Age§ (Myr)	Mass§ ($M_\odot$)
BF-86††	5.7	0.055	2350	M8.5	<0.1	0.04
BF-S2‡‡	0.8	0.008	2590	M8.5	···	<0.02
— BD_c —						
A-30††	6.3	0.024	2760	M6	2.0	0.06
A-38††	11	0.051	2760	M6	1.0	0.08
A-S2††	4.5	0.063	2590	M7	0.2	0.06

*Visual extinction derived from an IR color (Bontemps et al., 2001).

†Bolometric luminosity estimated from an intrinsic NIR–MIR band magnitude. (Bontemps et al., 2001).

‡Effective surface temperature and its spectral type derived by an NIR spectroscopy (Luhman & Rieke, 1999).

§Stellar age and mass derived from the locus in the H-R diagram (Figure 2.1).

‖Casanova et al. (1995).

#Nürnberger et al. (1998).

**Chini (1981).

††Wilking et al. (1999).

‡‡Cushing et al. (2000).

Appendix C

Modeling of the Flare

In this appendix, we show details for the estimation of the flare parameters (τ_r, τ_d, and kT), which are used in chapter 8. These formulations are based on the standard magnetic reconnection model (Petschek, 1964), as well as the observed results and analysis of solar flares.

C.1 Estimation of the Flare Parameters

- **Plasma temperature ($< kT >$)**

  Fisher & Hawley (1990) showed that the flare maximum temperature, T_{max} [K], is determined by the balance between the heating rate (Q ergs s^{-1} cm^{-3}) and conduction cooling ($\propto T_{max}^{7/2}/L^2$), then obtained an equation,

  $$T_{max} \cong (\frac{2QL^2}{\kappa_0})^{2/7}, \tag{C.1}$$

  where L and κ_0 are the semi-length of the flare loop and Spitzer's thermal conductivity ($\equiv 9.0\times10^{-7}$; Spitzer 1956). For the magnetic reconnection, Q is equal to the Poynting flux divided by L, i.e.,

  $$Q \cong \frac{c}{4\pi L}\mathbf{E}\times\mathbf{B} = \frac{(\mathbf{B}\times\mathbf{v})\times\mathbf{B}}{4\pi L} = \frac{B^2 v}{4\pi L}, \tag{C.2}$$

  where E, B, and v are electric field strength, magnetic field strength, and fluid velocity, respectively. v is assumed to be the Alfvén velocity;

  $$v = v_A \equiv \frac{B}{\sqrt{4\pi m n_c}}, \tag{C.3}$$

  where m and n_c are the proton mass ($\equiv 1.67\times10^{-24}$ g) and pre-flare (coronal) density, respectively. Numerical simulations (Yokoyama & Shibata, 1998) further showed that the observed maximum temperature (T) is a factor of ~3 lower than T_{max}. Finally, Shibata & Yokoyama (1999, 2002) obtained the following relation;

$$T \cong \frac{1}{3}T_{max} \cong 6.75 \times 10^7 (\frac{n_c}{10^9 \text{ cm}^{-3}})^{-1/7} (\frac{L}{10^{11} \text{ cm}})^{2/7} (\frac{B}{100 \text{ G}})^{6/7} \text{ [K]}, \quad (C.4)$$

As for the usual stellar flares, we can only determine the time-averaged temperature ($< kT >$) due to the limited statistics. However, van den Oord et al. (1988) showed that the behavior of the flare temperature is exponential, hence we obtain the relation

$$T = \frac{\tau_r + \tau_d}{\int_{-\tau_r}^{0} e^{t/\tau_r} dt + \int_0^{\tau_d} e^{-t/\tau_d} dt} \cdot < T > \cong 1.6 < T > \quad (C.5)$$

Using Eqs. (C.4) and (C.5), $< kT >$ is determined as

$$< kT > \cong 3.64 (\frac{n_c}{10^9 \text{ cm}^{-3}})^{-1/7} (\frac{L}{10^{11} \text{ cm}})^{2/7} (\frac{B}{100 \text{ G}})^{6/7} \text{ [keV]}. \quad (C.6)$$

- **Rise timescale (τ_r)**

  On the basis of a standard reconnection model, τ_r is equal to the interval of magnetic reconnection. Petschek (1964) showed that the reconnection timescale is proportional to the Alfvén time, $\tau_A \equiv L/v_A$. Hence τ_r is,

$$\tau_r = \frac{\tau_A}{M_A} = \frac{\sqrt{4\pi m n_c} L}{M_A B} \quad (C.7)$$

The correction factor M_A, sometimes referred as the reconnection rate, is estimated to be 0.01–0.1 (Petschek, 1964), while the observations for the solar flares show that M_A is in the range of 0.001–0.1 (Table 2 in Isobe et al. 2002), regardless of their flare size. τ_r is therefore,

$$\tau_r \cong 1.45 \times 10^4 (\frac{M_A}{0.01})^{-1} (\frac{n_c}{10^9 \text{ cm}^{-3}})^{1/2} (\frac{L}{10^{11} \text{ cm}}) (\frac{B}{100 \text{ G}})^{-1} \text{ [s]}. \quad (C.8)$$

- **Decay timescale (τ_d)**

  We assume that τ_d is nearly the same as the radiative cooling timescale (τ_{rad}), i.e,

$$\tau_d \cong \tau_{rad} \equiv \frac{3nkT}{n^2 \Lambda(T)}, \quad (C.9)$$

where n and $\Lambda(T)$ are the maximum plasma density and radiative loss function given by $10^{-24.73}\ T^{1/4}$ for $T > 20$ MK (Mewe et al., 1985). Furthermore, we assume that magnetic pressure is comparable to plasma pressure at the flare peak;

$$2nkT = \frac{B^2}{8\pi}. \quad (C.10)$$

Using Eqs.(C.4), (C.9), and (C.10), we obtain τ_d as

$$\tau_d \cong 7.75 \times 10^4 (\frac{n_c}{10^9 \text{ cm}^{-3}})^{-1/4} (\frac{L}{10^{11} \text{ cm}})^{1/2} (\frac{B}{100 \text{ G}})^{-1/2} \text{ [s]}. \quad (C.11)$$

C.2 Predicted Correlations between the Flare Parameters

- **τ_r vs τ_d**
  Using Eqs.(C.8) and (C.11), we obtain a relation

$$(\frac{\tau_d}{\mathrm{s}}) = A(\frac{\tau_r}{\mathrm{s}})^{1/2}, \tag{C.12}$$

  where

$$A \cong 640(\frac{n_c}{10^9\ \mathrm{cm}^{-3}})^{-1/2}(\frac{M_A}{0.01})^{1/2}. \tag{C.13}$$

  Hence the positive correlation is expected between τ_r and τ_d.

- **$< kT >$ vs τ_r**
  From Eqs.(C.6), (C.8) and (8.4), we obtain

$$\tau_r \cong 10^{2.20}(\frac{n_c}{10^9\mathrm{cm}^{-3}})(\frac{M_A}{0.01})^{-1}(\frac{B}{100\ \mathrm{G}})^{-4}(\frac{< kT >}{\mathrm{keV}})^{7/2}\ [\mathrm{s}], \tag{C.14}$$

$$\tau_r \cong 10^{4.82}(\frac{n_c}{10^9\mathrm{cm}^{-3}})^{1/3}(\frac{M_A}{0.01})^{-1}(\frac{L}{10^{11}\ \mathrm{cm}})^{4/3}(\frac{< kT >}{\mathrm{keV}})^{-7/6}\ [\mathrm{s}]. \tag{C.15}$$

  These equations indicate that the positive and negative log-linear correlations of $< kT >$ vs τ_r are expected if B and L are equal for all sources, respectively.

C.3 The kT–EM Scaling Law

Using Eqs.(C.4), (C.10), and assuming $V \cong L^3$ (V: plasma volume), Shibata & Yokoyama (2002) derived the relation between the flare maximum temperature (T) and emission measure (EM, Eqs. 5–6 in Shibata & Yokoyama 2002). Similar to Eq.(C.5), the time behavior of EM is also exponential (van den Oord et al., 1988), hence we assume $EM \cong 1.6 < EM >$. We thus replace Eqs.(5) and (6) in Shibata & Yokoyama (2002) as

$$< EM > \cong 3.7 \times 10^{48}(\frac{n_c}{10^9\ \mathrm{cm}^{-3}})^{3/2}(\frac{B}{100\ \mathrm{G}})^{-5}(\frac{< kT >}{\mathrm{keV}})^{17/2}\ [\mathrm{cm}^{-3}], \tag{C.16}$$

$$< EM > \cong 7.0 \times 10^{51}(\frac{n_c}{10^9\ \mathrm{cm}^{-3}})^{2/3}(\frac{L}{10^{11}\ \mathrm{cm}})^{5/3}(\frac{< kT >}{\mathrm{keV}})^{8/3}\ [\mathrm{cm}^{-3}]. \tag{C.17}$$

We also derive the following two equations

$$B \cong 52(\frac{n_c}{10^9\ \mathrm{cm}^{-3}})^{3/10}(\frac{< EM >}{10^{50}\ \mathrm{cm}^{-3}})^{-1/5}(\frac{< kT >}{\mathrm{keV}})^{17/10}\ [\mathrm{G}], \tag{C.18}$$

$$L \cong 7.8 \times 10^9(\frac{n_c}{10^9\ \mathrm{cm}^{-3}})^{-2/5}(\frac{< EM >}{10^{50}\ \mathrm{cm}^{-3}})^{3/5}(\frac{< kT >}{\mathrm{keV}})^{-8/5}\ [\mathrm{cm}]. \tag{C.19}$$

C.4 Possible Error for the Derived Parameters

In the discussions of the main text (chapter 8), the assumption of τ_d (Eq.C.9) includes relatively large uncertainty. Reale et al. (1997) proposed that τ_d becomes about a factor of $\lesssim 10$ larger than the radiative loss timescale (τ_{rad}), if the sustained heating exists during the decay. The dependences of the relevant parameters on τ_d are;

$$n_c \propto \tau_d^{-2} \tag{C.20}$$

$$B \propto n_c^{1/4} \propto \tau_d^{-1/2}. \tag{C.21}$$

$$L \propto n_c^{-1/2} \propto \tau_d^{1} \tag{C.22}$$

Accordingly, n_c has large dependence on τ_d; larger n_c value than $\sim 10^{10.5}$ cm^{-3} may be conceivable. The dependence of L is also relatively large. However, this uncertainty makes L much smaller, hence larger flare loops is still less possible.

Another uncertainty is in the kT–EM scaling law. Shibata & Yokoyama (2002) showed that the effect of the filling factor f ($V = fL^3$) may not be negligible. This gives possible errors for the values in columns [5]–[6] of Table 8.2. The dependences of the relevant parameters on f are;

$$B_{SY} \propto EM^{-1/5} \propto f^{1/5} \tag{C.23}$$

$$L_{SY} \propto EM^{3/5} \propto f^{-3/5} \tag{C.24}$$

Hence slightly smaller and larger values of B_{SY} and L_{SY} would be conceivable, although the effect is only a factor of < 5 (if $f = 0.1$).

Bibliography

Ageorges, N., Eckart, A., Monin, J. L., & Ménard, F. 1997, A&A, 326, 632

Anders, E., & Grevesse, N. 1989, Geochimica et Cosmochimica Acta, 53, 197

André, P., Montmerle, T., & Feigelson, E. D. 1987, AJ, 93, 1182

André, P., Montmerle, T., Feigelson, E. D., Stine, P. C., & Klein, K. 1988, ApJ, 335, 940

André, P., Ward-Thompson, D., & Barsony, M. 1993, ApJ, 406, 122

André, P. 1994, in The Cold Universe, ed. T. Montmerle, C. J. Lada, I. F. Mirabel, J Trân Thanh Vân (France: Gif-sur-Yvette), 179

André, P., & Montmerle, T. 1994, ApJ, 420, 837

Audard, M., Güdel, M., & Mewe, R. 2001, A&A, 365, L318

Awaki, H., Koyama, K., Inoue, H., Halpern, J. P. 1991, PASJ, 43, 195

Bachiller, R. 1996, ARA&A, 34, 111

Barsony, M., Burton, M. G., Russell, A. P. G., Carlstrom, J. E., & Garden, R. 1989, ApJ, 346, L93

Barsony, M. 1994, ASP Conf. Ser. 65, Clouds, Cores, and Low Mass Stars, D. P. Clemens & R. Barvainis (San Francisco: ASP), 197

Barsony, M., Kenyon, S. J., Lada, E. A., & Teuben, P. J. 1997, ApJS, 112, 109

Basri, G. 2000, ARA&A, 38, 485

Bevington, P. R., & Robinson, D. K. 1992, Data Reduction and Error Analysis for the Physical Science (2d ed.; Boston: WCB/McGraw-Hill)

Bontemps, S. et al.2001, A&A, 372, 173

Bouvier, J., & Appenzeller, I. 1992, A&AS, 92, 481

Brandner, W. et al. 2000, A&A, 364, L13

Brinkman, A. C. et al.2001, A&A, 365, L324

Burke, B. E., Mountain, R. W., Harrison, D. C., Bautz, M. W., Doty, J. P., Ricker, G. R., Daniels, P. J. 1991, IEEE Trans. ED-38, 1069

Carkner, L., Feigelson, E. D., Koyama, K., Montmerle, T., Reid, I. N. 1996, ApJ, 464, 286

Casanova, S., Montmerle, T., Feigelson, E. D., & André, P. 1995, ApJ, 439, 752

Chen, H., Myers, P. C., Ladd, E. F., & Wood, D. O. S. 1995, ApJ, 445, 377

Chen, H., Grenfell, T. G., Myers P. C., & Hughes, J. D. 1997, ApJ, 478, 295

Chini, R. 1981, A&A, 99, 346

Comerón, F., Rieke, G. H., Burrows. A., & Rieke, M. J. 1993, ApJ, 416, 185

Costa, V. M., Lago, M. T. V. T., Norci, L., and Neurs, E. J. A. 2000, A&A, 354, 621

Cushing, M. C., Tokunaga, A. T., & Kobayashi, N. 2000, AJ, 119, 3019

Cutri, R., et al. 2000, http://www.ipac.caltech.edu/2mass/releases/second/doc/

Dame, T. M., et al., 1987, ApJ, 322, 706

Dame, T. M., Hartmann, D., & Thaddeus, P. 2001, ApJ, 547, 792

D'Antona, F. & Mazzitelli, I. 1997, in Mem. Soc. Astron. Italiana, 68, 807

de Zeeuw, P. T., Hoogerwerf, R., de Bruijne, J. H. J., Brown, A. G. A., & Blaauw, A. 1999, AJ, 117, 354

Dolidze, M. V. & Arakelyan, M. A. 1959, Astronomicheskii Zhurnal, 36, 444

Donati, J. F., Semel, M., Rees, D. E., Taylor, K., & Robinson, R. D. 1990, A&A, 232, L1

Durney, B. R., De Young, D. S., & Roxburgh, I. W. 1993, Sol. Phys., 145, 207

Elias, J. H. 1978, ApJ, 224, 453

Favata, F., & Schmitt, J. H. M. M. 1999, A&A, 350, 900

Favata, F., Micela, G., & Reale, F. 2001, A&A, 375, 485

Favata, F., Fridlund, C. V. M., Micela, G., Sciortino, S., & Kaas, A. A. 2002, A&A, 386, 204

Feigelson, E. D., & DeCampli, W. M. 1981, ApJ, 243, L89

Feigelson, E. D., & Kriss, G. A. 1981, ApJ, 248, L35

Feigelson, E. D., Nelson, P. I. 1985, ApJ, 293, 192

Feigelson, E. D., & Montmerle, T. 1999, ARA&A, 37, 363

Feigelson, E. D. et al.2002, ApJ, 574, 258

Feldman, U. 1992, Phys. Scr, 46, 202

Festin, L. 1998, A&A, 336, 883

Fisher, G. H. & Hawley, S. L. 1990, ApJ, 357, 243

Fleming, T. A., Schmitt, J. H. M. M., & Giampapa, M. S. 1995, ApJ, 450, 401

Freeman, P. E., Kashyap, V., Rosner, R., Lamb, D. Q. 2002, ApJS, 138, 185

Gagné, M. 2001, in ASP Conf. Ser., High Energy Universe at Sharp Focus: Chandra Science, ed. E. M. Schlegel & S. Vrtilek, 4

Gehrels, N. 1986, ApJ, 303, 336

Giampapa, M. S., Rosner, R., Kashyap, V., Fleming, T. A., Schmitt, J. H. M. M., & Bookbinder, J. A. 1996, ApJ, 463, 707

Girart, J. M., Rodriguez, L. F., & Curiel, S. 2000, ApJ, 544, L153

Gómez, M., Whitney, B. A., & Wood, K. 1998, AJ, 115, 2018

Grasdalen, G. L., Strom, K. M., & Strom, S. E. 1973, ApJ, 184, L53

Greene, T. P. & Young, E. T. 1992, ApJ, 395, 516

Grosso, N., Montmerle, T., Feigelson, E. D., André, P., Casanova, S., & Gregorio-Hetem, J. 1997, Nature, 387, 56

Grosso, N., Montmerle, T., Bontemps, S., André, P., & Feigelson, E. D. 2000, A&A, 359, 113

Grosso, N. 2001, A&A, 370, L22

Grosso, N., Alves, J., Neuhäuser, R., & Montmerle, T. 2001, A&A, 380, L1

Güdel, M. & Benz, A. O. 1993, ApJ, 405, L63

Güdel, M. et al.2001a, A&A, 365, L336

Güdel, M., Audard, M., Magee, H., Franciosini, E., Grosso, N., Cordova, F. A., Pallavicini, R., & Mewe, R. 2001b, A&A, 365, L344

Güdel, M. et al.2001c, astro-ph/0109267

Haisch, K. E., Jr., Barsony, M., Greene, T. P., & Ressler, M. E. 2002, AJ, 124, 2841

Hamaguchi, L., Terada, H., Bamba, A., & Koyama, K. 2000, ApJ, 532, 1111

Hamaguchi, K., ph.D. thesis, Kyoto University

Hamaguchi, K., Corcoran, M. F., & Imanishi, K. submitted to PASJ

Hartman, R. C. et al.1999, ApJS, 123, 79

Hayashi, C. 1966, ARA&A, 4, 171

Hayashi, M. R., Shibata, K., & Matsumoto, R. 1996, ApJ, 468, L37

Henyey, L. G., Lelevier, R., & Levée, R. D. 1955, PASP, 67, 154

Howard, E. M., Pipher, J. L., & Forrest, W. J. 1994, ApJ, 425, 707

Huenemoerder, D. P., Canizares, C. R., & Schulz, N. S. 2001, ApJ, 559, 1135

Imanishi, K., Koyama, K., & Tsuboi, Y. 2001a, ApJ, 557, 747

Imanishi, K., Tsujimoto, M., & Koyama, K. 2001b, ApJ, 563, 361

Imanishi, K., Tsujimoto, M., & Koyama, K. 2002, ApJ, 572, 300

Imanishi, K., Tsujimoto, M., & Koyama, K. 2002b, Proc. of The IAU 8th Asian-Pacific Regional Meeting, 149.

Imanishi, K., Nakajima, H., Tsujimoto, M., Koyama, K., & Tsuboi, Y. PASJ, accepted

Inoue, H. 1985, Space Sci. Rev., 40, 317

Isobe, T., Feigelson, E. D., & Nelson, P. I. 1986, ApJ, 306, 490

Isobe, H., Yokoyama, T., Shimojo, M., Morimoto, T., Kozu, H., Eto, S., Narukage, N., & Shibata, K., 2002, ApJ, 566, 528

Jerius, D., Freeman, M., Gaetz, T., Hughes, J. P., & Podgorski, W. 1995, ASP Conf. Ser. 77: Astronomical Data Analysis Software and Systems IV, 4, 357

Johnstone, D., Wilson, C. D., Moriarty-Schieven, G., Joncas, G., Smith, G., Gregersen, E., & Fich, M. 2000, ApJ, 545, 327

Kaastra, J.S. 1992, An X-Ray Spectral Code for Optically Thin Plasmas (Internal SRON-Leiden Report, updated version 2.0)

Kamata, Y., Koyama, K., Tsuboi, Y., & Yamauchi, S. 1997, PASJ, 49, 461

Kamazaki, T., Saito, M., Hirano, N., & Kawabe, R. 2001, ApJ, 548, 278

Kastner, J. H., Huenemoerder, D. P., Schultz, N. S., Canizares, C. R., & Weintraub, D. A. 2002, ApJ, 567, 434

Knude, J. & Høg, E. 1998, A&A, 338, 897

Kohno, M., Koyama, K., & Hamaguchi, K. 2002, ApJ, 567, 423

Koyama, K. 1987, PASJ, 39, 245

Koyama, K., Asaoka, I., Kuriyama, T., & Tawara, Y. 1992, PASJ, 44, L255

Koyama, K., Maeda, Y., Ozaki, M., Ueno, S., Kamata, Y., Tawara, Y., Skinner, S., & Yamauchi, S. 1994, PASJ, 46, L125

Koyama, K., Hamaguchi, K., Ueno, S., Kobayashi, N., & Feigelson, E. D. 1996, PASJ, 48, L87

Lada, C. J., 1991, in The Physics of Star Formation and Early Stellar Evolution, NATO ASI, ed. C. J. Lada & N. D. Kylafis, Kluwer, 329

Leous, J. A., Feigelson, E. D., André, P., & Montmerle, T. 1991, ApJ, 379, 683

Liedahl, D.A., Osterheld, A.L., & Goldstein, W.H. 1995, ApJ, 438, 115

Loren, R. B. 1989, ApJ, 338, 902

Loren, R. B., Wootten, A., & Wilking, B. A. 1990, ApJ, 365, 269

Lorenzani, A., & Palla, F. 2001, ASP Conf. Ser. 243, From Darkness to Light, Montmerle, T., & André, P. (San Francisco: ASP), 745

Luhman, K. L. & Rieke, G. H. 1999, ApJ, 525, 440

Mewe, R., Gronenschild, E. H. B. M., & van den Oord, G. H. J. 1985, A&AS, 62, 197

Montmerle, T., Koch-Miramond, L., Falgarone, E., & Grindlay, J. E. 1983, ApJ, 269, 182

Montmerle, T., Grosso, N., Tsuboi, Y., & Koyama, K. 2000, ApJ, 532, 1097

Morrison, R. & McCammon, D. 1983, ApJ, 270, 119

Motte, F., André, P., & Neri, R. 1998, A&A, 336, 150

Mundy, L. G., Wootten, H. A., & Wilking, B. A. 1990, ApJ, 352, 159

Mushotzky, R. F., Cowie, L. L., Barger, A. J., & Arnaud, K. A. 2000, Nature, 404, 459

Nakajima, H., Imanishi, K., Takagi, S., Tsujimoto, M., & Koyama, K. 2003, submitted to PASJ

Neuhäuser, R. & Preibisch, T. 1997, A&A, 322, L37

Neuhäuser, R. & Comerón, F. 1998, Nature, 282, 83

Neuhäuser, R. et al. 1999, A&A, 343, 883

Nürnberger, D., Brandner, W., Yorke, H. W., Zinnecker, H. 1998, A&A, 330, 549

Ohashi, T. et al. 1996, PASJ, 48, 157

Ozawa, H., Nagase, F., Ueda, Y., Dotani, T., & Ishida, M. 1999, ApJ, 523, L81

Ozawa, H. 2000, ph.D. thesis, University of Tokyo

Parker, E. N. 1955, ApJ, 122, 293

Parker, E. N. 1957, J. Geophys. Res., 62, 509

Parker, E. N. 1970, ApJ, 162, 665

Petschek, H. E. 1964, in Proc. of AAS-NASA Symposium on the Physics of Solar Flares, ed. W. N. Ness, NASA, SP-50, 425

Pravdo, S. H., Feigelson, E. D., Garmire, G., Maeda, Y., Tsuboi, Y., & Bally, J. 2001, Nature, 413, 708

Predehl, P., & Schmitt, J. H. M. M. 1995, A&A, 293, 889

Preibisch, T. 1997, A&A, 320, 525

Preibisch, T. & Zinnecker, H. 2002, AJ, 123, 1613

Press, W. H., Teukolsky, S. A.,Vetterling, W. T., & Flannery, B. P. 1992, Numerical Recipes in C (2d ed.; Cambridge: Cambridge Univ. Press)

Reale, F., Betta, R., Peres, G., Serio, S., & McTiernan, J. 1997, A&A, 325, 782

Rodriguez, L. F., Myers, P. C., Cruz-Gonzalez, I., & Terebey, S. 1989, ApJ, 347, 461

Rutledge, R. E., Basri, G., Martin, E. L., & Bildsten, L. 2000, ApJ, 538, L141

Schmelz, J. T. 1993, ApJ, 408, 373

Schmitt, J. H. M. M., & Favata, F. 1999, Nature, 401, 44

Sekimoto, Y., Tatematsu, K., Umemoto, T., Koyama, K., Tsuboi, Y., Hirano, N., & Yamamoto, S. 1997, ApJ, 489, L63

Serlemitsos, P. J. et al. 1995, PASJ, 47, 105

Shemi, A. 1991, MNRAS, 251, 221

Shevchenko, V. S., & Herbst, W. 1998, AJ, 116, 1419

Shibata, K. & Yokoyama, T. 1999, ApJ, 526, L49

Shibata, K. & Yokoyama, T. 2002, ApJ, 577, 742

Silva, A. V. R., White, S. M., Lin, R. P., de Pater, I., Shibasaki, K., Hudson, H. S., & Kundu, M. R. 1996, ApJ, 458, L49

Simon, M. et al.1995, ApJ, 443, 625

Skinner, S. L. 2000, in IAU Symp. No.200, Birth and Evolution of Binary Stars, ed. B. Reipurth & H. Zinnecker (Boston: Kluwer Academic Publishers), 97

Smith, K., Güdel, M., & Benz, A. O. 1999, A&A, 349, 475

Spitzer, L. 1956, Physics of Fully Ionized Gases (New York: Interscience)

Stelzer, B., Neuhäuser, R., & Hambaryan, V. 2000, A&A, 356, 949

Stine, P. C., Feigelson, E. D., André, P., & Montmerle, T. 1988, AJ, 96, 1394

Strom, K. M., Kepner, J., & Strom, S. E. 1995, ApJ, 438, 813

Struve, O. & Rudkjobing, M. 1949, ApJ, 109, 92

Swanenburg, B. N. et al.1981, ApJ, 243, 69

Sweet, P. A. 1958, in IAU Symp. No.6, Electromagnetic Phenomena in Cosmical Physics, ed. B. Lenhnert (Cambridge Univ. Press), 123

Tachihara, K., Mizuno, A., & Fukui, Y. 2000, ApJ, 528, 817

Takagi, S., Murakami, H., & Koyama, K. 2002, ApJ, 573, 275

Tanaka, Y., Inoue, H., & Holt, S. S. 1994, PASJ, 46, L37

Tsuboi, Y., Koyama, K., Murakami, H., Hayashi, M., Skinner, S., and Ueno, S. 1998, ApJ, 503, 894

Tsuboi, Y. 1999, PhD thesis, Kyoto University

Tsuboi, Y., Imanishi, K., Koyama, K., Grosso, N., & Montmerle, T. 2000, ApJ, 532, 1089

Tsuboi, Y., Koyama, K., Hamaguchi, K., Tatematsu, K., Sekimoto, Y., Bally, J., & Reipurth, B. 2001, ApJ, 554, 734

Tsujimoto, M., Koyama, K., Tsuboi, Y., Goto, M., & Kobayashi, N. 2001, ApJ, 566, 974

Tsujimoto, M., Koyama, K., Tsuboi, Y., Chartas, G., Goto, M., Kobayashi, N., Terada, H., & Tokunaga, A. T. 2002, ApJ, 573, 270

Tsujimoto, M. 2003, PhD thesis, Kyoto University

Tsuneta, S., Hara, H., Shimizu, T., Acton, L. W., Strong, K. T., Hudson, H. S., & Ogawaka, Y. 1992, PASJ, 44, L63

Vaiana, G. S. & Rosner, R. 1978, ARA&A, 16, 393

van den Oord, G. H. J., Mewe, R., & Brinkman, A. C. 1988, A&A, 205, 181

Vrba, F. J., Strom, K. M., Strom, S. E., & Grasdalen, G. L.

Waters, L. B. F. M. & Waelkens, C. 1998, ARA&A, 36, 233

Welty, A. D. 1995, AJ, 110, 776

Weisskopf, M. C., Brinkman, B., Canizares, C., Garmire, G., Murray, S., van Speybroeck, L. P. 2002, PASP, 114, 1

Wilking, B. A. & Lada, C. J. 1983, ApJ, 274, 698

Wilking, B. A. Schwartz, R. D., & Blackwell, J. H. 1987, AJ, 94, 106

Wilking, B. A., Lada, C. J., & Young, E. T. 1989, ApJ, 340, 823

Wilking, B. A., Greene, T. P., & Meyer, M. R. 1999, AJ, 117, 469

Xu, J. J., Wang, Z. R., & Qu, Q. Y. 1992, A&A, 256, 483

Yamauchi, S., Koyama, K., Sakano, M., Okada, K. 1996, PASJ, 48, 719

Yokoyama, T. & Shibata, K. 1998, ApJ, 494, L113

Yokoyama, T., Akita, K., Morimoto, T., Inoue, K., & Newmark, J. 2001, ApJ, 546, L72

Yokoyama, T. & Shibata, K. 2001, ApJ, 549, 1160

Young, E. T., Lada, C. J., & Wilking, B. A. 1986, ApJ, 304, L45

Yu, T., & Chernin, L. M. 1997, ApJ, 479, L63

Zhang, Q., Wootten, A., & Ho, P. T. 1997, ApJ, 475, 713

Acknowledgment

I am deeply grateful to Prof. K. Koyama for his continuous guidance and support throughout the five years of my graduate school period. I also thank my collaborators, Dr. Y. Tsuboi, Dr. K. Hamaguchi, Dr. M. Tsujimoto, and Mr. H. Nakajima for their helpful and constructive discussions.

I would like to thank Prof. G. Garmire, Prof. E. D. Feigelson, Dr. L. Townsley, and Dr. Y. Maeda for kind hospitality to the *Chandra* data analysis at the Pennsylvania State University. Many helpful comments and discussions on X-ray observations of YSOs were given by Prof. T. Montmerle, Prof. T. Preibisch, Prof. S. Yamauchi, Dr. N. Grosso, Dr. M. Güdel, and Dr. M. Audard. Results of the solar X-ray observations, numerical simulations, and magnetic reconnection theory were shown by Prof. K. Shibata, Dr. T. Yokoyama, Dr. T. Morimoto, and Mr. H. Isobe. I also thank Dr. F. Motte, Dr. Y. Kamazaki, and Dr. K. Tachihara for their advice about the radio observations on the ρ Ophiuchi cloud. Prof. T. Tanimori, Prof. T. Nakamura, Prof. T. Tanaka, and Dr. H. Matsumoto give me constructive referring and comments on this thesis.

I am grateful to all the members of the Cosmic-ray laboratory in Kyoto University for their continuous discussions, encouragements, and technical advice.

The *Chandra* data were obtained through the Chandra X-ray Observatory Science Center (CXC) operated for NASA by the Smithsonian Astrophysical Observatory. This publication makes use of data products from the Two Micron All Sky Survey, which is a joint project of the University of Massachusetts and the Infrared Processing and Analysis Center/California Institute of Technology. I was financially supported by Japan Society for the Promotion of Science and by the Hayakawa Satio Foundation.

Finally, I would like to thank my family for supporting my graduate school life.